NASA Contractor Report 4238

High-Power Single Spatial Mode AlGaAs Channeled-Substrate-Planar Semiconductor Diode Lasers for Spaceborne Communications

J. C. Connolly, D. B. Carlin,
and M. Ettenberg
David Sarnoff Research Center
Princeton, New Jersey

NASA

National Aeronautics and
Space Administration

Office of Management

Scientific and Technical
Information Division

1989

PREFACE

Table of Contents

APPENDICES

    A. High-Power Edge- and Surface-Emitting AlGaAs
        Semiconductor Lasers
        (Used by permission of the SPIE)

    B. Lateral Optical Confinement of Channeled-Substrate-
        Planar Lasers with GaAs/AlGaAs Substrates
        (Used by permission of the IEEE)

    C. High-Power 0.87-μm Channel Substrate Planar
        Lasers for Spaceborne Communications
        (Used by permission of the SPIE)

    D. Self-Consistent Analysis of Gain Saturation in
        Channeled-Substrate-Planar Double-Heterostructure
        Lasers
        (Used by permission of Appl. Phys. Lett.)

List of Illustrations

List of Illustrations
(cont'd.)

List of Illustrations
(cont'd.)

List of Illustrations
(cont'd.)

SUMMARY

The theoretical understanding of high-power channeled-substrate-planar (CSP) lasers with an emission wavelength between from 860 to 880 nm has been broadened, particularly the effect of optical absorption and gain on the power capability, threshold current, and differential quantum efficiency. The results of this work have been experimentally incorporated into the CSP structure grown by Liquid Phase Epitaxy (LPE) to produce devices displaying record-high output power levels and efficiencies without sacrificing the desirable characteristics of the laser, such as beam quality, non-astigmatic wavefronts, and modulation performance.

The single-spatial-mode output power level for a discrete device (grown by LPE) has been extended to 160-mW cw, more than an 100% improvement over the results reported previously. In addition, the overall power capability for the laser has been increased to 205-mW cw with a corresponding increase in the differential quantum efficiency. A few selected devices displayed stable single-longitudinal-mode behavior under both pulsed and cw operation at power levels up to 100 mW. The typical lateral and perpendicular far-field radiation patterns at the beam full-width half-power (FWHP) point for these devices are 7° and 27°, respectively. As the performance of the CSP laser has improved, the device reliability has also benefited. The results of CSP lasers placed on lifetest at 50 mW (50% duty cycle; 10 MHz) have shown room-temperature lifetimes in excess of 10,000 h, a significant improvement over our previous work.

In our computer modeling studies, we have identified the importance of optical absorption in the winged region of the CSP structure and have been able to correlate the role of this loss mechanism with total power capability. In addition, we have calculated the gain coefficient for the second-order modes in the CSP structure as a function of operating current and have identified the optimum V-channel width for maximum power capability in a single-spatial mode. In other related studies, we have examined the role of the zinc diffusion stripe width on the differential quantum efficiency and threshold current of the CSP laser and expanded our work on the principal guiding mechanisms in the CSP structure.

An improved version of the CSP structure has also been demonstrated, the double current confined-channeled substrate planar (DCC-CSP). This structure contains current blocking layers to more effectively utilize the current in the

laser. These devices have shown 70% differential quantum efficiency (1 W/amp) the highest differential quantum efficiency from any CSP laser we have fabricated without sacrificing the desirable device characteristics necessary for spaceborne communication systems.

HIGHLIGHTS

- 205-mW, cw output power capability
- Single-spatial-mode operation up to 160-mW, cw
- Expanded theoretical modeling capabilities
- Room-temperature LPE-grown CSP lifetimes up to 10,000 h at 50 mW
- Demonstration of DCC-CSP laser structure

Section I

INTRODUCTION

The work described in the previous annual report centered on the continued development of individual high-power, single-mode diode lasers and a new laser structure incorporating a grating to stabilize the longitudinal mode for potential use in areas such as space communications, optical recording and storage, and local-area optical communication networks. In the work on individual laser sources, we reported new record power levels from channeled substrate planar (CSP) lasers grown by LPE with both improved efficiency and reduced threshold current density. These developments were obtained without sacrificing the excellent beam qualities of the device. A new CSP laser structure incorporating a grating to stabilize the longitudinal mode during modulation was also developed. This device not only demonstrated improved longitudinal modal stability, but also exhibited improved temperature-dependance of the threshold current density as compared to conventional CSP lasers.

This annual report describes the research and development work that was conducted to further improve and enhance the CSP laser structure for high output power operation at emission wavelengths between from 860 to 880 nm. A self-consistent method of computer modeling has been developed to identify and improve the ultimate power capability, without sacrificing the desirable operating characteristics and reliability. These studies have lead to the fabrication of CSP diode lasers having the highest single-spatial-mode power ever attained with record-high differential quantum efficiencies.

A modification was also made to the basic CSP laser structure that incorporates current blocking layers to improve the differential quantum efficiency. This has lead to CSP lasers with exceptionally higher differential quantum efficiencies as compared to conventional CSP lasers. In addition, by controlling the material composition of the blocking layer(s), the optical adsorption in the laser structure may be adjusted to optimize the effective lateral index profile. The improvements described above have been shaped by the requirements of the NASA Advanced Communications Technology Satellite (ACTS) Program.

Section II

DIODE LASER PERFORMANCE AT 860 - 880 nm

The goal of this program is the development of AlGaAs diode lasers, with an emission wavelength between 860 and 880 nm, having improved performance and reliability than previously fabricated diode lasers. The eventual use of these diode lasers would be as light sources in intersatellite communications systems and, specifically, the NASA Advanced Communications Technology Satellite (ACTS) System.[1]

In the first three sections, computer modeling studies of optical absorption in the substrate, zinc diffusion stripe width, and guiding mechanisms in the 860 to 880-nm high-power channeled substrate-planar (CSP) diode lasers will be discussed. In later sections, the liquid-phase-epitaxial (LPE) growth, characterization, mounting, and reliability of single-spatial-mode lasers will be discussed.

A. SUBSTRATE ABSORPTION MODELING STUDY

The computer modeling program used at Sarnoff for this work has been developed and refined over the years as our understanding of the operation of the CSP structure has increased. The method of modeling that we use begins with the basic laser structure and then the various components associated with laser operation, such as the current distribution, carrier diffusion gain profile, and heating effects, are sequentially incorporated into our model. As these various components are added, iterations are performed until self-consistency is obtained within the error limits imposed upon the device parameters. The flow chart in Fig. 1 illustrates our self-consistent method of solution. A more completed description of this model can be found in Appendix A. The basic CSP laser structure is shown in Fig. 2, and the parameters we use for our calculations are listed in Table 1.

4
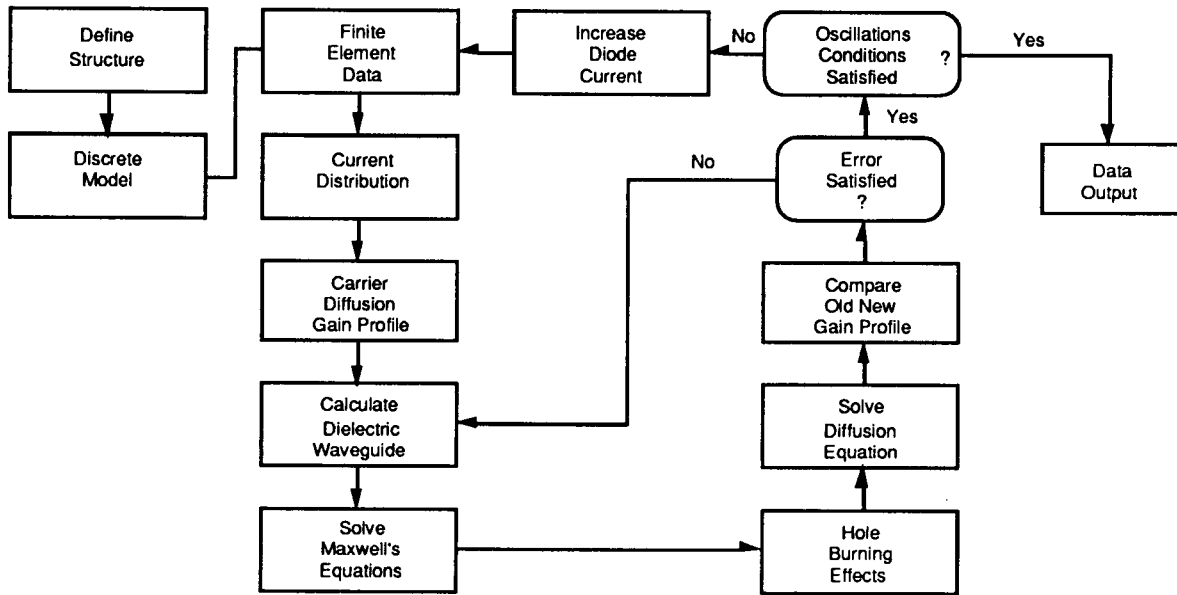
Figure 1. Flow chart summarizing the numerical calculations for laser oscillation above threshold.
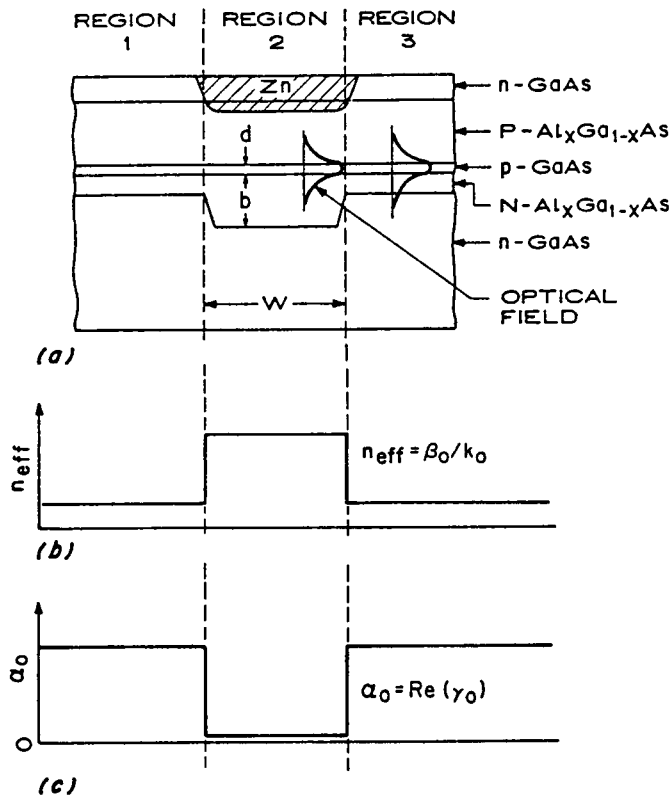
Figure 2. (a) Geometry of a CSP laser, (b) real part of the lateral effective index profile, and (c) imaginary part of the lateral effective index profile.

5

Table 1

CSP MODELING PARAMETERS

	Cladding Layers	Active Region	Substrate
Mole Fraction AlAs	0.30	0.07	0.0
Refractive Index	3.40	3.62	3.64
Absorption Coeffient	10 cm^{-1}	---	5000 cm^{-1}

l = 0.83 μm (lasing wavelength)

d_2 = 0.06 μm (active layer thickness)

B = 10^{12} cm^3/s (bimolecular coefficient)

L_D = 3 μm (carrier diffusion length)

t_s = 3 x 10^{-9}/s (carrier lifetimes)

R_1 = 0.32 (front facet reflectivity)

R_2 = 0.85 (rear facet reflectivity)

d_c = 0.4 μm (n-clad thickness outside channel)

y_0 = 0.5 μm (current decay parameter)

S = 4 μm (stripe width)

L = 250 μm (device length)

The computer modeling results reported in the last annual report identified many key areas responsible for the desirable high-performance characteristics of the CSP diode laser. This work gave a very good understanding of the basic operation of the diode laser and some insight into other areas that required additional analysis. We have identified the loss mechanism that is characterized in the CSP structure by absorption of the optical mode by the highly absorbent GaAs substrate (5,000 cm^{-1}) as one of these areas. This loss or absorption of the optical mode by the GaAs substrate results in excess heat which must be removed from the laser if it is to work well at high power with reliable operating lifetimes. In our normal mounting configuration, the CSP laser is mounted p-side down to the heatsink. Thus, the heat in the substrate must be removed by re-radiation of the absorbed heat across the active region, through the p-cladding and cap layers to the copper heatsink. This absorption cannot be totally eliminated in the CSP laser, however, since absorption of the optical mode by the substrate is crucial to operation in a single-spatial-mode at high output powers.

In last year's study, we found that although the total modal losses in the CSP structure were found to be insensitive to the n-cladding thickness, the normalized loss or the loss parallel to the direction of the active layer varied significantly. We found that the normalized loss increased dramatically as the thickness of the n-cladding layer in the winged region of the structure was reduced from 1.5 μm to 0.2 μm. This loss in the CSP structure is associated with the absorption of the optical mode by the substrate. Thus, as the position of the active layer is adjusted closer to the substrate, greater loss is incurred. This loss in the CSP structure is critical for its operation in a single-spatial-mode at high output powers. The exact role of this loss mechanism in the operation of the CSP laser was not well understood, however. Thus, we chose this particular area as the starting point in our modeling investigations.

In our investigation, we first examined the role of the substrate upon the absorption of the optical mode in the CSP laser. The CSP laser structure we chose to model had the following parameters: (1) n-cladding layer ($Al_{.30}Ga_{.70}As$, 0.40 μm); (2) active layer ($Al_{.07}Ga_{.93}As$, 600 Å); (3) p-cladding layer ($Al_{.30}Ga_{.70}As$, 1.5 μm); (4) p-cap layer (GaAs, 1.0 μm); (5) cavity length - 250 μm; (6) front facet reflectivity - 32%; (7) rear facet reflectivity - 85%. These valves were chosen based upon experimental data from CSP lasers displaying superior high-power single-spatial-mode operation. The channel width, as measured at the substrate surface, was varied from 4 to 10 μm. Figure 3 is a plot of the substrate absorption, at an output power level of 100-mW, as a function of lateral position along the substrate. The zero position is taken to be the center of the V-channel. The four curves represent the substrate absorption for V-channel widths of 4, 6, 8, and 10 μm, respectively. The location of the peaks for each curve corresponds to the shoulders on either side of the etched V-shape channel in the substrate. If we examine the curve for the 4-μm-wide channel, we find at the 100-mW power level, over 50 mW or half of the optical mode is being absorbed by the GaAs substrate. This implies that greater than half of the energy driving the CSP laser is transformed into heat due to the large absorption or loss in the GaAs substrate. This heat is more detrimental than other I^2R effects since it occurs so close to the lasing area. Some estimates, based upon Raman spectroscopy, predict localized temperature increases of greater than 200°C. At this temperature, defects that are present in the crystalline material move extremely rapid. This can lead to the formation of dark line defects (DLDs), the principal cause of degraded or failed semiconductor lasers.[2,3] When the channel width is increased to 6-μm, we find a

7

sudden drop in the amount of optical energy that is absorbed by the substrate. At a 6-µm channel width, only about 10% of the total energy is absorbed, hence the localized heating is greatly reduced. Further reductions can be obtained by increasing the channel width. At a channel width of 10 µm, only about 2% of the optical energy is absorbed. Thus, it would be advantageous to fabricate CSP lasers with the widest possible channel widths.
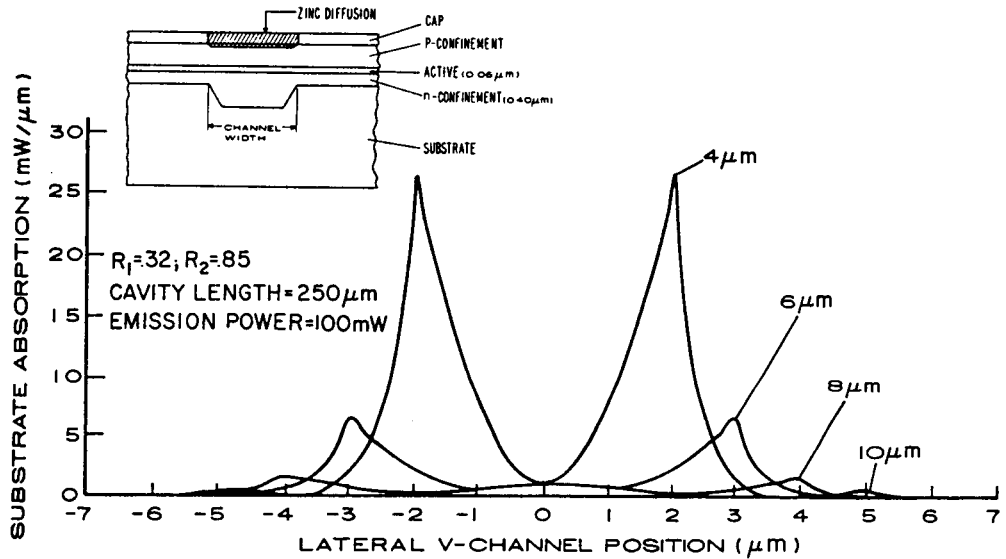
Figure 3.   Substrate absorption of the optical mode as a function of position in the CSP laser. The results for 4-, 6-, 8-, and 10-µm-wide V-channels are displayed. The zero position corresponds to the center of the channel.

The total substrate absorption was also examined as a function of the output power level for 4-, 6-, 8-, and 10-µm-wide channels. This data is shown in Figure 4. A substrate absorption saturation level is reached at low power levels for the 6-, 8-, and 10-µm-wide channels, while the 4-µm-wide channel displays essentially a linear behavior from the low to the high output power levels. Again, this data supports the theory that wide channels are preferred for reduced heating and increased efficiency in the CSP laser.
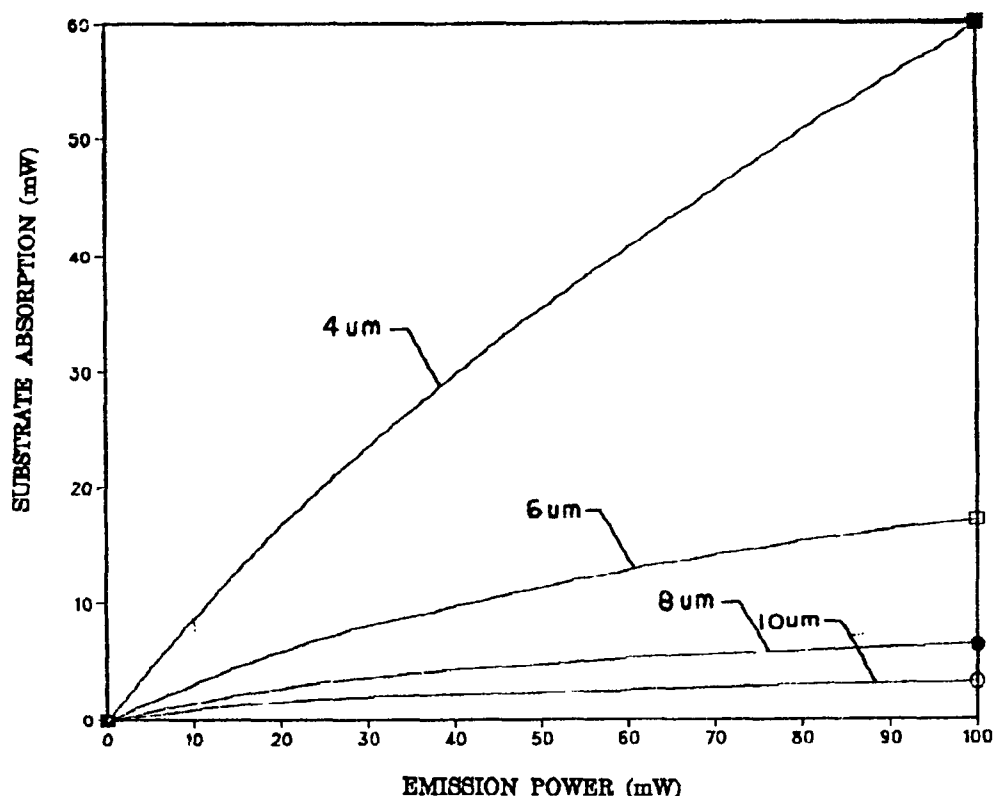
Figure 4.   Total substrate absorption as a function of output power for a CSP laser
with 4-, 6-, 8-, and 10-μm- wide V-channels.

As mentioned previously, the CSP laser requires absorption or loss to
maintain single-spatial-mode operation at high output powers; too little
absorption can lead to beam movement with drive current and higher-order mode
operation. To examine this effect, the gain coefficient for second-order mode was
calculated as a function of driving current. The gain coefficient is defined as

$$g_{th} = G_{th} + \alpha_{fc} + \Gamma^{-1}\alpha_{end}$$

where G_{th} represents the recombination region gain coefficient at threshold, α_{fc} is
the free carrier absorption, Γ is the power confined to the active region, and α_{end}
is the cavity end loss. The gain coefficient was calculated for 4-, 6-, 8-, and 10-μm-
wide V-channels. Figure 5 is a plot showing our results. The dotted line at a gain
value of 25 cm^{-1} represents the amount of gain required for lasing to occur. This
value has been determined from prior modeling studies on both CSP and other
double heterostructure (DH) lasers.[4] The data for the 4-μm-wide channel was not
plotted since the gain coefficient for the second-order mode never attains

9

threshold value even at extremely high driving currents (> 300 mA). The 6-μm-wide channel displays similar behavior in that the second order mode does not attain lasing except at drive current levels far exceeding our expected operating point. Both the curves for the 8- and 10-μm-wide channels cross the threshold value at drive currents of 125 mA and 88 mA, respectively. Thus, higher-order mode behavior is expected for these lasers at these operating currents.

The results from this plot indicate that the smaller channel widths are preferred for high-power operation since no matter how much current is used to operate the device, higher-order mode operation will not be present. Recalling the results from Fig. 3, however, remember that the wider channel widths were preferred since they greatly reduced absorption of the optical mode. Thus, combining the results found from Figs. 3 and 4, the preferred CSP laser structure should contain a V-channel having a width between 6 to 7 μm, in which minimum absorption is present and higher-order single-spatial-mode operation cannot be supported.

The power-vs-current (P-I) curves for the various channel widths were also plotted and are displayed in Fig. 6. The parameters used were the same as described previously. As the channel is increased from 4 μm, a small reduction in the threshold current and a corresponding increase in efficiency is obtained. At the larger channel widths, however, we again see increased threshold currents and reduced device efficiency. If we combine these results with the results from the previous plots, we can deduce the following explanation. The optical field profile for the CSP laser is changing as the width of the channel is increased or decreased. The gain profile in our CSP laser is constant due to the width and depth of the deep zinc diffusion that controls the current injection into the laser. As the profiles for each are overlapped, the performance of the laser will be improved and optimized when the profiles match or overlap one another. At narrow channel widths, the optical field is strongly absorbed in the GaAs substrate, while at larger channel widths, the optical field is weakly confined since the absorption is so weak. The shoulders on either side of the channel are too far from the optical mode, and as a result, carrier leakage is increased (i.e., higher threshold current and lower device efficiency). Once again, we see that this evidence supports a 6 to 8-μm-wide V-channel for lowest threshold current, highest differential quantum efficiency, highest single-spatial-mode power capability, and best reliability from CSP lasers.
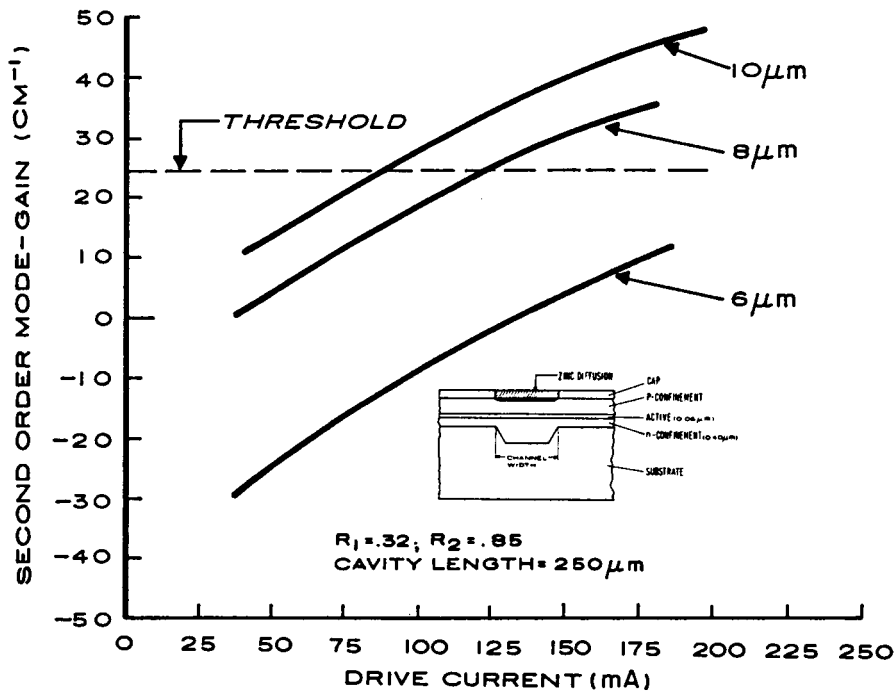
Figure 5. Gain coefficient for the second-order mode of a CSP laser as a function of driving current. Results for 6-, 8-, and 10-μm-wide V-channels are displayed. The dotted line at a gain value of 25 cm^{-1} represents the threshold for the mode.
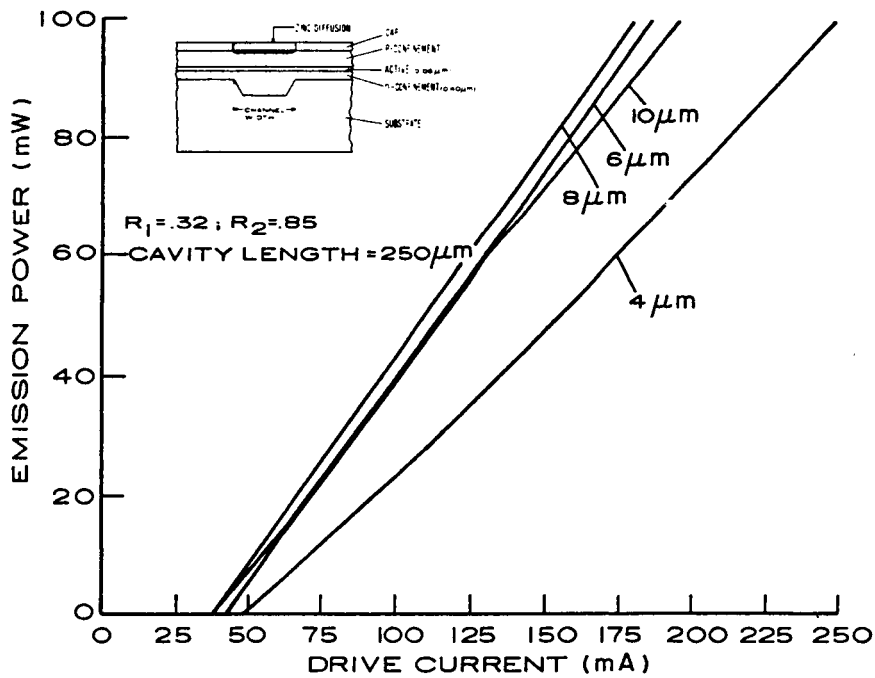
Figure 6. Emission power vs drive current curve for a CSP laser with 4-, 6-, 8-, and 10-μm-wide V-channels.

B. ZINC DIFFUSION MODELING STUDY

In the previous modeling study, the deep zinc diffusion stripe width was held constant at 6-µm. Thus, the gain profile due to the injected current was not varied in this study. Now that we have determined that a 6- to 8-µm channel width is preferred for high performance operation, we examined the effect of varying the width of the zinc diffusion stripe for these optimum channel widths. The parameters that were used were the same as we described previously, except the thickness of the n-cladding layer was reduced from 0.4 to 0.3 µm.

We examined two specific device characteristics, the differential quantum efficiency and the threshold current. These characteristics were chosen since small changes in their magnitude could readily be seen in the performance of the laser. In Fig. 7, the differential quantum efficiency as a function of diffusion stripe width, S, is shown. This plot shows a reduction in efficiency with increasing stripe width and a change in the slope of the curve at about 5 µm. The total change, however, is quite small, only about 10% in efficiency for a 300% change in stripe width. The values reported here may seem low as compared to the devices we have fabricated, but remember these results are for devices having a $\lambda/2$ Al_2O_3 (32% facet reflectivity) dielectric coating on the emitting facet. If the facet reflectivity were lower from 32% to 10%, we would see the corresponding increase in efficiency.
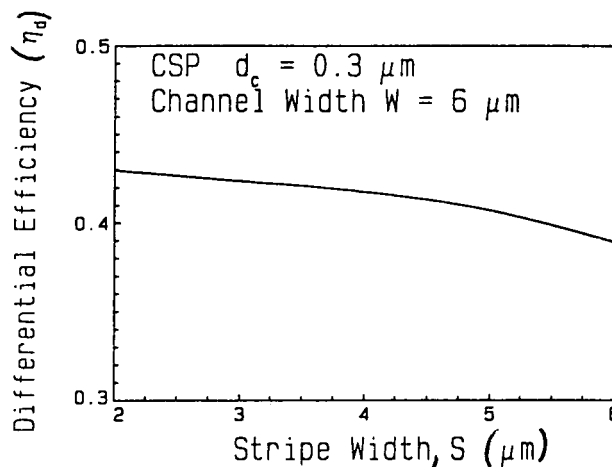
Figure 7.   Differential quantum efficiency as a function of the diffusion stripe width for a CSP laser with a 6-µm channel width.

The 32% value is used in our modeling studies since at this reflectivity value, a uniform gain distribution along the longitudinal direction of the device can be assumed. This greatly simplifies the modeling procedure. In Fig. 8, the change in the threshold current as a function of diffusion stripe width for a 6-μm channel is displayed. There appears to be some discrepancy between the results of the plots. In Fig. 7, the efficiency is increasing as the stripe width is reduced, yet the minimum in the threshold current is found at 3 μm. It would be expected the the maximum efficiency and the lowest threshold current would occur at the same stripe width value. At the present time, we have no explanation why the threshold current curve in Fig. 8 turns back up at a 3-μm stripe width, further study will be necessary to clarify the reason.
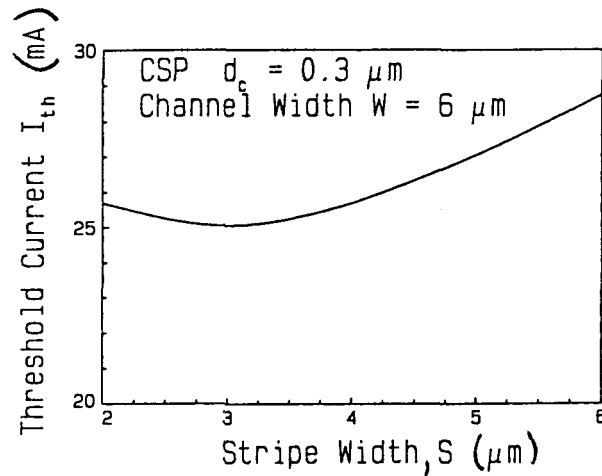
Figure 8.   Threshold current as a function of the diffusion stripe width for a CSP laser with a 6-μm channel width.

This same study was conducted for the 8-μm-wide V-channel, and the plots showing the dependency of the differential quantum efficiency and threshold current as a function of the zinc diffusion stripe width are shown in Figs. 9 and 10, respectively. If we compare these plots, we see good agreement between the two curves. As the stripe width is decreased, we see a corresponding increase in the differential quantum efficiency and a decrease in the threshold current down to 25 mA for a stripe width of 5 μm. The increase in efficiency from about 40% to 50% for a 6-μm-wide channel again is due to improved matching of the optical field and gain profiles.
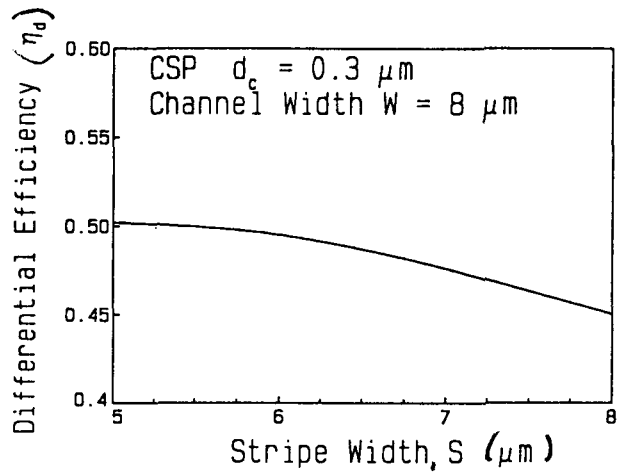
Figure 9.   Differential quantum efficiency as a function of the diffusion stripe width for a CSP laser with an 8-μm channel width.
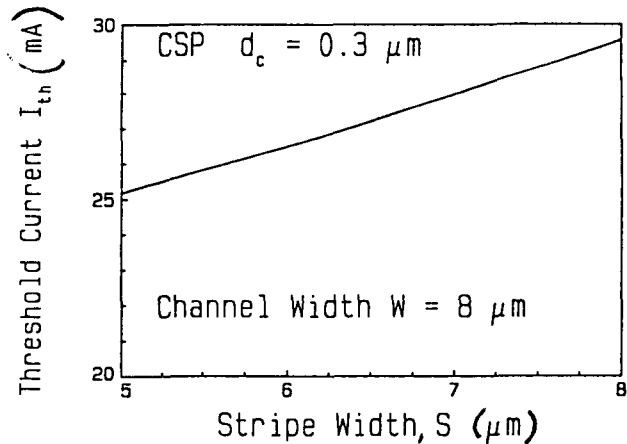
Figure 10.   Threshold current as a function of the diffusion stripe width for a CSP laser with an 8-μm channel width.

The most unexpected result found in this study was that zinc diffusion stripes having a narrower width than the channel are preferred. It has always been assumed that a wider zinc diffusion stripe was desirable, since it would produce an uniform gain profile across the lasing area. Typically, devices containing a non-uniform profile have led to undesirable performance characteristics, such as output beam movement with drive and higher-order mode operation. Thus, previous devices have always been fabricated with diffusion stripe widths greater than the channel width. This indeed produces a uniform gain profile across the lasing area, but also wastes current since the profiles extends far beyond the lasing area. Lasers produced using this method

should display higher threshold currents and lower differential quantum efficiencies. In addition, the current spreading due to the conductivity level found in the p-cladding layer of the laser causes an even wider profile to exist.

Thus, considering these factors, it is understandable that narrow diffusion stripe widths comparable to the width of the lasing spot are the most favorable design. This can be clearly seen in Fig. 9, in which, for an 8-μm-wide V-channel, a 5 to 6-μm wide diffusion stripe is preferred. The width of the lasing spot, as measured from near-field intensity profiles, for a 8-μm-wide V-channel is about 5.7 to 6.0 μm. The change in slope for the curve also occurs at this same value. Further reductions in the stripe width only produces a very small increase in efficiency. This small increase below the 6-μm value is most likely associated with current spreading. We would typically expect current spreading effects to extend approximately 0.75- to 1.0 μm on either side of the stripe area. The actual extent of the spreading is associated with the carrier concentration of the p-cladding layer and the distance from the leading edge of the zinc front to the active layer of the device. At stripe widths below 4 μm, we would expect no further increase in the efficiency. Although all the data supports narrower diffusion stripes, we must remember that too narrow a stripe width can lead to non-uniform gain profiles, a situation we need to stay away from if high-power single-mode behavior is to be expected. Thus, any reductions in stripe width below the width of the lasing spot will be avoided. The small gain in efficiency obtained by further reductions are offset by spatial hole burning effects that will be present at high output power levels.

C.   GUIDING MECHANISM MODELING STUDY

The previous modeling work on the absorption characteristics of the CSP lasers suggested that we should re-examine and expand our work on the principal guiding mechanisms in the structure. The main focus of this work was to (1) analyze the "cold cavity" modal characteristics of conventional CSP lasers that have GaAs and AlGaAs substrates, and (2) present a physical explanation of the CSP guiding mechanism.

The waveguiding mechanisms of the CSP laser have been qualitatively explained in physical terms, and theoretical analyses agree that the lateral mode confinement results from the combination of a positive real index guide parallel to the junction, with high losses (related to a large imaginary component of the

effective index) in the region outside the channel. This resulting complex effective index provides mode confinement parallel to the lasing junction.

The growth of CSP lasers on AlGaAs substrates or AlGaAs buffer layers is of interest to prevent the meltback of the channel profile during the growth. This technique has previously been used to prevent meltback of a grating incorporated in a structure that provides distributed feedback (DFB) operation.[5] In addition, an AlGaAs buffer layer may be a more effective current blocking layer than a conventional GaAs blocking layer. It reduces the localized heating in and around the channel region of the device. In this structure, lateral radiation (because a negative index step lateral waveguide is formed) would be substituted for the transverse substrate radiation of a CSP laser.

We have found that CSP lasers emitting our wavelength of interest have a real positive index step even if the substrate has a mole fraction of AlAs approaching 0.3. Previously, a high absorption loss in the substrate was considered necessary for lateral guiding in CSP structures. A common belief has been that CSP lasers would not be index-guided at long wavelengths (> 860 nm) because of the reduced absorption of the lasing light by the GaAs substrate. (Depending on the dopant concentration of the substrate, the substrate absorption is reduced from about 5000 cm^{-1} at 830 nm to about 500 cm^{-1} or less at 870 nm.)

The analysis of the near- and far-field patterns of the structure can be accomplished using the effective index method. The analysis of the lateral modes (along the y direction) uses the effective index obtained from calculations of the transverse modal field. We assume the fields are written as

$$E_y = E_0 u(x, y)\, u(y)\, \exp(j\omega t - \gamma z)$$

where $\gamma = \alpha + j\beta$ is the complex modal propagation constant. The quantity $u(x, y)$ is the transverse field function and a solution of the wave equation

$$d^2 u/dx^2 + [\gamma_0(y)^2 - k^2_0 \kappa(x, y)]\, u = 0$$

where $\kappa(x, y)$ is the layer-dependent complex relative electric permittivity, $\gamma_0(y) = \alpha_0(y) + j\beta_0(y)$ is the transverse complex propagation constant, and k_0 is the free space wavenumber. Assuming the top p-cladding layer thickness > 1.0 μm , the transverse modes can be determined from a solution of the four-layer waveguide and are shown in Fig. 11.

Figure 11. The (a) and (b) imaginary part of the electric field distribution for the transverse profile shown for a CSP laser structure with an active layer thickness of 60.0 nm, cladding layer of 300.0 nm, and substrate absorption of 5000 cm⁻¹.

The waveguiding in the CSP structure appears paradoxical at first glance. Based upon intuition for bound modes in dielectric waveguides, one expects that the CSP geometry has a larger effective index in the region outside the channel since a significant portion of the perpendicular field distribution there "averages in" the high index of the GaAs substrate. In addition, one expects that the large imaginary component of the effective index outside the channel region is due to high absorption in the GaAs substrate. However, analysis of the CSP structure shows that (1) the effective index is higher in the channel than outside (producing a positive index step and corresponding bound lateral modes), and (2) the mode loss outside the channel region increases as the substrate absorption is decreased.

The reason for these apparent contradictions is that the transverse field in the regions outside the channel is not a conventional bound mode, but a complex field that radiates some power into the substrate. The conventional bound mode of

17

a passive dielectric waveguide has decaying exponential field solutions in the first and last (semi-infinite) layers. A leaky mode has sinusoidal solutions with exponential growth in one or both of the outermost layers. When the outermost layers of an otherwise leaky waveguide have sufficient loss, the field solution is proper (referred to here as a "bound leaky mode") because the fields exponentially decay, although the decay is due to absorption. Conventional bound modes have normalized transverse propagation constants β_0/k_0 that are greater than the refractive indexes of the outermost layers. The complex transverse fields ("bound leaky modes") outside the channel have normalized propagation constants less than the refractive index of one or both outermost layers.

In Fig. 12, we show the near-field intensities (a) and near-field phases (b) for the fields perpendicular to the junction in both the regions inside and outside the channel for a CSP laser with an active layer thickness = 60 nm and substrate absorption, α, = 10,000 cm^{-1}. The wavefront is tilted at 1° for -1.5 < x < 0.0 μm and at about 20.2° for x > 0.3 μm for the mode in the regions outside the channel. Since the direction of wave propagation is perpendicular to the wavefront, the wave outside the channel is therefore tilted away from the z axis of the waveguide and is radiating some energy into the substrate. As the wavefront tilt increases, the guide wavelength λ increases (see Fig. 12). Correspondingly, the propagation constant ($\beta = 2\pi/\lambda_z$) and the effective index ($n_{eff} = \beta/k_0$) decreases.

If we assume that the wavelength in the direction of propagation (λ_p) does not change for the fundamental field distribution perpendicular to the junction, whether it is inside or outside the channel, we can calculate the average tilt angle of the field distribution from (see Fig. 12)

$$\theta = \cos^{-1}[\lambda_p/\lambda_z]$$
$$= \cos^{-1}[\beta_0(y>w/2)/\beta_0(y=0)].$$

For a structure with the active layer = 60.0 nm and the substrate absorption = 10,000 cm^{-1}, β_0/k_0 (at y = 0) = 3.42315 and β_0/k_0 (at y > w/2) = 3.41656, which results in a tilt angle of 3.6°.

From the curves in Fig. 12, a plane-wave equivalent tilt q can be calculated between any two points x_1 and x_2 with corresponding phases (in degrees) $\Phi(x_1)$ and $\Phi(x_2)$ from

$$\theta = \tan^{-1}[\Phi(x_1) - \Phi(x_2)]\lambda_0 / 360 \, n_{eff}[x_1-x_2].$$

18

Indicated in Fig. 12 are plane-wave equivalent tilts between the region of non-zero intensity (-1.0 < x < 1.0) of 8.5° between the $1/e^2$ points in intensity of 2.5° and between the half-power points of 1.6°. Another indication of average tilt of the wavefront can be obtained from the calculated shift of the peak of the far-field intensity pattern (corresponding to the "wing" region, $|y| > w/2$) that is offset from 0° because of radiation into the substrate. The mode perpendicular to the junction, outside the channel region has a calculated shift in the far-field peak of 4° in air [Fig. 12(c)] and, therefore, about 1.2° in the CSP structure.

The use of an AlGaAs substrate or a very thick AlGaAs buffer layer is often desirable, since AlGaAs has less meltback during LPE growth than GaAs. Thus a AlGaAs layer may be preferred for fabricating gratings such as those used in distributed feedback (DFB) CSP lasers. The reduced meltback can also aid in maintaining the dimensions of the channel and the n-cladding layer thickness. An AlGaAs buffer layer can also be a more effective current blocking layer than conventional GaAs layers due to a shorter diffusion length of minority carriers. A more detailed and complete analysis of this work can be found in Appendix B.
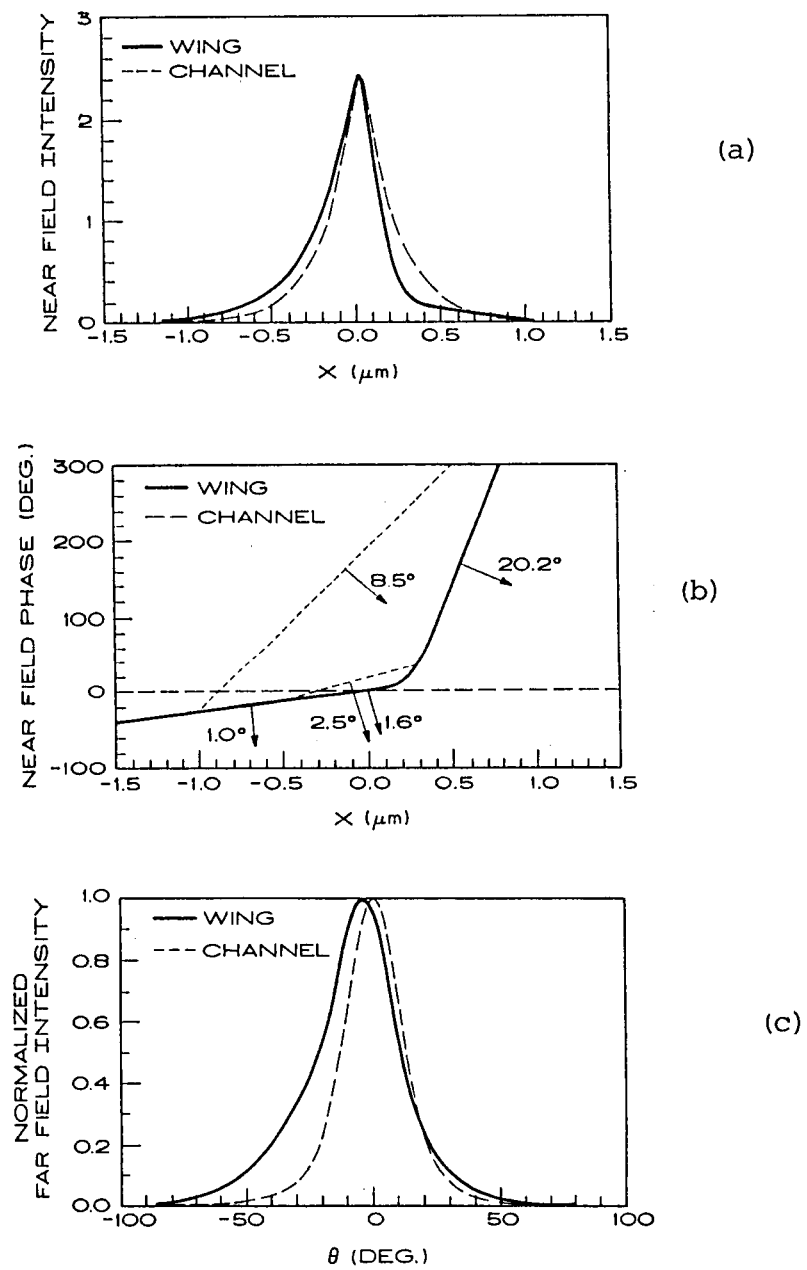
Figure 12.   The transverse (a) near-field intensity, (b) near-field phase, and (c) far-field intensity $I_{ch}(q)$ and $I_w(q)$ for a conventional CSP laser with an active layer thickness of 60.0 nm in the region inside (——) and outside (----) the channel.

D.   MATERIAL GROWTH OF CSP LASERS

In last year's report, we described in great detail the automated liquid phase epitaxial (LPE) growth system used for the fabrication of the CSP lasers. A photograph of this system is shown in Fig. 13. In addition, we reported on a new boat design and discussed growth techniques that provided more uniformly thick layers with greater reproducibility. In this report, we will describe improvements to the LPE process and how we fabricate the high-power CSP lasers.
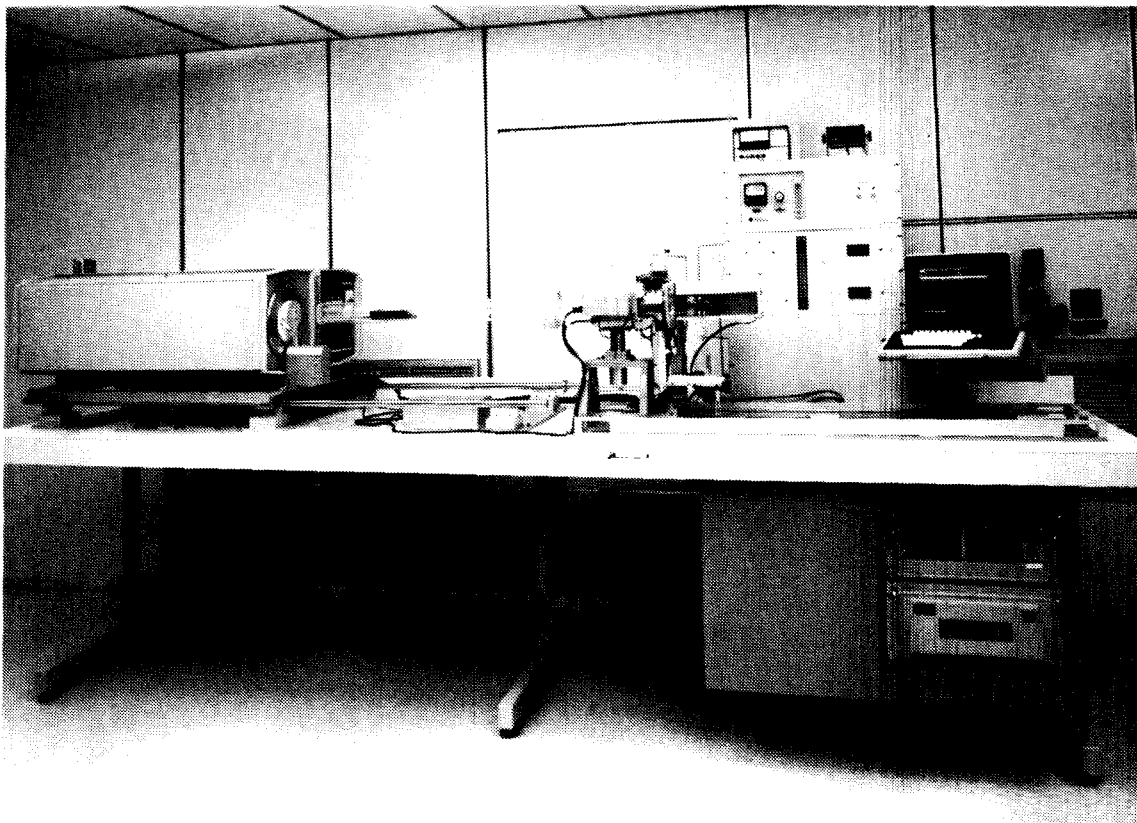
Figure 13.   Photograph of liquid-phase-epitaxial system used for the growth of the CSP laser.

A schematic diagram and cross-sectional micrograph of a CSP structure optimized for an emission wavelength of 870 nm are shown in Fig. 14. The structure is fabricated in a single-growth-step using liquid phase epitaxy (LPE). V-shaped channels are chemically etched in the (100) oriented GaAs substrate along the [011] direction using an oxide-defined contact mask before LPE growth. Prior to placement of the substrate in the horizontal sliding graphite growth boat, the entire surface of the wafer is subject to a light chemical etch. This procedure

21

ensures that both the surfaces in the channel region and on the substrate are chemically prepared in the same manner for LPE growth.
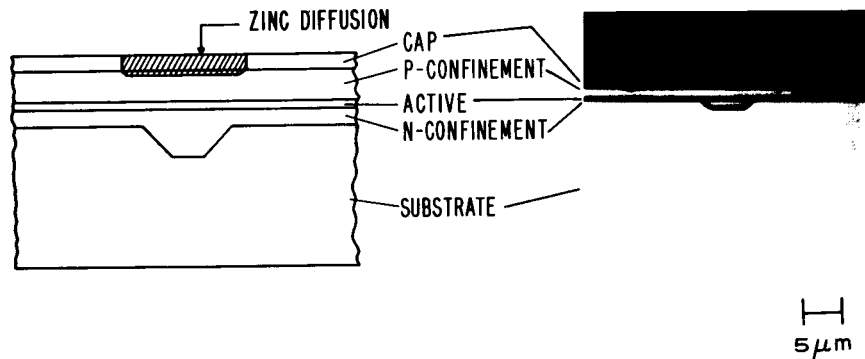
Figure 14.   A schematic diagram and cross-sectional micrograph of the CSP laser structure.

LPE growth is performed over the V-channeled substrate and four layers are grown: (1) $Al_xGa_{1-x}As$ cladding layer (x = 0.27, 0.3 μm, N_d = 1 x 10^{18} cm^{-3}); (2) GaAs active layer (0.07 μm, N_d = 1 x 10^{17} cm^{-3}); (3) $Al_xGa_{1-x}As$ cladding layer (x = 0.27, 1.5 μm, N_a = 5 x 10^{17} cm^{-3}); (4) GaAs capping layer (0.7 μm, N_d = 5 x 10^{17} cm^{-3}). The growth is performed at 800°C using a cooling rate of 1°C/min. The fabrication of high-power CSP lasers having the proper lateral index profile for fundamental mode operation requires the active layer to be planar over the V-channel while the thickness of the n-cladding layer outside the channel region is maintained between 0.2 and 0.5 μm. A non-planar active layer alters the lateral index profile of the CSP structure, which degrades the superior performance characteristics of the laser. To ensure planar active-layer growth over the channel region, it is necessary to maximize the total amount of supercooling associated with the gallium melt used for the growth of the n-cladding layer. This is accomplished in our automated growth system by using the single-phase growth method[6] for the n-cladding layer and the two-phase method[7] for the growth of the other layers in the CSP structure. The single-phase growth method permits us to accurately control the degree of supercooling present in the gallium melt prior to the introduction of the growth wafer. In addition to the quick filling of the V-channel to planarize the layer, careful control of the amount of supercooling also permits a high degree of control on layer thickness not only across the wafer but from one LPE growth run to another. The single-phase growth technique may also be used for the growth of the other layers

in the structure, but is not necessary since the n-cladding layer grown directly on the non-planar substrate planarizes the surface for the subsequent layers. The use of the single-phase growth technique for all the layers in the structure would unnecessarily complicate the growth process.

Another factor effecting the planarity of the active layer in the CSP structure is the crystal orientation of growth substrate. The effects of surface morphology due to large amounts (> 0.5°) of substrate misorientation with respect to the (100) surface has been previously noted in the literature.[8,9,10] We have found that substrate misorientations as small as 0.1° may result in terracing of the n-cladding and active layers in the CSP structure during the LPE growth process. Thus, the shape or planarity of the epitaxial layers are extremely sensitive to such factors as the non-planar growth surface, substrate orientation, and growth conditions. Local arsenic concentration gradients in and around the channels influence the lateral and vertical growth rates that lead to terracing of the epitaxial layers as the channels are filled.[11] Although this effect is not desired in the CSP laser, other high-power lasers, such as the terraced-heterostructure large optical cavity (TH-LOC) laser, have been fabricated exploiting this anomaly.[12] Independent of the growth conditions and/or the geometric channel shape, the terrace or perturbation in the layer would eventually be eliminated as the (100) surface, which possesses the lowest interfacial energy density, is reconstructed. However, in the CSP structure the terrace must be eliminated before the growth of the active layer, otherwise the change in the active layer thickness due to the terrace alters the lateral index profile of CSP structure. By optimizing the LPE growth conditions and minimizing the misorientation of the growth substrate with respect to the (100) plane, planar active layer growth can be obtained on a routine basis.

A terrace formed in the active layer of the CSP structure cannot be observed in standard, high-magnification cross-sectional micrographs. A more effective examination technique is angle lapping of the growth surface. A 1° angle lap polished perpendicular to the active layer can reveal terracing as small as 10.0 nm. Figures 15(a) and 15(b) are 1° angle lap micrographs of two CSP growth runs displaying a terraced and a non-terraced active layer, respectively. The height of the terrace or step in Fig. 15(a) is approximately 60.0 nm, which yields a 20% change in the active layer thickness. Thus, this terrace represents a significant change in the properties of the CSP structure. A CSP laser with a planar active layer is depicted in Fig. 15(b). Laser devices fabricated from this

wafer displayed low threshold operation, kink-free P-I curves to high output powers, fundamental mode operation, and stable far-field radiation patterns, while devices fabricated with the terraced active layers displayed kinks in the P-I curve and far-field radiation patterns that move with changing drive current. Thus, careful control of the V-channel etching, substrate orientation, and LPE growth can lead to the fabrication of CSP lasers having desirable performance properties. The flow of current in the CSP structure is confined to the channel region via a deep zinc diffusion. Zinc is diffused through the n-type cap layer into the p-type cladding layer using an oxide-defined contact mask, thereby forming a reverse bias p-n junction to confine the current flow. The leading edge of the zinc front is positioned approximately 0.5 μm above the active layer.

Figure 15.   Micrographs of two different CSP growths angle-lapped at a 1°-angle showing (a) terraced and (b) non-terraced active layers.

E.   MATERIAL GROWTH OF DCC-CSP LASER

Although significant improvements have been made to the CSP structure that have resulted in devices exhibiting lower threshold currents and record efficiencies, further refinements were still required to reduce the drive level during operation. Our modeling studies indicated that the incorporation of one or more buffer/current blocking layers to effectively focused the current to the lasing area should provide devices with improved differential quantum efficiencies. One very important criteria that we adhere to for any process modifications, was that any change incorporated into the growth process should not reduce the yield

obtained during fabrication or impact the desirable performance qualities of the device.

The incorporation of the buffer/current blocking layers into our CSP structure would require that a second-growth step be added to the fabrication procedure. In addition, a photolithographic process must be performed on top of this layer(s) to facilitate etching of the V-channels. Past experience in other programs in which high-resolution photolithograhy was required, demonstrated that surface morphology was extremely important in terms of contacting the mask used in the photolithographic process. Although the surface morphology obtained in the LPE growth process can be quite good, the edge effects around the perimeter of the wafer due to the growth can result in large hillock formation. In order to facilitate good contacting during the photolitograhic process it is necessary to remove the edges from the grown substrate and only use the central portion for the growth of the CSP structure. This additional LPE process will double the amount of growth time necessary for fabricating the CSP structure and will reduce the throughput from our reactor.

Recently, we have developed a metalorganic chemical vapor deposition (MOCVD) process for the growth of AlGaAs and GaAs films. MOCVD is an open tube vapor-phase epitaxial growth process. This means that the flowing reactant gas stream only contacts the growing surface once. After the stream passes the crystal, the reactants do not participate in the growth process. Efficient deposition of material, thus, requires that a high degree of supersaturation exist over the growing crystal surface. This condition can be established by ensuring that the reactants have high partial pressures in the gas stream. The supersaturation condition is relieved upon contact with the substrate, where the reactants are deposited on the growing crystal and the gas stream leaving the substrate is in equilibrium with the deposited film at the substrate temperature. The partial pressures of the reactants in the gas stream leaving the reactor are reduced by the amount of the reactants deposited on the crystal surface. Since the reactants remaining in the gas stream are now discarded, most efficient deposition occurs when the highest degree of supersaturation is present. A photograph of our MOCVD reactor is shown in Fig. 16.
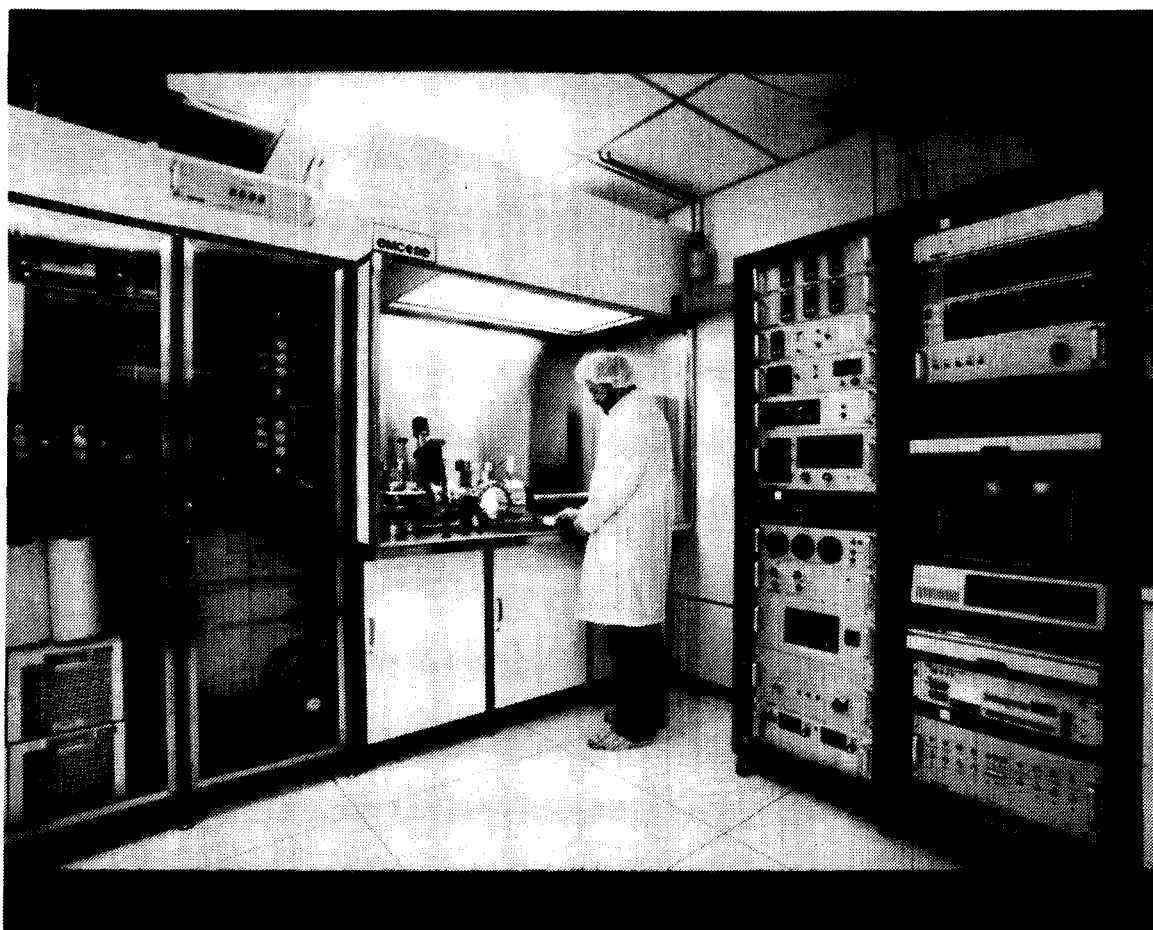
Figure 16.   Photograph of the metalorganic vapor deposition system used to grow current blocking layer/s in the CSP structure.

The growth cell geometry and the manner in which the gas flows through it govern the way the reactants contact the crystal surface. The overall reaction for the growth of GaAs from the trimethylgallium and arsine can be expressed as:

$$(CH_3)_3\ Ga(g)\ +\ AsH_3\ (g)\ =>\ GaAs(s)\ +\ 3CH_4(g)$$
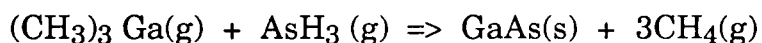
Even at growth temperature the thermodynamic equilibrium for this reaction is far to the right, which implies the reaction will only take place at elevated temperatures or in the presence of a catalyst, the crystalline substrate. The heating in our MOCVD system is controlled by a resistance heated stage that results in only the crystal and gas closest to the crystal surface being heated. The walls in the reactor cell are cool relative to the substrate, thereby minimizing any contamination that may occur and increasing the deposition efficiency.

Although we can thermodynamically predict that the growth reaction will occur, information regarding the rate of reaction cannot be obtained from thermodynamics. The reaction rate is controlled by kinetic effects that are related to the mechanisms of growth and the rate at which the reactant material is delivered to the crystal surface. The reaction rate will therefore be determined by the slowest kinetic effect. These kinetic effects include: 1) transport of reactants to the deposition area; 2) diffusion of reactants through the boundary layer of gas above the crystal surface; 3) diffusion of reaction by-products from the crystal surface through the boundary layer and into the gas stream; 4) transport of by-products away from the deposition area; 5) adsorption of one or more of the reactants or non-reactants (impurities); 6) chemical reactions between adsorbed reactants at the crystal surface or between the adsorbed and the gas-phase reactants; and 7) desorption of reaction products from the growing crystal surface. Processes 1 through 4 involve the transport of material to and from the growing crystal surface. Processes 5 through 7 involve chemical reactions at the growing crystal surface. Since these are kinetic processes, they all exhibit a strong dependence upon the growth temperature.

The temperature range (600°C to 850°C) normally chosen for MOCVD growth allows the reactant input rate and surface processes to be fast relative to the diffusion of material to and from the crystal surface through the boundary layer (processes 2 or 3) formed by the gas stream flowing over the crystal. This is termed mass-transport-controlled or diffusion-limited deposition. In this growth regime, the epitaxial layer growth rate is independent of the wafer orientation due to the fast surface processes. During the growth of GaAs using TMG and AsH_3, the rate limiting step is thus the diffusion of the gallium (Ga) reactants through the stagnant boundary layer above the growing crystal, the concentration on the gas side of the stagnant layer being the same as in the gas stream and complete reaction with As_4 at the crystal surface. The Ga reactants diffusing through the stagnant layer are proportional to the TMG partial pressure in the gas stream and to the square root of the total flow rate since the total flow rate determines the thickness of stagnant boundary layer above the wafer surface.

As just mentioned, if the As reactant (As_4) is in excess (high partial pressure) in the gas stream, then the growth rate is determined by the Ga reactants. This process also holds for III-V ternary alloys such as AlGaAs, since incorporation of the reactants does not depend upon segregation coefficients as in liquid phase epitaxial growth (LPE), but instead relies upon the diffusion of

reactants across the boundary layer. Thus, the Al/Ga ratio in the grown epitaxial layer is usually very close to TMA/TMG ratio in the gas stream. Alloy composition control thus involves the appropriate metering of the gas flows of the constituent reactants. The overall reaction for the growth of AlGaAs from the metalorganics trimethylgallium (TMG) and trimethylaluminum (TMA) and arsine (AsH₃) may be written as:

$$(CH_3)_3 \, Ga(g) + (CH_3)_3 \, Al(g) + AsH_3(g) => AlGaAs(s) + gasses$$
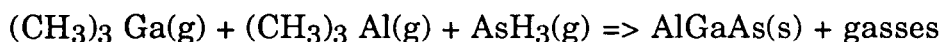
The reactive nature of Al causes problems of incorporation of unwanted impurities, primarily oxygen and carbon. Oxygen is a deep level donor in AlGaAs. In high concentrations, it can form semi-insulating material due to the compensating acceptors. In lower concentrations, it degrades minority carrier lifetimes and the near-band-edge luminescence. For these impurities, particularly oxygen, a molecular sieve trap or liquid metal bubbler (InGaAl) is normally installed in the arsine gas line to remove any trace amounts that may be present.

The doping of GaAs and AlGaAs is carried out by controlling the partial pressure of the dopants in the reactant gas stream. The most commonly used shallow acceptor in the vapor phase growth of III-V compounds is zinc (Zn), derived from dimethylzinc (DMZ). For the n-type dopant or shallow donor we use silicon (Si) derived from silane (SiH₄). The As/Ga or V/III ratios in the reactant gas stream also play a role in determining the incorporation of donors and acceptors in the grown epitaxial film. Higher V/III ratios increase the number of Ga vacancies and decrease the number of As vacancies. Thus, the incorporation of Zn and Si on the V/III ratio, at any fixed V/III ratio both the acceptor and donor density incorporated into the epitaxial film have a linear dependence upon the partial pressure of the dopant in the reactant gas stream.

The method of internally confining the current in the CSP laser utilizes blocking layer(s) of GaAs and/or AlGaAs to channel the flow of current in the device. One approach to incorporating a blocking layer into the CSP structure is growing a layer(s) using MOCVD growth techniques having a polarity opposite to that of the GaAs substrate prior to channel etching and LPE growth. A schematic representation of the CSP laser with an internal current blocking layer, is shown in Fig. 17. We call this structure the double current confined-channel substrate planar laser or DCC-CSP laser. The light generated in the active layer is absorbed in the current blocking layer, which results in the generation of electron-hole

pairs. Thus, when a single layer of GaAs is used then the thickness of the layer must be larger than the minority-carrier diffusion length. If the blocking layer thickness is less than the minority-carrier diffusion length, minority carriers diffuse away from the blocking layer resulting in an accumulation of majority carriers and a reduction in barrier potential. As a result, current is permitted to flow through the layer. If the blocking layer thickness is greater than the minority-carrier diffusion length, electrons and holes recombine in the layer and the barrier to current flow is maintained.
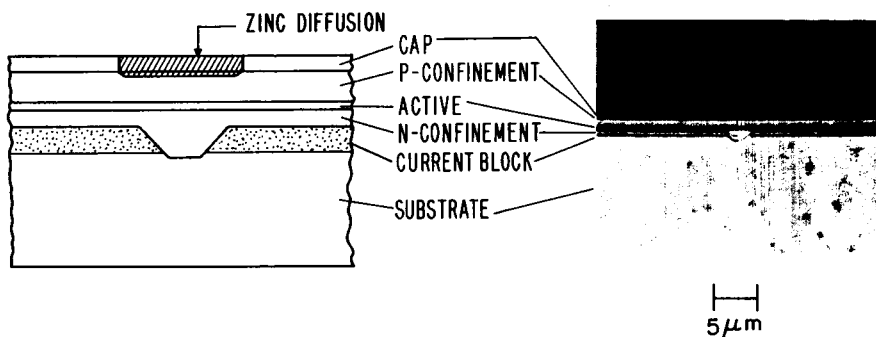
Figure 17.   Schematic diagram and cross-sectional micrograph of the DCC-CSP laser structure.

The fabrication of the CSP structure requires that the thickness of the current blocking layer be thinner than 1.2 μm to maintain the channel width necessary to support fundamental mode operation. The hole diffusion length will always be less than 1.2 μm for carrier concentrations equal or greater than the normal substrate concentration. On the other hand, the electron diffusion length is approximately three times the thickness of the blocking layer. However, there is a very strong dependence of the electron diffusion length upon carrier concentration and composition. At a concentration level an order of magnitude higher than the substrate concentration, the electron diffusion length decreases to below the thickness of the current blocking layer. Although this layer concentration will be greater than what could be obtained using LPE growth techniques, it can be obtained using MOCVD growth techniques. In addition, MOCVD growth technology provides improved surface morphology and layer uniformity. Thus, both p- and n-type current blocking layers may be used in the CSP structure. In addition, a compositional change from GaAs to AlGaAs also results in a reduction of the minority-carrier diffusion lengths. One drawback of using AlGaAs blocking layers is the formation of native oxides on the layer

surface will inhibit nucleation during the LPE growth process. The nucleation problem can be eliminated by only exposing the LPE growth melt to a GaAs surface. Thus we have fabricated a current blocking device consisting of both AlGaAs and GaAs layers. First an $Al_{.10}Ga_{.90}As$ layer is grown to effectively block current flow in the laser structure, except in the channel region, then a thin GaAs layer is subsequently grown on top to eliminate the formation of native oxides that may impede the LPE growth procedure. The small portion of this layer that is exposed in the walls of the V-channel does not disturb the nucleation process in the channel region. A 1° angle lap photograph of a CSP structure with a MOCVD blocking layer is displayed in Fig. 18. These blocking layers are transparent to the the standard LPE growth procedure used to fabricate CSP lasers. Thus, no change to our LPE process was required to implement this new structure. The device results for this new structure (DCC-CSP) are presented in the device characterization section of this report.
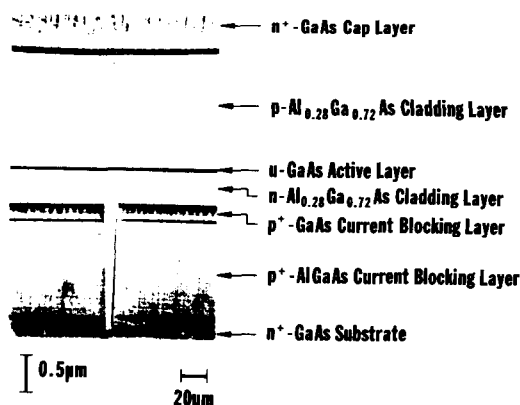
Figure 18. Micrograph of a 1° angle lap of the DCC-CSP structure.

F. LASER DIODE DIE AND WIRE MOUNTING

All the testing and characterization of the CSP lasers are performed on our laboratory mount. This particular mount, which we call the "L-mount," is machined and fabricated in-house. It has been used for many years, not only for the CSP laser program, but almost all other optoelectronic programs. Although it is a convenient mount to use for our work at Sarnoff, it is not the ideal package for a communication system. Its large size and inability to monitor the output power level makes it a poor selection for use in most communication systems. Thus, we looked for an alternate mount that would be commercially available, capable of monitoring the output power level, and can be manufactured to the high tolerance

specification required. The package that meets these criteria is one designed many years ago by Philips Laboratories in Einhoven, Holland. This basic design has been adopted by many manufacturers of both packages and optoelectronic components. A diagram of the package we are using is shown in Fig. 19. It consists of three principal parts, the stem, the mounting ring, and the cap. Fully assembled, it provides a hermetically sealed environment for the laser. In addition, the package when mounted properly to a heatsink permits device operation at high output powers.

At first glance, the conversion from our laboratory mount to a commercially available mount appears to be a simple one. Except when one fully explores what is required to complete the conversion. First the die and wire bonding equipment must be modified to accept the new package. The die bonding equipment not only required re-design of the holder, but also to some of the optics to provide the proper prospective of the laser chip during mounting. In addition, previously the L-mounts were prepared with the solder electroplated on the mount. The new package configuration prevents us from applying this technique. Thus, a Cu sub-mount is used between the laser chip and the mount that has the solder electroplated to it. The fabrication of this submount and the associated plating processes are all performed in-house where they can be carefully monitored to ensure repeatable mounting characteristics. The modification to the wire bonding equipment only required a modification to the mount holder, which posed no major problems.
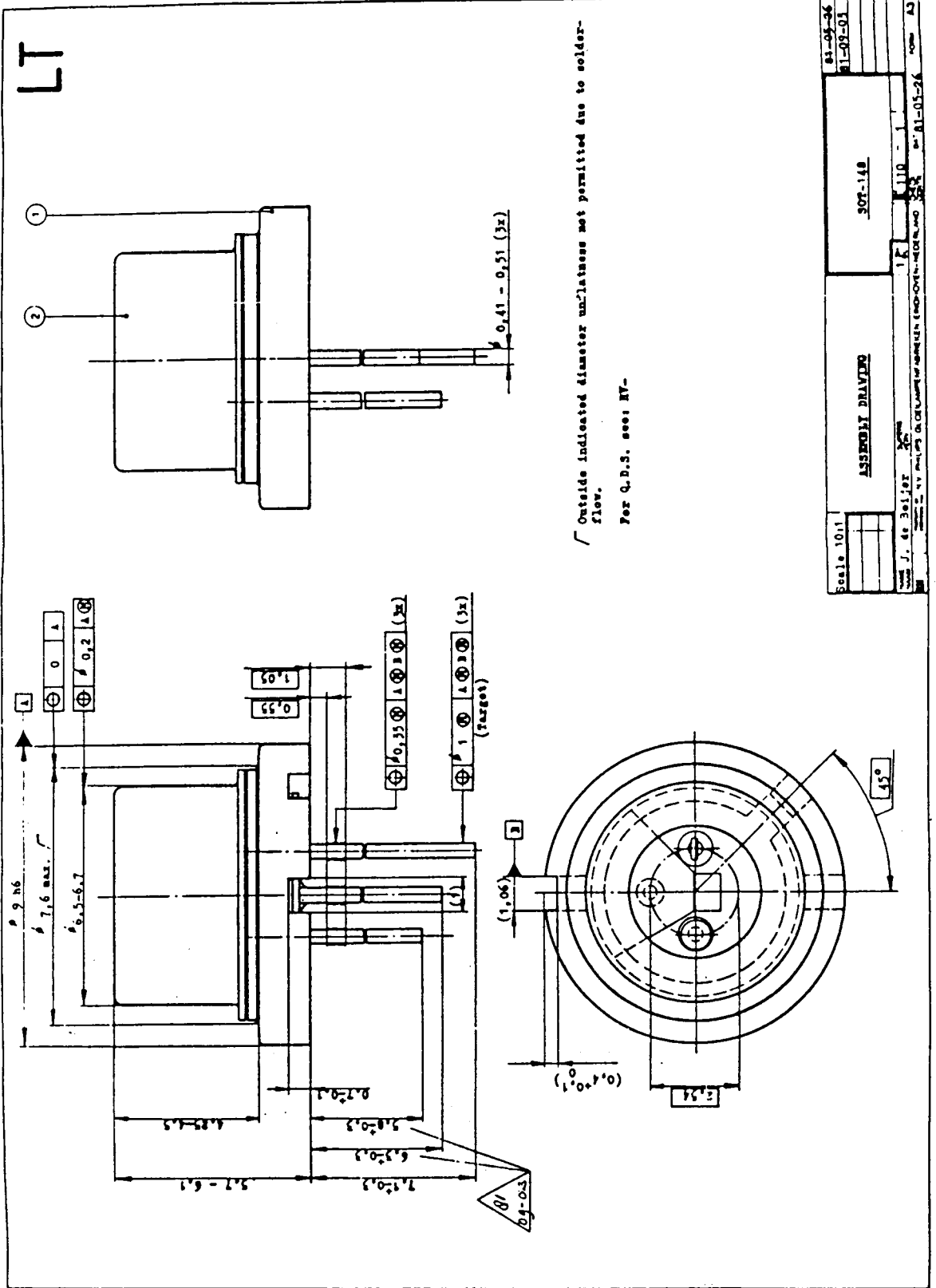
Figure 19. Schematic diagram of package used for mounting the CSP lasers.

Once the laser chips are properly mounted, they need to be characterized to permit evaluation of their performance. This presented the most difficult problem, since the lead configuration for the two mounts are so different, and the new mount contains an additional lead for monitoring the voltage from the detector. The characterization of the high-power CSP lasers are performed both on our fully automated characterization system and our manual system. The automated system can perform all the standard measurements such as: (1) power and voltage vs driving current curves (PIV); (2) far-field radiation patterns; and (3) spectral measurements. This is the system that is used for the majority of our measurements, but the manual system is still required to perform other measurements such as thermal resistance, modulation, and wavelength stability studies. Thus, two different mounts were required. Both these new mounts were designed and fabricated in-house in our mechanical design laboratory and manufacturing facility.

The last systems that needed re-designing due to the new mount were the burn-in and lifetest equipment. They are similar to the characterization system in that the new lead configuration in addition to round package configuration posed difficult re-designing problems, since the lifetest equipment contain monitor detectors that must be aligned with the output beam of the lasers while at the same time be positioned to permit adequate heatsinking during testing. Thus, the conversion to the new laser mount was not as simple as we first thought. Having completed all the necessary system modifications, the high-power CSP lasers are now capable of being delivered in flight ready packages.

G. LASER DIODE OPERATING CHARACTERISTICS OF CSP LASERS

In spaceborne communications systems, the output emission wavelength of lasers are optimized at around 870 nm to avoid absorption of the emitted light by the atmosphere when communicating with ground-based terminals. A CSP laser has been fabricated that has produced lasing operation to 205-mW cw, single-fundamental-spatial and spectral-mode operation up to 100 mW (50% duty-cycle), with single-spatial mode operation continuing up to 160-mW cw; beyond 160 mW there are increasing line broadening effects in the parallel far-field pattern due to gain saturation effects and higher order mode operation as described in the modeling section of this report.

In Fig. 20, the power output vs drive current (P-I) curves for two devices are displayed. The devices are 200-µm long, with a (λ/4) Al_2O_3 passivation coating on the (front) emitting facet and a six-layer dielectric-stack reflector on the rear facet.[13] In Fig. 20(a), we show the performance of the CSP laser as the heat sink temperature is varied from 0°C to 80°C. Note that 80-mW-cw output power was obtained at a heatsink temperature of 80°C. The device operated in a stable single-spatial mode over the entire temperature range. The differential quantum efficiency of the device decreased from 62% to 45% as the heatsink temperature was raised from 0°C to 80°C. The T_0 value for this device in cw operation over this temperature range is approximately 100°K. At 62% differential quantum efficiency, the slope efficiency of the device is 0.89 mW/mA.

Figure 20(b) shows the results of operating a device to its catastrophic optical damage (COD) level. Damage occurred at 205 mW cw at a drive current of 335 mA. The applied voltage at 205 mW is 1.76V. The emitting facet of the device displayed melting of the crystalline material, normally associated with facet damage. This exceptionally high COD level was attained without the use of a window type structure.[14] The differential quantum efficiency for this device was 55% at the COD level. Also displayed in this figure is the total power conversion efficiency from the emitting facet of the device from the lasing threshold value to the maximum cw output power level. A peak power conversion efficiency of >35% was measured for this device. The high power conversion efficiency of this device, which permits single-mode operation at high output powers and temperatures is associated with the optimization of the current flow and mode control in the CSP structure. Attention to the control of these parameters using improved growth and processing procedures will ultimately lead to high reliability at high power.
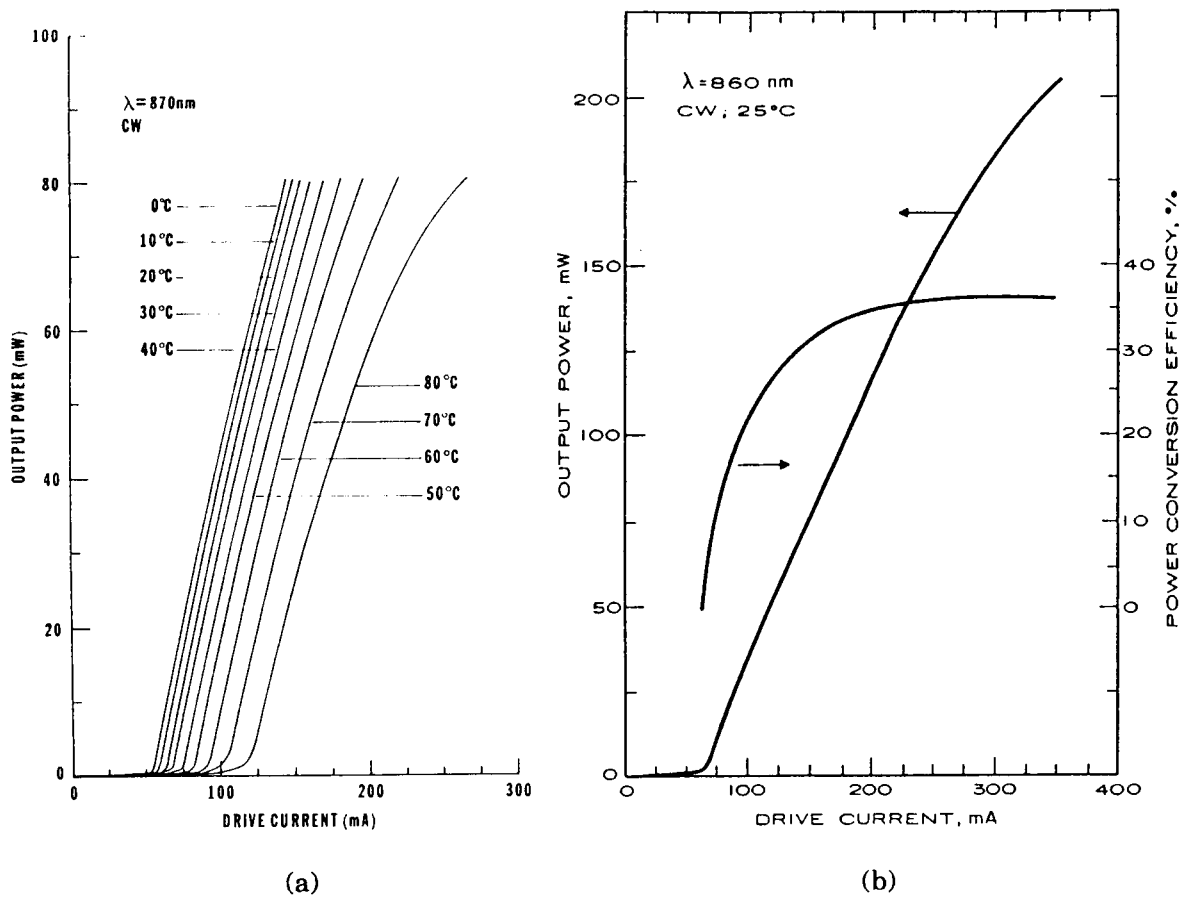
Figure 20. Power output vs operating current (P-I) curve for a CSP laser at (a) various heatsink temperatures and (b) when operated to its catastrophic optical damage (COD) level.

The spectral behavior of the optimized CSP structure at an elevated power level is shown in Fig. 21. Predominantly single-longitudinal-mode operation was achieved to (a) 100 mW cw and (b) 100 mW 50% duty-cycle of output power. At higher output powers, the intensity ratio of main mode to the satellite modes decreases with increasing drive, thereby degrading the single-longitudinal-mode qualities of the device. Spectral changes with increasing output levels reflects increases in junction temperature due to joule heating effects. At 100 mW, the CSP laser operates at approximately three times the threshold current. The spectral behavior the devices was also examined while the operating temperature was varied. The wavelength shift of the longitudinal mode was measured as the heatsink temperature was modulated. As the operating temperature of the device is increased, the laser emission shifts towards higher wavelengths. Large

changes in temperature cause all the power in the dominant longitudinal mode to shift to the next higher longitudinal mode. This behavior is usually referred to as a mode hop. When a mode hop or shift occurs, the power in the longitudinal mode is shared between modes. Mode hop normally occurs over a 2°C to 3°C temperature range and that the longitudinal mode is stable both above and below this transition region. These shifts are normally seen approximately every 6°C to 7°C over the temperatures we investigated. One of the best CSP devices (see Fig. 22) exhibited stable longitudinal- mode operation over a 15°C temperature range at a cw output power of 41mW (H. Hendricks and T. Mack, *private communications*). The wavelength shifted from 868.8 nm to 870.0 nm as the temperature was varied from 15°C to 36°C. This corresponds to a wavelength dependence of 0.08 nm/°C over this temperature range. Over a much larger temperature range (~50°C) this device displayed the characteristic 0.3 nm/°C wavelength dependence normally associated with CSP-type lasers.
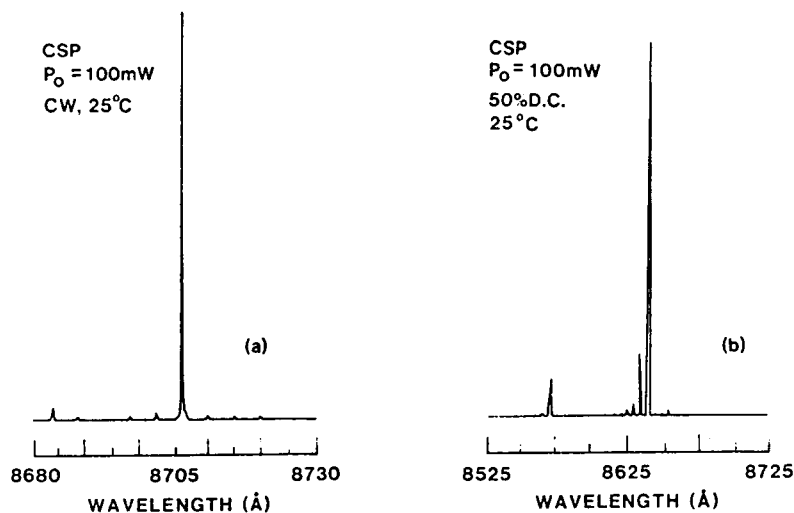
Figure 21.   Longitudinal-mode spectrum for a CSP laser operating at 100 mW in the (a) cw and (b) 50% duty-cycle modes.

The lateral and perpendicular far-field patterns of an optimized CSP laser from 100 mW to 190 mW of cw output power are shown in Fig. 23. Below 100 mW, the beam full width at half-power (FWHP) of the lateral far-field patterns remained unchanged with drive current. At output powers of 100 mW and above the beam FWHP broadens from 11° to 15° with increasing drive current due to heating and gain saturation in the CSP structure. The perpendicular far-field

pattern did not change with increasing drive current, the beam FWHP remains unchanged at 25°. At output powers exceeding 190 mW, higher order mode operation begins to dominant until the COD level is reached. While the heatsink temperature was varied, we monitored the far-field pattern of several optimized CSP devices. At powers below 100 mW, the lateral far-field pattern remains unchanged in both the cw and pulsed conditions. This is expected, since the lateral-mode confinement is provided by a real index dielectric waveguide. This also confirms that the superior device performance is not related to changes in the lateral-mode guiding. Typical beam dimensions at FWHP levels in the planes parallel and perpendicular to the junction for the optimized CSP structure are 8° to 12° and 22° to 26°, respectively. The exceptional single-mode performance of this device at high output powers is related to the very high power conversion efficiency it displays. This high efficiency significantly reduces thermal effects at high output powers that can modify the index profile. Small changes in the complex lateral index profile due to joule heating can dramatically degrade the single-mode properties of the device. Minimizing the joule heating in this structure by reducing optical absorption losses has permitted operation in a single spatial mode at output powers previously unattainable before in conventional CSP structures.
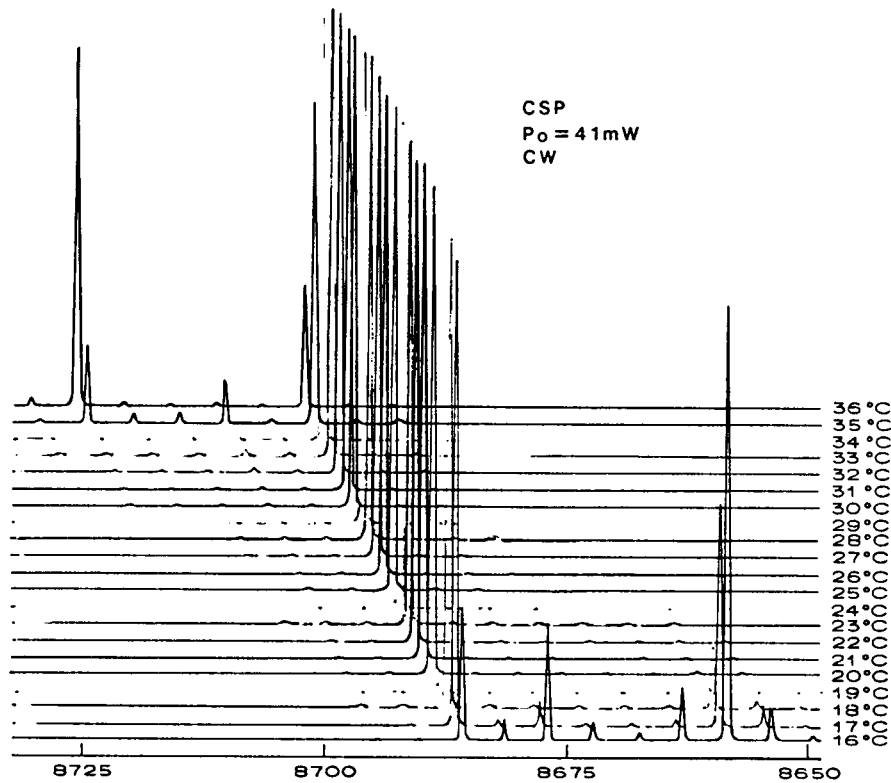
Figure 22.   Longitudinal mode spectrum for a CSP laser operating at 41-mW cw
as the heatsink temperature is varied from 15°C to 36°C.

In free-space communications, large signal losses may occur due to aberrations in the collimated output beam of the diode laser. The source of these aberrations may be associated with the diode laser, the optical system forming the beam, or variations in the atmosphere if the system is used for communication between space and ground terminals. In conventional oxide-defined or gain-guided lasers, sizable aberrations are present in the output beam. In particular, they exhibit large amounts of astigmatism, which change as power is varied and during modulation. By using index-guided laser sources, such as a CSP-type device, to achieve diffraction, limited performance aberrations are minimized. The phase fronts of collimated 870-nm CSP diode lasers have been experimentally measured using a LADITE computer-controlled Mach-Zehnder interferometer. The total rms phase aberrations measured ~λ/50 under all operating conditions up to 100 mW of cw output power, well below the level at which aberrations significantly decrease beam quality. A more detailed description of these results can be found in Appendix C.
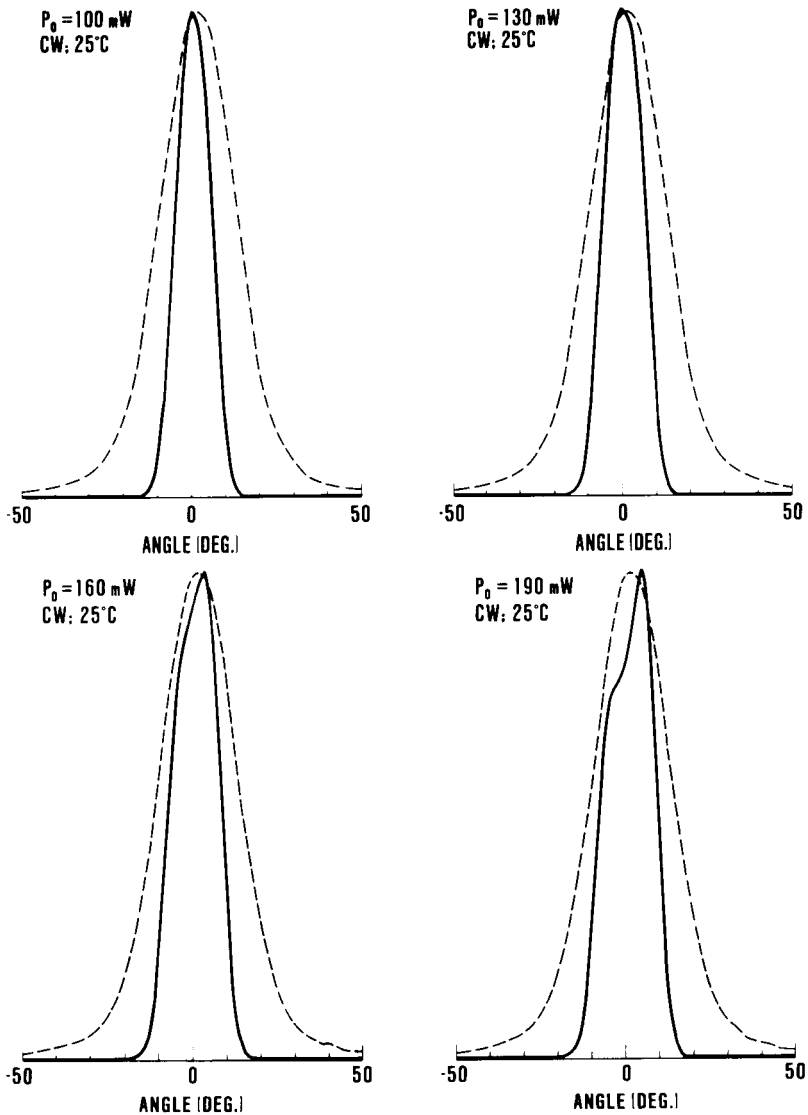
Figure 23. Lateral and perpendicular far-field radiation patterns for a CSP laser operating from 100- to 190-mW cw.

H. LASER DIODE OPERATING CHARACTERISTICS OF THE DCC-CSP LASER

Several LPE growth runs incorporating the new current blocking layer have been characterized. In Fig. 24 (a) and (b), the output power vs drive current and corresponding far-field radiation patterns are displayed. The output power was measured both in the cw and 50% duty-cycle mode at a heatsink temperature

of 25°C. The laser was operated up to 35 mW and 70 mW, respectively. The differential quantum efficiency remained unchanged at 70% for both modes of operation.
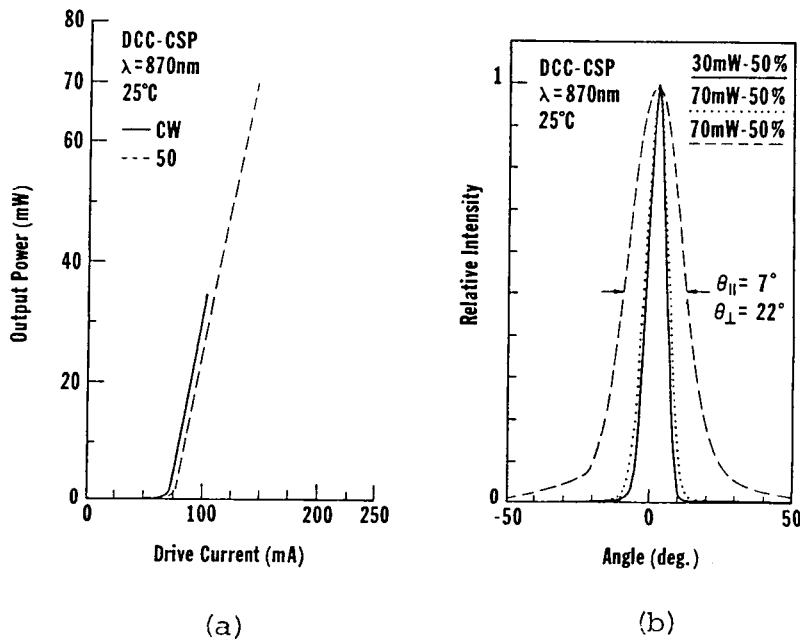
Figure 24.   (a) Power output vs operating current (P-I) curve and (b) lateral and perpendicular far-field radiation patterns for a DCC-CSP laser.

The perpendicular and lateral far-field radiation patterns for the DCC-CSP laser are displayed in Fig. 24(b). They were measured in both the cw and 50% duty-cycle mode of operation. The lateral far-field pattern was measured at 30 mW cw and 70 mW 50% duty-cycle. The beamfull width at half power (FWHP) remained unchanged at 7°, indicating that no movement of the lasing spot occurred with output power or operating conditions. The perpendicular far-field radiation pattern was measured at 70 mW 50% duty-cycle and the FWHP was 22°. These measurements were conducted at a heatsink temperature of 25°C.

The spectral characteristics of the DCC-CSP laser are shown in Fig. 25. The spectrum was measured at a heatsink temperature of 25°C and under both cw and 50% duty-cycle operation. Single-longitudinal-mode operation was displayed under both operating conditions at the same peak emission wavelength of 866.2 nm. The extremely high efficiency of the device significantly reduces the heating effects in the laser, thus, permitting operation at the same peak

wavelength at different power and operating conditions. The small amount of spectral broadening observed in the 50% duty-cycle mode is associated with chirping of the longitudinal mode during the pulse. This particular CSP device has no means of fixing the lasing wavelength during modulation.

DCC-CSP
30mW-CW
25°C

8635   8660   8685
Wavelength (Å)

(a)

DCC-CSP
70mW-50%
25°C

8635   8660   8685
Wavelength (Å)

(b)
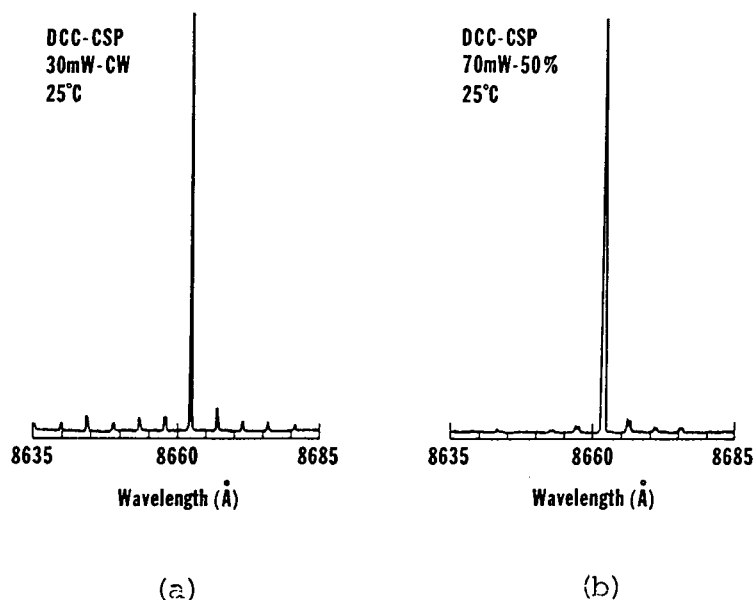
Figure 25.   Longitudinal mode spectrum for a DCC-CSP laser operating (a) cw and (b) 50% duty-cycle at an output power level of 35 mW and 70 mW, respectively.

I.   RELIABILITY ASSURANCE

The devices used in our lifetest studies were mounted p-side down to the L-mount copper heatsink using both hard and soft solders. The n-side contact was made using a wire lead. The devices were tested using a constant power technique in which the drive current used to power the device was continually adjusted to maintain rated output power. This technique subjects the devices to a greater operational stress than the constant current technique in which the laser device is placed on lifetest at rated power and the change in output power is monitored. The threshold currents for all the devices were below 80 mA and the initial thermal resistances were between 20° c/w and 40° c/w. The lasers had (λ/4) Al_2O_3 coating with a reflectance of 10% on the emitting facet and a (λ/4) Al_2O_3/Si stack coating having a reflectance of 90% on the rear facet. The devices were not

subject to a preselection burn-in process prior to placement on lifetest. The devices placed on lifetest were taken from three different LPE growth runs that displayed operational characteristics of suitable for use in the ACTS program.

The devices chosen for our lifetest study all operated in the fundamental mode and had emission wavelengths between 860 nm and 880 nm. The lifetime criteria used for this study is device operation in a fundamental mode at an output power level of 50 mW, not just the ability to lase. Once a device is no longer able to maintain this power level, it is removed from the test. In almost all cases devices removed from the lifetest system still exhibited lasing, but displayed an increase in threshold current. At specific intervals some of the devices were removed from the lifetest system and their operational characteristics (i.e. threshold current, far-field radiation patterns, spectrum, etc.) were re-examined. The pulsed threshold typically showed no change for devices requiring little or no change in drive current while devices with larger drive current changes showed moderate increases. The cw threshold increased slightly on most devices. We attribute this change to an increase in the thermal resistance of the devices. The far-field radiation patterns were found to be remain unchanged, as expected, for index-guided type devices. The peak emission wavelength for these types of devices showed only moderate changes in wavelength with operational time. The wavelength shift with operating time is an important parameter in a laser communication system incorporating dichroic filters to combine the output from multiple sources. A change in the emission peak outside the bandpass tolerance of the dichroic filter (~20 nm) will lead to a severe reduction in total optical power of the communication system.

In Fig. 26, we show lifetest test data for another group of seven CSP lasers operating at 50 mW (50% duty cycle, 10 MHz). Four devices have failed to maintain the 50-mW power level and three are still operating with operational times exceeding 10,000 h. The four failed devices ceased to maintain rated power between a operating time of ~ 3,000 h and 8,000 h. A visual examination of the failed devices revealed no information as to the exact cause of the failures. In addition, no evidence of catastrophic optical damage (COD) was observed on either the emitting or reflective facet. Although these particular devices had not been examined using TEM analysis, other devices displaying similar degradation characteristics have shown DLDs as the cause of their failure. Two of the three diodes still remaining on lifetest required no adjustment in drive current

throughout the entire lifetime. This is a good indication that little or no change in the bulk material properties or thermal resistance has occurred.
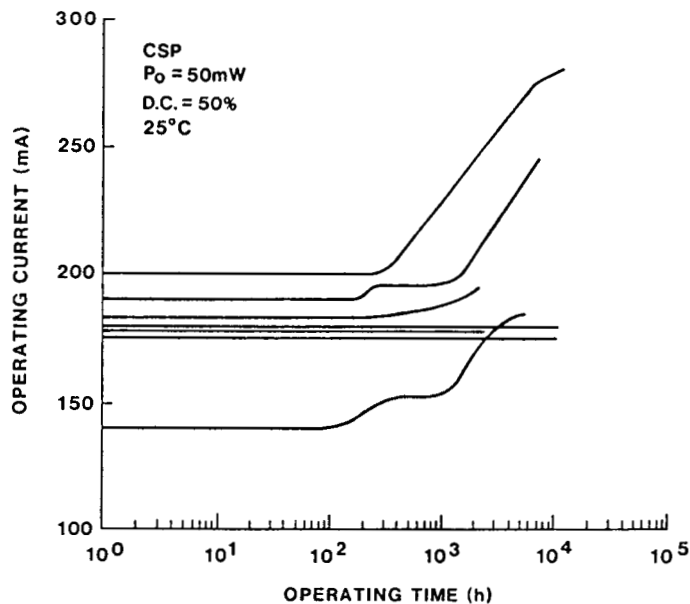
Figure 26. Aging behavior of high-power, 860- to 880-nm CSP lasers as a function of operating time. The lasers were maintained at a constant output power level of 50 mW (50% duty-cycle;10 MHz).

The small population size of this lifetest study precludes the determination of accurate device lifetimes based upon this study. There is one conclusion that can be drawn, however. The lasers in this study were not subject to any type of burn-in procedure prior to being placed on test. It is evident that some type of pre-selection process would have been beneficial in eliminating some of the lasers that failed early in our study. A good starting point for this selection process would be a burn-in procedure using the operating conditions the same as in our study for a set period of time and eliminating any devices displaying change in their operating characteristics during that time. If this procedure was performed, on the lasers in our study, for a time period of 500 h, four of the failed devices would have been eliminated from the study (see Fig. 26). This certainly would change the way the results of this study would be interpreted. Thus, future lifetest studies should include some type of pre-selection procedure prior to placement of devices on the lifetesting equipment.

Section III
CONCLUSIONS

The continued development of the high-power CSP laser by NASA has led to substantial developments in computer modeling and fabrication techniques. These developments have resulted in the fabrication of lasers operating at wavelengths (860 nm - 880 nm) previously thought unattainable with record high-power capability and total power conversion efficiency of 205 mW cw and > 35%, respectively. The transparency of the atmosphere in this wavelength regime makes these results significant for optical communication links between space and ground-based systems. Further work is still necessary, however, to develop sources to meet the critical requirements for space applications. Although preliminary reliability evaluations of the devices at room temperature look quite good (> 10,000 h at 50 mW, 50% duty cycle, and 10 MHz), improved reliability at this wavelength range is still currently a major concern. In addition, to ensure only long-lived devices are used in reliability assessment studies and operational systems, a suitable burn-in procedure must be developed. Reliability assessment studies are currently underway for the realization of a spaceborne communication system.

Section IV

REFERENCES

1. D. B. Carlin, M. Ettenberg, N. A. Dinkel, and J. K. Butler, "A high-power channeled-substrate-planar AlGaAs laser,"J. Appl. Phys. 47, 655-667, Oct. 1985.

2. P. Petroff and R. L. Hartman, "Defect structure introduced during operation of heterojunction GaAs lasers," Appl. Phys. Lett. 23, 469-471, Oct. 1973.

3. H. Kressel and I. Ladany, "Reliability aspects and facet damage in high-power emission from (AlGa)As cw laser diodes at room temperature," RCA Rev. 36, 230-239, June 1975.

4. H. Kressel and J. K. Butler, Semiconductors Lasers and Heterojunction LEDs, Chapter 7, Section 5, Academic Press, New York, pp. 269, 1977.

5. B. Goldstein, G. Evans, J. Connolly, N. Dinkel, and J. Kirk, "Efficient AlGaAs channeled-substrate-planar distributed feedback laser," Appl. Phys. Lett. 53 (7), 550-552, Aug. 1988.

6. J.J. Hsieh, "Thickness and surface morphology of GaAs LPE layers grown by supercooling, step-cooling, equilibrium-cooling,and two-phase solution techniques," J. Crystal Growth 27, 49 (1974).

7. J.J. Hsieh, "Thickness and surface morphology of GaAs LPE layers grown by supercooling, step-cooling, equilibrium-cooling,and two-phase solution techniques," J. Crystal Growth 27, 49 (1974).

8. T. Nishinaga, K. Pak, and S. Uchiyama, "Studies of LPE ripple on morphological stability theory," J. Crystal Growth 43 (1978) 85.

9. B. L. Mattes and R.K. Route, "LPE growth of GaAs: formation of nuclei and surface terraces," J. Crystal Growth 27 (1974) 133.

10. D. L. Rode, "Crystal growth terraces and surface reconstruction," J. Crystal Growth 27 (1974) 313.

11. D. Botez, W. Tsang, and S. Wang, "Growth characteristics of GaAs-Ga$_{1-x}$Al$_x$As structures fabricated by liquid-phase epitaxy over preferentially etched channels," Appl. Phys. Letters 28 (1976) 234.

12. D. Botez and J. C. Connolly, "Terraced-heterostructure large optical cavity AlGaAs diode laser: A new type of high-power cw single-mode device," Appl. Phys. Letters 41 (1982) 310.

13. M. Ettenberg, "A new dielectric facet reflector for semiconductor lasers," Appl. Phys. Lett. 32 (1978) 724.

14. T. Murakami, K. Ohtaki, H. Matsubara, T. Yamawaki, H. Saito, K. Isshiki, Y. Kokubo, A. Shima, H. Kumabe, and W. Susaki, "A very narrow-beam AlGaAs laser with a thin tapered-thickness active layer (T^3 laser)," IEEE J. Quantum Electron., QE-23 (1987) 712.

Appendix

High-power edge- and surface-emitting AlGaAs semiconductor lasers

G. A. Evans, J. K. Butler, D. B. Carlin, N. W. Carlson, J. C. Connolly, and J. M. Hammer

David Sarnoff Research Center, Inc.
CN 5300, Princeton, NJ 08543-5300

1. INTRODUCTION

Channeled-Substrate-Planar (CSP) AlGaAs/GaAs semiconductor lasers are important, established, commercial products and have been extensively studied both experimentally and theoretically.[1-12] They have single spatial mode output powers as high as any single element semiconductor laser[4,5] and have demonstrated long life at very high power.[6] They have been used as the elements in linear[13,14] and Y-guide[15,16] arrays . Originally grown by liquid phase epitaxy (LPE) on n-type[1] and later p-type[2] GaAs substrates, functionally equivalent structures are also grown by metalorganic chemical vapor deposition (MOCVD)[17,18] and molecular beam epitaxy (MBE).[19,20]

In contrast to CSP lasers, Grating Surface Emitting (GSE) lasers are just now moving beyond the "laboratory curiosity" phase, having demonstrated the capability for high power and moderate efficiencies.[21] GSE lasers offer the potential for very high power (> 1W) and high brightness when integrated into coherent one-dimensional[22] and two-dimensional arrays.[23] Although an early GSE laser was based on a conventional CSP structure,[24] recent rapid improvements in GSE performance are a result of advances in 1) material growth technologies which provide quantum well capability and 2) processing technology.

In this paper, we review the lateral guiding mechanism of CSP lasers and compare experimental and analytical results of CSP lasers with geometrical and compositional nonuniformities. Finally, we review the structures and performance of recent GSE lasers.

2. CSP LASERS

2.1. Analysis of CSP lasers

The waveguiding mechanisms of the CSP laser structure (Fig. 1a) have been qualitatively explained in physical terms,[9] and theoretical analyses[7-12] agree that lateral mode confinement results from the combination of a positive real index guide (Fig. 1b) parallel to the junction, with high losses (related to a large imaginary component of the effective index) in the region outside the channel (Fig. 1c). This resulting complex effective index profile provides mode confinement parallel to the junction.
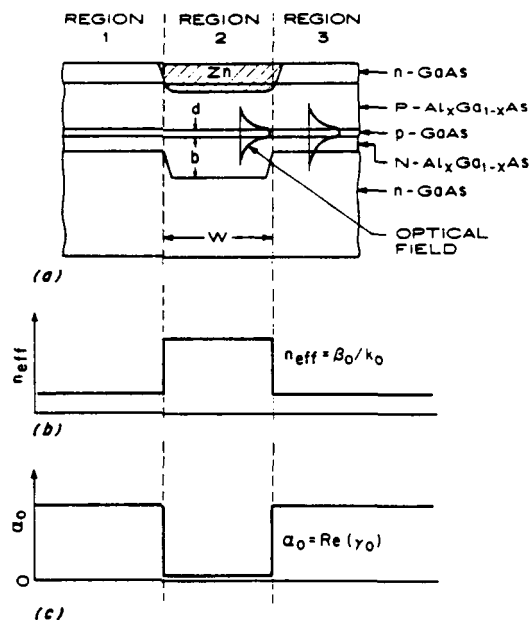

Figure 1. (a) Geometry of a CSP laser, b) real part of the lateral effective index profile, and c) imaginary part of the lateral effective index profile.

The analysis of the near- and far-fields of laser structures can be accomplished using the effective index method as discussed extensively in the literature.[25] The analysis of the lateral modes (along the y-direction) uses the effective index obtained from calculations of the transverse modal field. The fields are written as

$$E_y = E_0 \, u(x,y) \, v(y) \, \exp(j\omega t - \gamma z) \qquad (1)$$

where $\gamma = \alpha + j\beta$ is the complex modal propagation constant. The quantity $u(x,y)$ is the transverse field function and is a solution of the wave equation

$$\partial^2 u / \partial x^2 + [\gamma_0(y)^2 - k_0^2 \, \kappa(x,y)] \, u = 0 \qquad (2)$$

where $\kappa(x,y)$ is the layer dependent complex relative electric permittivity, $\gamma_0(y) = \alpha_0(y) + j\beta_0(y)$ is the transverse complex propagation constant, and k_0 is the free-space wavenumber. Generally the solutions are complex with complex eigenvalues[26] and the fields in the substrate are damped sinusoidal functions as shown in Fig. 2. The solutions for the transverse field functions $u(x,y)$ are obtained in both the channel region ($|y| < W/2$) and the wing region ($|y| > W/2$) by matching the fields and their derivatives at the three interfaces located at $x = 0$, d_2, and d_3; W is the channel width. The lateral field functions $v(y)$ are computed after the complex effective index profile $n_{eff}(y) = -j\gamma_0(y)/k_0$ is determined. In the analysis of the transverse mode functions, we assume the absorption losses in the p-cladding, active layer, and n- cladding layers have values $\alpha_1 = 10 \text{ cm}^{-1}$, $\alpha_2 = 200 \text{ cm}^{-1}$, and $\alpha_3 = 10 \text{ cm}^{-1}$. (The actual value of loss (or gain) in the active layer has an insignificant effect on the value of the complex effective index.) The Al content of the active layer is ~ 7% in order to give a lasing wavelength $\lambda_0 = 0.83 \, \mu\text{m}$. The Al content of the cladding layers is typically 33%. A material absorption value of 10 cm^{-1} is nominally assigned to the cladding layers and the AlAs containing substrates to account for free-carrier losses.
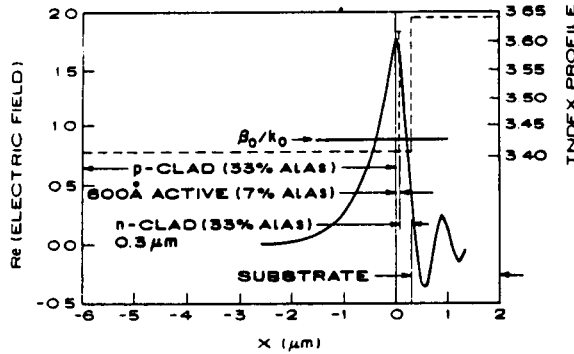

Figure 2a. The real part of the electric field distribution for the transverse profile shown in Fig. 2 with $d_2 = 600$ Å and $\alpha_s = 5000 \text{ cm}^{-1}$.
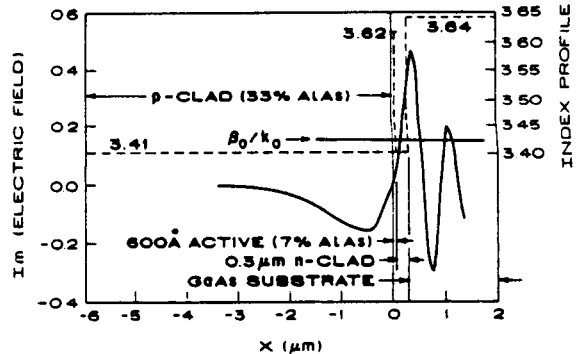
Figure 2b. The imaginary part of the electric field distribution for the transverse profile shown in Fig. 2 with $d_2 = 600$ Å and $a_s = 5000 \text{ cm}^{-1}$.

The far-field intensity pattern is found from the two dimensional Fourier transform of the aperture field distribution and the obliquity factor $g(\theta)$.[27] The two dimensional Fourier transform of the aperture field at the laser facet lying in the $z = 0$ plane is

$$F(k_x, k_y) = E_0 \int_{-\infty}^{\infty} \int_{-\infty}^{\infty} u(x,y) \, v(y) \, \exp[jk_x x + k_y y] \, dx \, dy \qquad (3)$$

where $k_x = k_0 \cos\phi \sin\theta$ and $k_y = k_0 \sin\phi \sin\theta$ and r, θ, and ϕ are the observation point coordinates in the far-field defined by $z = r \cos\theta$, $x = r \sin\theta$, and $y = r \sin\theta \sin\phi$. The transverse radiation pattern is obtained by placing $\phi = 0$ and varying θ. The lateral pattern is obtained by placing $\theta = \pi/2$ and varying ϕ.

2.2. Lateral optical confinement

Waveguiding in CSP lasers appears paradoxical at first glance: Based on intuition for bound modes in dielectric waveguides, one expects that the CSP geometry has a larger effective index (real part) in the region outside the channel since a significant portion of the perpendicular field distribution there "averages in" the high index of the GaAs substrate. In addition, one expects that the large imaginary component of the effective index outside the channel region is due to high absorption (because $\alpha_4 = 5000 - 10000 \text{ cm}^{-1}$ at a lasing wavelength of 0.83 microns[28]) in the GaAs substrate. However, analysis of the CSP structure shows that 1) the effective index (real part) is higher inside the channel than outside (producing a positive index step and corresponding bound lateral modes), and 2) the mode loss outside the channel region increases as the substrate absorption is decreased.

50

The reason for these apparent contradictions is that the transverse field in the regions outside the channel is not a conventional bound mode, but a complex field which radiates some power into the substrate. The conventional bound mode of a passive dielectric waveguide has decaying exponential field solutions in the first and last (the outermost, semi-infinite) layers. A leaky mode[29] has sinusoidal solutions with exponential growth in one or both of the outermost layers. When the outermost layers of an otherwise leaky waveguide have sufficient loss, the field solution is proper (referred to here as a "bound leaky mode") because the fields exponentially decay, albeit the decay is due to the absorption. Conventional bound modes have normalized transverse propagation constants β_0/k_0 that are greater than the refractive indices of the outermost layers. The complex transverse fields ("bound leaky modes") outside the channel have normalized propagation constants less than the refractive index of one (or both) outermost layers.

In Fig. 2, the index of refraction profile of the layers outside the channel region is shown superimposed on a plot of the real (2a) and imaginary (2b) parts of the electric field for the fundamental mode. The magnitude (3.4163) of the normalized longitudinal propagation constant β_0/k_0 (at $y > W/2$) for the fundamental mode, also shown in Fig.2, corresponds to sinusoidal solutions in both the active layer and the substrate. The oscillatory behavior of the fields for $x > 0.36$ is characteristic of a complex field which radiates some power into the substrate. Even in the channel region, the mode perpendicular to the junction is also, strictly speaking, a complex field, but the electric field is so isolated from the substrate by the thick n-clad region that the amplitude of the field oscillations in the substrate is negligible as shown in Fig. 3.
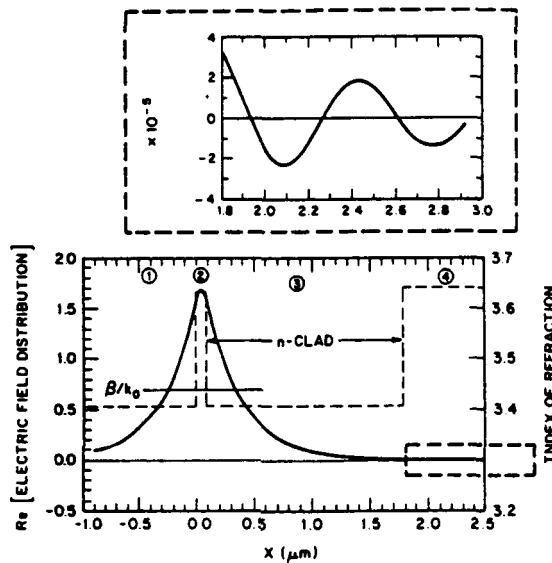

Figure 3.   Index profiles (----) and corresponding electric field distributions (——) for a conventional CSP laser. The layer compositions, thicknesses, and effective index for each structure are listed in Tables 1-3. The dashed rectangles show the field distributions on expanded scales for $x > 1.8$ μm.

Figure 4 shows the near-field intensities (4a) and near-field phases (4b) for the fields perpendicular to the junction in both the regions inside and outside the channel for a CSP structure with $d_2 = 600$ Å and $\alpha_4 = 10,000$ cm^{-1}. Note that the wavefront is tilted at 1.03° for $-1.5 < x < 0.0$ microns and is tilted at about 20.21° for $x > 0.3$ microns for the mode in the regions outside the channel. Since the direction of wave propagation is perpendicular to the wavefront, the wave outside the channel is therefore tilted away from the z-axis of the waveguide and is radiating some energy into the substrate. As the wavefront tilt increases, the guide wavelength λ_z increases (see Fig. 5). Correspondingly, the propagation constant ($\beta = 2\pi/\lambda_z$) and the effective index ($n_{eff} = \beta/k_0$) decrease.

If we assume that the wavelength in the direction of propagation (λ_p) does not change for the fundamental field distribution perpendicular to the junction whether it is inside or outside the channel, we can calculate the average tilt angle of the field distribution from (see Fig. 5)

$$\theta = \cos^{-1}[\lambda_z/\lambda_p] = \cos^{-1}[\beta_0(y=0)/\beta_0(y>W/2)] \qquad (4)$$

For a structure with $d_2 = 600$ Å and $\alpha_4 = 10,000$ cm^{-1}, β_0/k_0 (at $y = 0$) = 3.42315, and β_0/k_0 (at $y > W/2$) = 3.41656 which results in a tilt angle of 3.6° using Eq. (4).

From curves such as Fig. 4b, a plane wave equivalent tilt Θ can be calculated between any two points x_1 and x_2 with corresponding phases (in degrees) $\Phi(x_1)$ and $\Phi(x_2)$ from
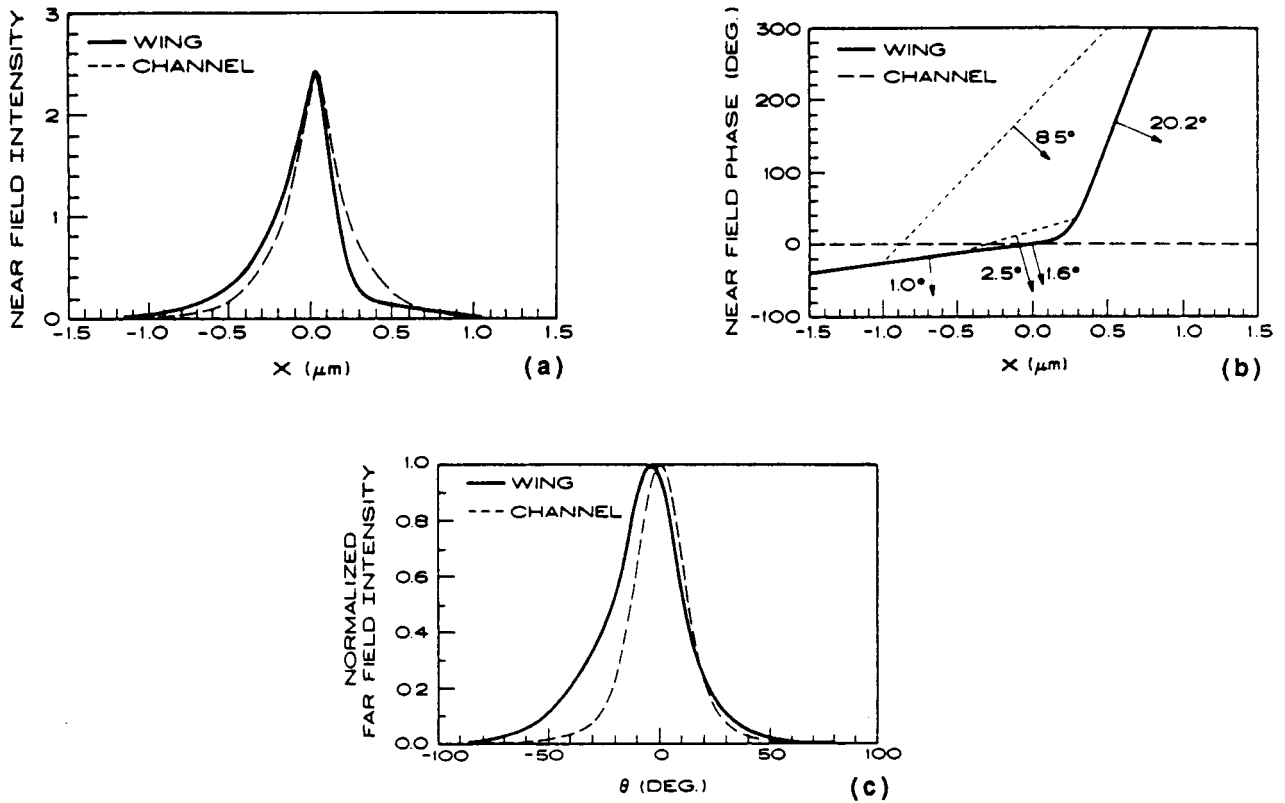
Figure 4. The transverse (a) near field intensity, (b) near field phase, and (c) far field intensity $I_{ch}(\theta)$ and $I_w(\theta)$ for a conventional CSP laser with an active layer thickness of 600 Å in the region inside (———) and outside (----) the channel.

$$\Theta = \tan^{-1}\frac{[\Phi(x_1) - \Phi(x_2)]\lambda_o}{360\ n_{eff}\ [x_1 - x_2]} \tag{5}$$

Indicated in Fig. 4b are plane wave equivalent tilts between the region of nonzero intensity (-1.0 < x < 1.0) of 8.45°, between the $1/e^2$ points in intensity of 2.40°, and between the half power points of 1.6°. Another indication of average tilt of the wavefront can be obtained from the calculated shift of the peak of the far-field intensity pattern (corresponding to the "wing" region, |y| > W/2) which is offset from 0° because of radiation into the substrate.[11,30-32] For the mode perpendicular to the junction outside the channel region, the calculated shift in the far-field peak is 4.0° in air (Fig. 4c), and therefore about 1.2° in the structure.
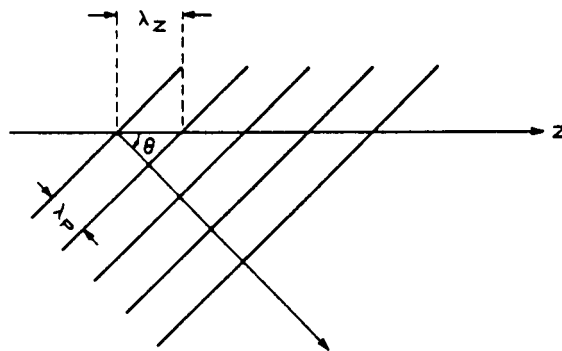

Figure 5. Relationship of the guide wavelength λ_z to the wavelength in the direction of propagation λ_p for a wave propagating at an angle θ with respect to the guide axis.

52

As the substrate absorption is decreased, the envelope of the sinusoidal field distribution in the substrate is less damped. More energy is therefore radiated into the substrate resulting in an increased average wavefront tilt, and both the positive index step and the mode absorption (imaginary part of the effective index) in the region outside the channel increases. Another way to view the increasing mode loss with decreasing substrate absorption is that the "skin depth" of the "bound leaky mode" increases as the substrate becomes less like a perfect conductor. Our calculations show that the mode loss and the lateral index step increase by about 13% and 8% as the substrate absorption decreases from 10,000 cm^{-1} to 0. This increase, although slight, is unexpected from an earlier explanation[9] of CSP waveguiding which predicts that the magnitude of the complex lateral effective index step approaches zero as the substrate absorption decreases towards zero.

2.3. Power dependent interactions

We now review the influence of changes in the profile of the lateral gain and effective index distributions on the opto-electronic properties of CSP lasers. Alterations in gain profiles result from power dependent interactions of the optical field with the electron-hole distribution. In an ideal, symmetric structure alterations of the gain profile produce only slight changes in the full width half power (FWHP) of the near- and far- field patterns. However, slight geometrical asymmetries can cause significant and undesirable shifts in the field patterns with increasing current. Furthermore, these slight asymmetries limit the ultimate emission power.

Several asymmetries can occur during the growth and fabrication of CSP-DH lasers. Asymmetry of the channel (shown in Fig. 6) can occur during etching of the channel into the substrate prior to growth or during the growth by meltback. Zinc diffused regions, used to confine current, may be misaligned with respect to the channel (Fig. 6c). Additionally, asymmetries introduced by nonuniform layer thicknesses and varying compositional properties generally produce variations in effective refractive index, and, if they exist in the active layer, strongly alter the local gain properties.
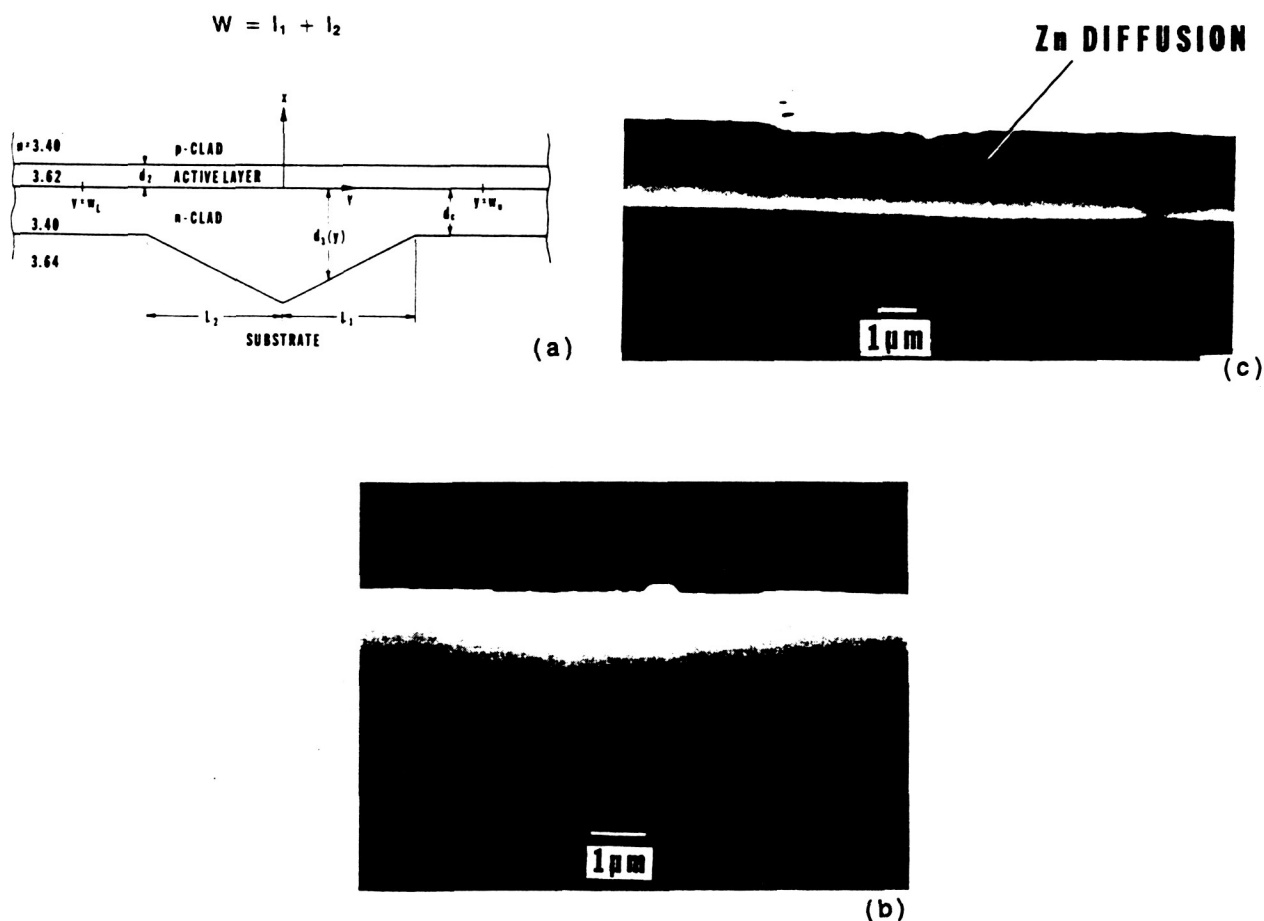

(a)

(b)

(c)

Figure 6. The CSP-DH laser structure: (a) idealized model, (b) scanning electron micrograph illustrating channel asymmetries, and (c) scanning electron micrograph illustrating misalignment of the zinc diffusion with the channel.

53

Computations of the laser characteristics are made using a self-consistent calculation of the optical field and of the electron-hole pair distribution in the active layer.[10] These computations show how small asymmetries in the device geometry affect the optical and electrical properties of the CSP-DH laser. The parameters of the device model include the effects of the various layer thicknesses, refractive indices and material absorption coefficients. Theoretical computations of the opto-electronic properties of symmetrical and asymmetrical configurations show good agreement with experimental measurements made on LPE grown CSP-DH lasers.[14].

<u>2.4. Field analysis</u>

From the solution to the layered waveguide field at specific lateral points, the lateral effective index along the y direction is established (Cf. Fig. 1). When the various layers have loss or gain, the effective index is complex. The absorption in the active layer is accounted for in the expression of the gain profile which we discuss later. The GaAs substrate has a very large absorption coefficient (~ 5000 - 10,000 cm^{-1}) while those of the p- and n- cladding layers are on the order of 10 cm^{-1}. In Eq. (1), the complex function $u(x,y)$ determines the transverse field shape along x, but it is slowly varying (along y) compared to $v(y)$ which defines the lateral field profile. For a lasing mode the eigenvalue γ must satisfy the oscillation condition $Re\{\gamma\} = -G/2$, where $G = -\ln(R_1R_2)/(2L)$ is the modal gain, R_1 and R_2 are the facet reflectivities, and L is the length of the laser. The magnitude of G is equal to the emission losses at the laser facets. The differential equation for the lateral field $v(y)$ satisfies

$$\partial^2 v/\partial y^2 + [\gamma^2 - \gamma_0^2 + k_0^2 \Gamma_c(y) \kappa_\upsilon(y,N_{ph})] v = 0 \tag{6}$$

where $\Gamma_c(y)$ is the complex confinement factor

$$\Gamma_c = \int_0^{d_2} u^2(x,y)dx / \int_{-\infty}^{\infty} u^2(x,y)dx \tag{7}$$

where d_2 is the active layer thickness. For an ideal structure with no loss or gain, the value of Γ_c is real. The complex effective index $n_{eff} = -j\gamma_0/k_0$ where $k_0 = 2\pi/\lambda$ and γ_0 is found from the solution of the transverse problem. The value $\kappa_\upsilon(y,N_{ph})$ is the gain (or carrier) dependent portion of the dielectric constant of the active layer and N_{ph} is the photon density in the active layer. At threshold, $N_{ph} = 0$, and $\kappa_\upsilon(y,N_{ph})$ is determined from the carrier injection and ambipolar diffusion processes in the active layer. Above threshold, $N_{ph} > 0$, and $\kappa_\upsilon(y,N_{ph})$ is then a function of $v(y)$ so that Eq. (6) is nonlinear. In terms of the active layer gain $g(y)$ and index changes due to carrier injection $\delta n(y)$, $\kappa_\upsilon(y,N_{ph})$ can be expressed as[25]

$$\kappa_\upsilon(y,N_{ph}) = 2n_2\delta n(y) + j \, n_2 \, g(y) /k_0 \tag{8}$$

The value $\delta n(y)$ is linearly related to the carrier or gain profile as $\delta n(y) = R \, g(y) / k_0$ where R lies between -1 and -4 for laser structures of the type discussed here.[33] This relates the index change $\delta n(y)$ at a point in the active layer to the gain $g(y)$ at that position using a linear relationship. The solution of Eq. (6) is obtained by numerical methods using a multipoint differential equation solver with prescribed boundary conditions.[34]. Above threshold, the high optical fields in the region below the stripe contact become so intense that electron/hole pairs are depleted at a fast rate. The rate of recombination is proportional to the product of the photon density $N_{ph}(x,y)$ and the optical gain coefficient $g(y)$. Thus, stimulated recombination acts as a sink for carriers while the applied current density is the source. The resulting carrier distribution must be found from solutions of the diffusion equation.

<u>2.4.1. Carrier diffusion.</u> To determine the source and sink terms in the diffusion equation, we must describe the current injection into the active layer as well as the optical fields inside the laser cavity. Computations of the current density distribution $J_x(y)$ in the active layer of various CSP laser structures have been made by using a finite-element code and agree with well known analytical expressions.[35] The exact shape of the current injection profile plays a secondary role in the shape of the carrier profile in the active layer because the ambipolar diffusion process causes carrier redistribution.

The optical hole burning process plays a major role in the nonlinear nature of the electrical and optical properties of the laser. The field inside the cavity can be considered as a superposition of two traveling waves. Because the waves are propagating in opposite directions, there is a quasi-standing wave pattern in the axial direction. Spatial hole burning would occur along the axial direction if carrier diffusion lengths were small. However, since the carrier diffusion length $L_D >> \lambda_g/2$ where λ_g (= $Im\{2 \pi/\gamma\}$) is the guide wavelength, we can neglect this axial variation of the carrier density. The photon density at a point in the axial direction is the sum of the photon densities in the forward and backward traveling waves. The photon density in the active layer is given as a fraction $\Gamma(y)$ of optical power in the transverse direction overlapping the active layer, where

$$\Gamma(y) = \int_0^{d_2} | u(x,y) |^2 dx / \int_{-\infty}^{\infty} |u(x,y)|^2 dx \tag{9}$$

The real function $\Gamma(y)$ is different from the complex function $\Gamma_c(y)$ given in Eq. (7) which is the complex confinement factor that arises from the normalization of the complex-valued wave functions. The total photon density in the active layer becomes

$$N_{ph} = P_o n_{eff} \Gamma(y) \,|v(y)|^2 \,[\exp(Gz) + R_1 \exp(G\{2L - z\})] \, / \, [hvcd_2 <|v(y)|^2>] \qquad (10)$$

where P_o is power in the forward traveling wave at $z=0$ (mirror 2), n_{eff} is the effective modal refractive index, c is the velocity of light, and R_1 is the reflectivity of mirror 1 located at $z = L$ and G is the modal gain coefficient. The term $<|v(y)|^2>$ is the integral of the field intensity over the lateral dimension. The z-dependence of N_{ph} is nearly uniform over the cavity length so that the two exponential terms can be averaged over the length of the cavity.[36] The resulting expression for the stimulated recombination term R_{st} in the diffusion equation becomes

$$R_{st} = 2P_1 \Gamma(y) \,|v(y)|^2 \times \{1 - R_1 - (R_1 R_2)^{1/2} + (R_1/R_2)^{1/2}\} g(y)/[hv \, d_2 <|v(y)|^2> (1 - R_1) \ln(1/R_1 R_2)] \qquad (11)$$

where the emission from the front facet $P_1 = P_o (1 - R_1) \exp(GL)$, and P_o is the power inside the laser at $z = 0$.

The necessary source and sink terms in the diffusion equation are now completely defined. Letting $N(y)$ denote the electron-hole pair density, the diffusion equation becomes

$$D_e \, \partial^2 N(y)/\partial y^2 - N(y)/\tau_s - BN^2(y) = -J_x(y)/[qd_2] + R_{st} \qquad (12)$$

where $D_e \, (=L_D^2/\tau_s)$ is the effective diffusion coefficient, τ_s is the spontaneous carrier lifetime, and B is the bimolecular recombination term. The gain coefficient is expressed as

$$g(y) = a \, N(y) - b \qquad (13)$$

In GaAs active layers, we use $a = 2.5 \times 10^{-16} \, cm^2$ and $b = 190 \, cm^{-1}$.[37]

Substitution of the gain expression into Eq. (12) gives a differential equation for the carrier density where the term P_1 is the emission power out of the front facet, assumed as a parameter, and the wave function $v(y)$ is a solution to Eq. (6). Of course, self-consistency requires the simultaneous solution of both the wave equation which has a dielectric constant that is carrier dependent and the carrier diffusion equation which has an optical field dependence. The flow chart in Fig. 7 illustrates our self-consistent method of solution.
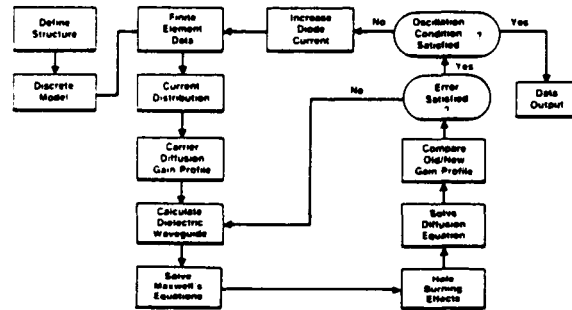

Figure 7. Flow chart summarizing the numerical calculations for laser oscillation above threshold.

2.5. Results and discussion of geometrical asymmetries

The basic laser structure is illustrated in Fig. 1, and Table 1 gives the parameters used in the calculations. In the following discussion, we consider a symmetrical CSP laser where the Zn diffusion is symmetrically located over the channel. For the asymmetrical structures, we first assume that the slope of the walls of the channel are different, with the Zn diffused region symmetrical about $y = 0$. Next we study the effects of a misaligned (relative to the channel) Zn diffused region over a symmetrical channel. In the cases shown in Figs. 8-10, and 12a, the width S of the Zn diffused region is 4 μm, the same as the width of the symmetric channel. In Fig. 12b, S = 6 μm which is larger than the channel. In Figs. 8-10, we show (a) the effective index, (b) the gain distribution in the active layer, (c) the near field intensity and (d) the far-field radiation patterns at various emission powers. At threshold, the gain in the active layer (Figs. 8-10, 12) is distributed according to the diffusion of carriers in the absence of hole burning.

For the symmetric waveguide, the dimensions are $l_1 = l_2 = 2$ μm while for the asymmetric case (Fig. 9), $l_1 = 2$ μm, and $l_2 = 1.7$ μm. This range of values is not atypical for our fabrication process. Differences in lengths l_1 and l_2 arise during fabrication as discussed earlier and can be associated with, for example, the crystal orientation so that both chemical etch rates and meltback rates can be different for the two sloping walls of the channel. Other effects of asymmetries can arise due to the asymmetrical growth of AlGaAs in the sloping channels.

TABLE 1. CSP MODELING PARAMETERS

	Cladding Layers	Active Region	Substrate
Mole Fraction AlAs	0.30	0.07	0.0
Refractive Index	3.40	3.62	3.64
Absorption Coefficient	10 cm⁻¹	--	5000 cm⁻¹

$\lambda = 0.83$ μm (lasing wavelength)

$d_2 = 0.06$ μm (active layer thickenss)

$B = 10^{-12}$ cm³/sec (bimolecular coefficient)

$L_D = 3$ μm (carrier diffusion length)

$\tau_s = 3 \times 10^{-9}$ sec (carrier lifetime)

$R_1 = 0.32$

$R_2 = 0.85$ (facet reflection coefficients)

$d_c = 0.4$ μm (nclad layer thickness outside of the channel)

$y_o = 0.5$ μm (current decay parameter)

$S = 4$ μm (stripe width)

$L = 250$ μm (device length)

For a perfect CSP laser, both the effective index (Fig. 8a) and the carriers (Fig. 8b) are distributed symmetrically about the center of the waveguide for all power levels. However, for $l_1 > l_2$, the effective index at threshold (Fig. 9a) is asymmetric with a corresponding shift of the peak near field intensity (Fig. 9c) along the positive y axis. Although the gain distribution (Fig. 9b) appears symmetric at threshold, the gain profile is redistributed asymmetrically with increasing power with the highest peak of the gain distribution occurring on the negative y axis. This redistribution of the gain profile with drive for the asymmetric case is a result of the near field intensity distribution (Fig. 9c) preferentially saturating the gain (Fig. 9b) along the positive y axis. The asymmetry of the lateral gain in turn forces the effective index profile to become even more asymmetric (the lateral effective index step increases more along the negative y axis than along the positive y axis) because of the gain-induced refractive index depression effect--which causes an increase in the shift

Figure 8. Calculated (a) lateral effective index profiles, (b) lateral gain profiles in the active layer, (c) near field intensity distributions, and (d) far field intensity patterns for a symmetric CSP-DH structure ($l_1 = 2.0$ μm and $l_2 = 2.0$ μm) with a 4 μm wide Zn diffusion front for output powers of 0, 10, 20, 30, 40, and 50 mW.
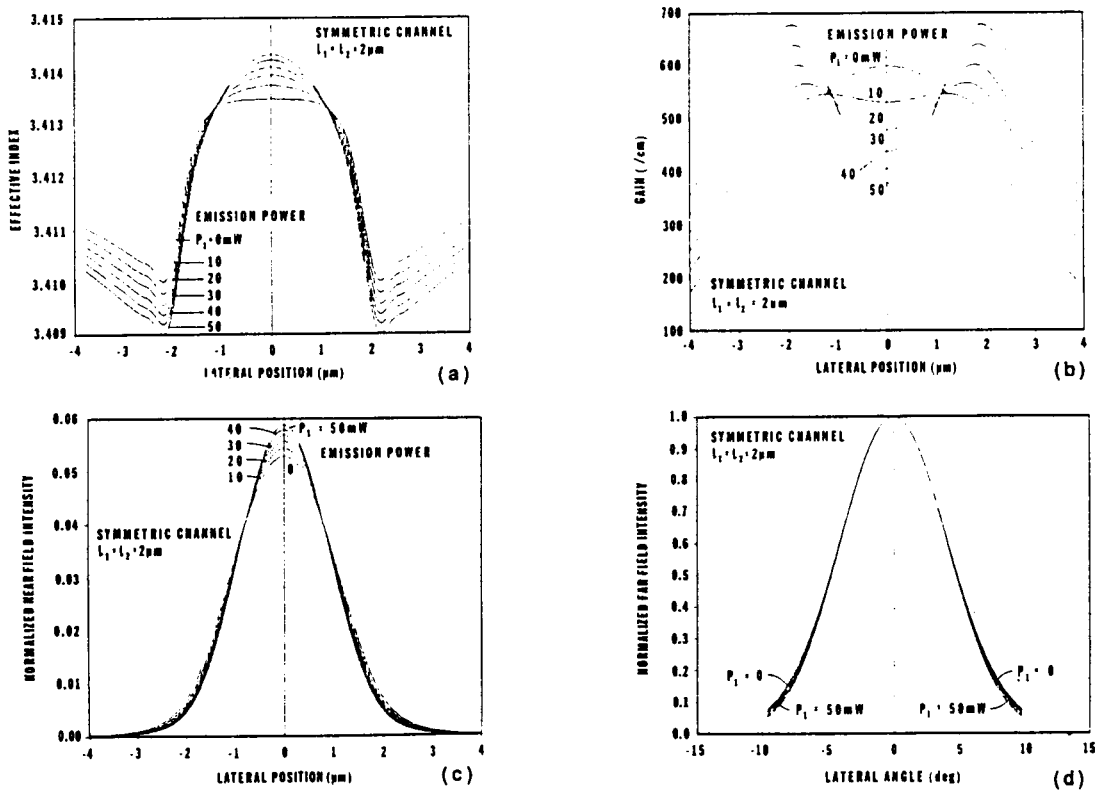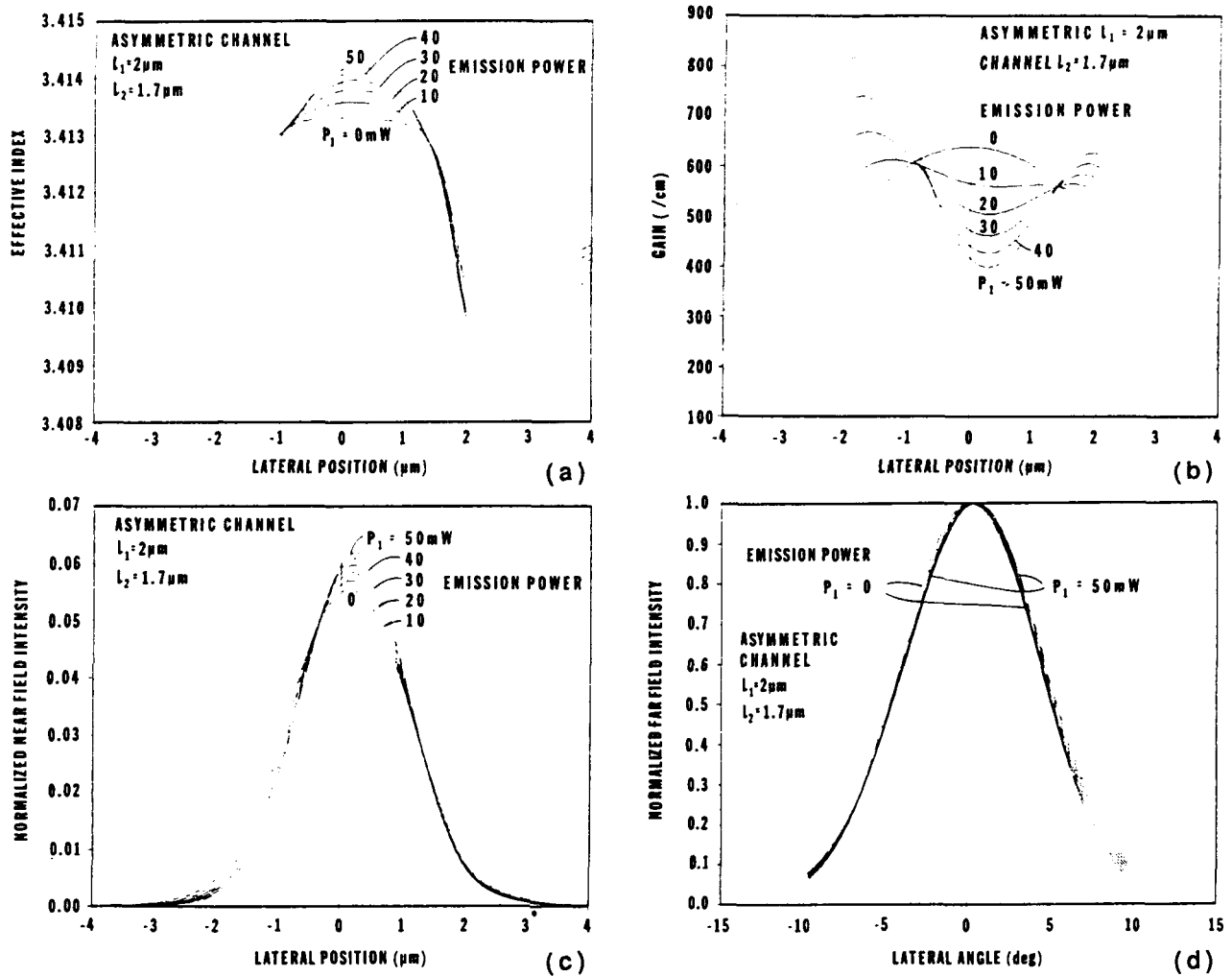
Figure 9. Calculated (a) lateral effective index profiles, (b) lateral gain profiles in the active layer, (c) near field intensity distributions, and (d) far field intensity patterns for an asymmetric CSP-DH structure ($l_1 = 2.0$ μm and $l_2 = 1.7$ μm) with a 4 μm wide Zn diffusion front for output powers of 0, 10, 20, 30, 40, and 50 mW.

of the optical field in the positive y direction with drive (as much as 0.25 μm at 50 mW as shown in Fig. 9(c)). As this interplay between the effective index profile, gain distribution, and near field intensity continues, the central peak of the near field distribution increasingly shifts along the positive y axis while the magnitude of the gain distribution increases much more along the negative y axis than along the positive y axis.

For a strongly asymmetric CSP structure, the interplay between the effective index profile, gain distribution, and near field intensity can limit the output power to a few tens of milliwatts: In Fig. 10, the 4 μm wide Zn diffused region of a symmetric channel CSP laser is displaced 0.5 μm along the negative y direction. For this case, the slight asymmetry in the effective index (Fig. 10a) near threshold is drastically enhanced as the peak of the near field distribution (Fig. 10c) increasingly shifts along the positive y axis, increasing the gain (Fig. 10b) almost exclusively along the negative y axis. As a result, the power in such a device saturates since increased drive current reduces the the interaction of the lasing mode with the gain and prevents saturation of the spontaneous emission. For this theoretical case, the total emission power of the fundamental mode could not be increased above approximately 30 mW at current levels above 125 mA as shown in Fig. 11.

If the misalignment of the Zn diffusion is less, or the width of the Zn diffused region is larger than the channel width, the device behavior is similar to the case of a CSP laser with an asymmetric channel (Fig. 9). The gain distribution for a 4 μm wide diffusion front displaced 0.2 μm is shown in Fig. 12a while that of a 6 μm wide diffusion front displaced 0.5 μm is shown in Fig. 12b. In both cases the symmetric channel is 4 μm wide. Not only are the gain distributions shown in Fig. 12 similar to the gain distribution shown in Fig. 9b, the effective index, near field distribution, and far field pattern curves for the two cases shown in Fig. 12 are very similar to the corresponding curves shown in Fig. 9. The near field shifts corresponding to the cases shown in Figs. 12a and 12b were both about 0.25 μm at 50 mW (the same as the asymmetric channel case shown in Fig. 8c) and the far field peak shifts were both about 0.8° at 50 mW (slightly more than the asymmetric channel case shown in Fig. 8d). For the strongly asymmetric CSP structure of Fig. 10, the near field peak shifts about 0.6 μm and the far-field peak moves about 2.5° as the output power increases from threshold to 30 mW. These
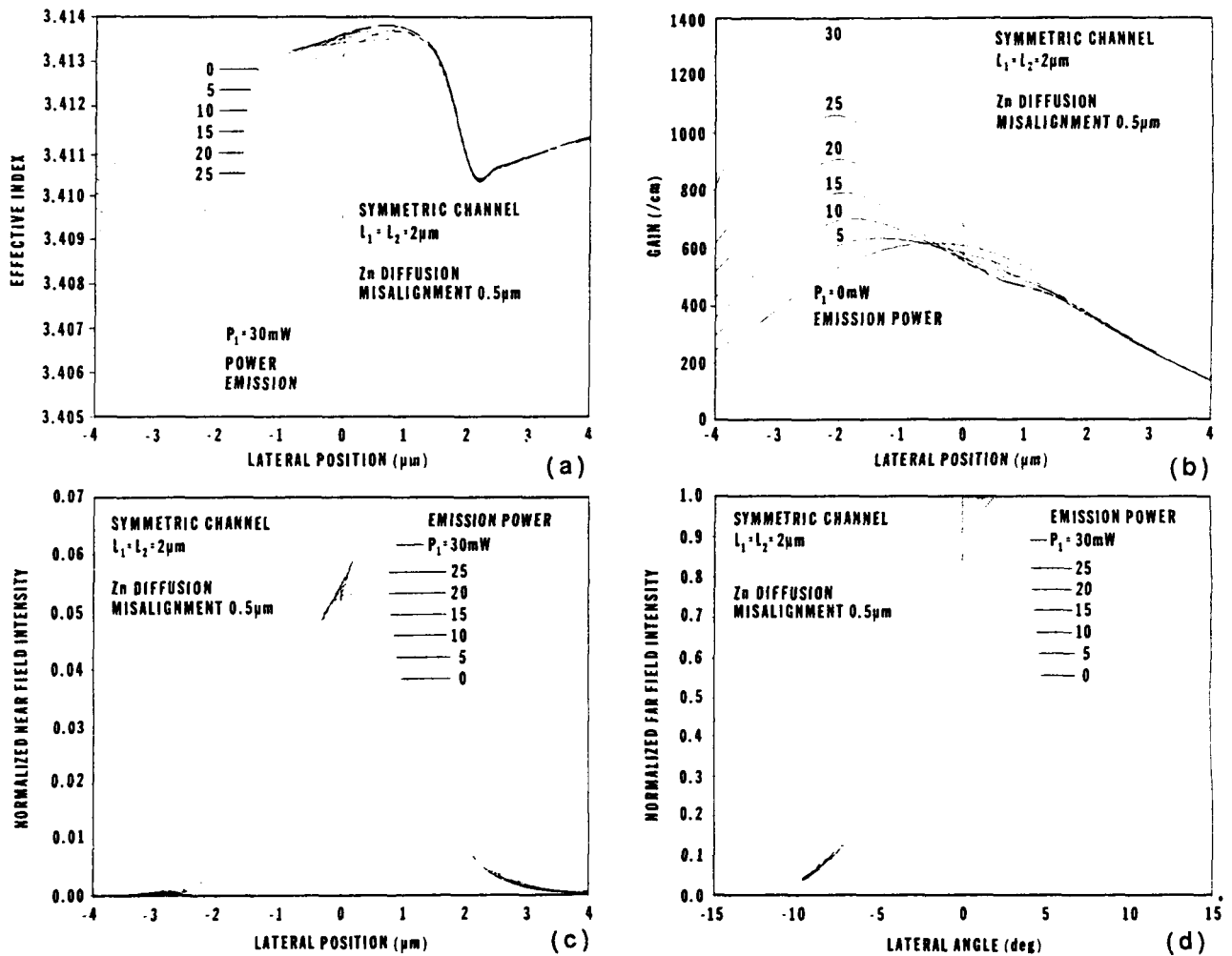
Figure 10. Calculated (a) lateral effective index profiles, (b) lateral gain profiles in the active layer, (c) near field intensity distributions, and (d) far field intensity patterns for a symmetric CSP-DH structure (l_1 = 2.0 µm and l_2 = 2.0 µm) with a misaligned 4 µm wide Zn diffusion front for output powers of 0, 5, 10, 15, 20, 25, and 30 mW. The Zn diffusion is centered at y = -0.5 µm.

near and far field shifts occur with asymmetries in the CSP structure because the gain-induced refractive index perturbation has a magnitude comparable to the "built-in" effective index profile. If the "built-in" effective index profile was large compared to the gain-induced index perturbations, the near- and far- fields should be stable with drive.

Because the gain in a CSP laser is predominantly above the channel, one expects that the lateral effective index step decreases with increasing drive. However, calculations indicate that the opposite occurs: the carriers are depleted in the center of the channel (Fig. 8b-10b, 12) by the optical field (which increases the effective index in the center of the channel), the gain is largest near the channel edges (which decreases the effective index outside of the channel) and the lateral effective index step is increased. This explanation is also consistent with astigmatism and phase front measurements made on CSP lasers[24] which show no measurable change with increasing power.

For both the symmetric and asymmetric cases, the full width at half power (FWHP) of the far-field pattern increases with increasing output power, although in the symmetric case, the increase is comparable to experimental error (a few tenths of a degree). The increase in the FWHP of the far-field pattern is due to narrowing of the near field intensity (Fig. 8c-10c) as the lateral effective index step (Fig. 8a-10a) increases with increasing power output. Experimental measurements showing the increase in FWHP of the far-field pattern with power for a CSP laser appear in Fig. 3 of reference 13.

In Fig. 13(a), the calculated values of the optical emission from the front facet (front facet reflectivity R_1 = 0.32, rear facet reflectivity R_2 = 0.85) for the four cases described in Figs. 8, 9, 10, and 12 as a function of the device drive current is shown. In the computations, we have assumed the internal quantum efficiency is unity and there is no loss of carriers transversing heterojunctions. Therefore, the current axis can be scaled to account for known leakage in realistic devices. Both the threshold currents and slope efficiencies are different for the different cases. For the symmetric CSP, I_{th} = 22 mA, while it is approximately 24 mA for the asymmetric channel case. Note that increasing the Zn diffusion front from 4 µm to 6 µm results in only a slight decrease in the external differential quantum efficiency. Figure 13(b) shows an experimental P-I curve of a typical CSP laser with minimal asymmetries and with geometry, composition, and facet coatings comparable to the numerical examples. Experimentally, thresholds as low as 37 mA were measured.
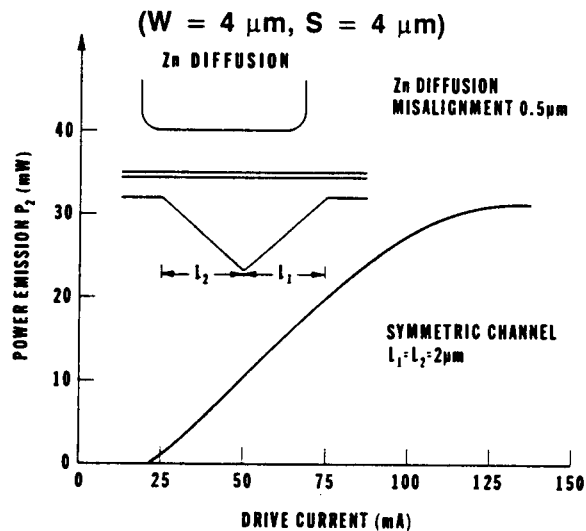
58

Figure 11. Calculated power versus current curves for a CSP-DH structure with a symmetric ($l_1 =$ 2.0 μm and $l_2 = 2.0$ μm) channel, and a 4 μm wide diffusion front which is offset from the channel by 0.5 μm.
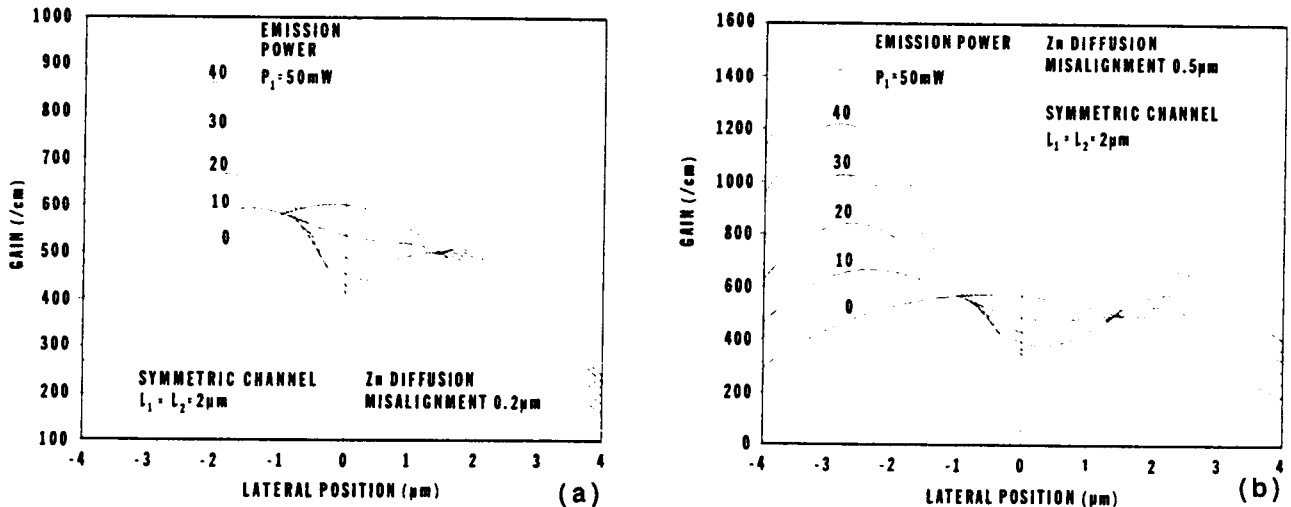

Figure 12. Calculated lateral gain profiles in the active layer for a symmetric CSP structure for output powers of 0, 10, 20, 30, 40, and 50 mW with (a) a misaligned 4 μm wide Zn diffusion front centered at y = -0.2 μm, and (b) a misaligned 6 μm wide Zn diffusion front centered at y = -0.5 μm.
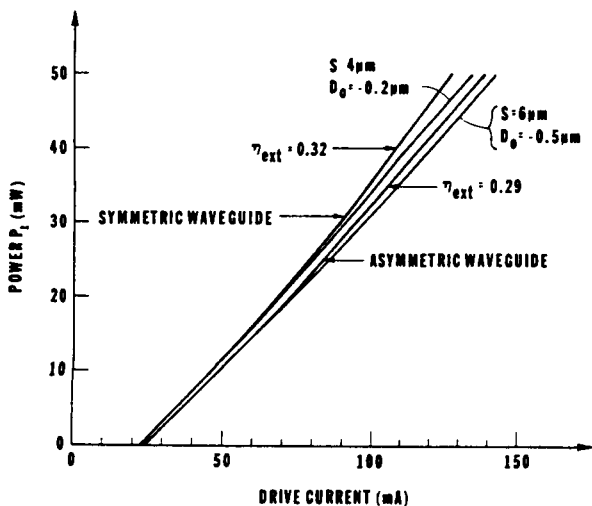
Figure 13. Calculated power vs current curves for a CSP-DH structure with 1) a symmetric ($l_1 = 2.0$ μm and $l_2 = 2.0$ μm) channel, symmetric 4 μm wide diffusion front (...); 2) an asymmetric ($l_1 = 1.7$ μm) channel, symmetric 4 μm wide diffusion front (....); 3) a symmetric ($l_1 = 2.0$ μm and $l_2 = 2.0$ μm) channel, misaligned 4 μm wide diffusion front centered at y = -0.2 μm (....); and a symmetric ($l_1 = 2.0$ μm and $l_2 = 2.0$ μm) channel, misaligned 6 μm wide diffusion front centered at y = -0.5 μm (....). The device geometry is shown in Fig. 1 and the numerical parameters given in Table 1.

59

2.6. AlAs composition variation

Another problem that may occur with CSP lasers is a variation of the AlAs composition in the channel region. We have found CSP lasers that have an increased AlAs concentration at the bottom of the channel, and others that have a decreased AlAs concentration at the bottom of the channel. In the case that there is a higher concentration of AlAs at the bottom of the channel, the original CSP index profile is changed into that of a Large Optical Cavity (LOC)--which can even be beneficial.[11] However, if there is less AlAs at the bottom of the channel, the resulting inadvertent fourth layer can act as an index matching layer which enhances the coupling of the field distribution to the substrate and increases the mode loss.[11] We have called such defective units Enhanced Substrate Loss (ESL) CSP lasers. In Fig. 14, the solid black line is the ratio of the mode energy in the substrate to the total mode energy for an ESL CSP laser as the AlAs composition of the bottom half of the channel is varied from 0 to 33%. The peaks correspond to resonances or "best" matching conditions. Shown in the insets are several far-field patterns corresponding to different AlAs compositions. Even away from the peaks, these perpendicular far-fields are quite asymmetric--with their peaks tilted off-axis towards the substrate. Fig. 15 shows several experimental far-fields from different devices from a wafer which was known to have AlAs variations in the channel. Such AlAs composition variations are almost the only explanation for asymmetric perpendicular far-fields in any AlGaAs semiconductor laser.
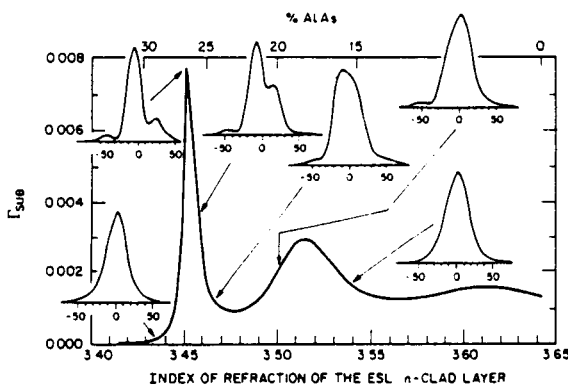

Figure 14. The substrate confinement factor Γ_s as a function of the % AlAs (or index of refraction at $\lambda = 0.83$ μm) of the n-clad layer at the bottom of the channel of an ESL-CSP laser. The inset far field intensity vs angle patterns show a large variation in asymmetry as a function of % AlAs of the n-clad layer.
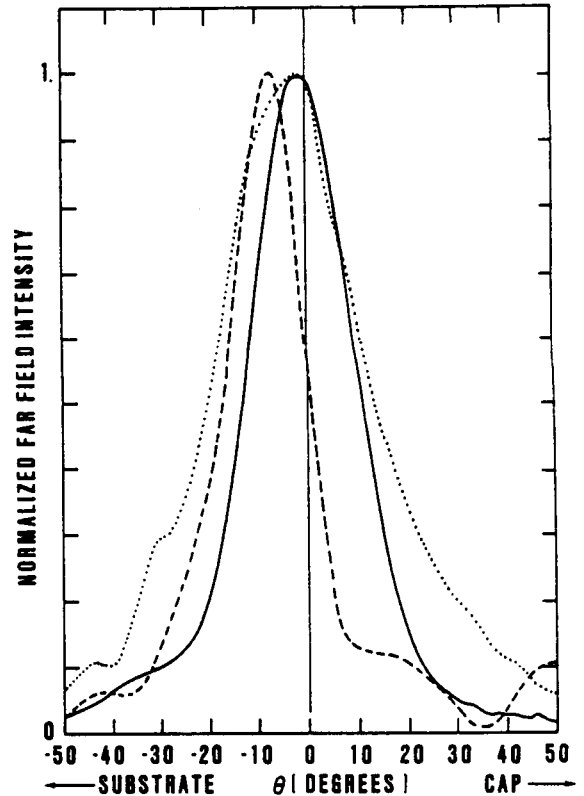

Figure 15. Experimentally measured far field intensity patterns for ESL-CSP lasers.

2.6.1. Performance considerations.

Although the large imaginary part of the effective index outside the channel region of a CSP laser helps stabilize the mode, it also increases the threshold current and decreases the differential quantum efficiency. Using the computational procedure described above, the power versus current curves for a CSP type laser, a ridge guide laser with cladding layer losses of 10 cm^{-1}, and a lossless ridge guide laser (all with active layer thicknesses of 600 Å) are calculated in Fig. 16. All three structures have the same lateral index step (6.822 x 10^{-3}) and profile (see inset of Fig. 16) with a channel or ridge width of 4 μm. The large differences in threshold current and differential quantum efficiency are due to the reduced losses outside the ridge of the two ridge structures compared to the high losses outside the channel for the CSP device.

The value of the injected current at which the first order lateral mode reaches threshold was also calculated for the three structures in Fig. 16. While the first order mode of the ridge structures reached threshold at power levels in the 10 to 20 mW range, the first order mode of the CSP structure was only approaching transparency at 200 mW. Since the channel and ridge widths are equal in these calculations, we must note that 4 μm is a relatively narrow channel for a CSP laser, while 4 μm is relatively wide for a ridge guide. As the CSP channel is widened from 8 μm to 12 μm, the power level at which the first higher order lateral mode reaches threshold is reduced from about 100 mW to 30 mW. As the width of the ridge is reduced to 2 μm, the first higher order lateral mode is calculated to reach threshold at about 50 mW. Such calculations indicate that the onset of higher order modes is not a significant effect in CSP lasers of common channel widths (less than 8 μm). Rather, variations and irregularities in the output characteristics of CSP lasers are more likely due to compositional variations[11] and geometrical asymmetries.[10,12]

For the devices in Fig. 16, $\Delta\alpha_0/k_0 = 0$ for the ridge guide structures and 5.074×10^{-3} for the GaAs substrate CSP laser.
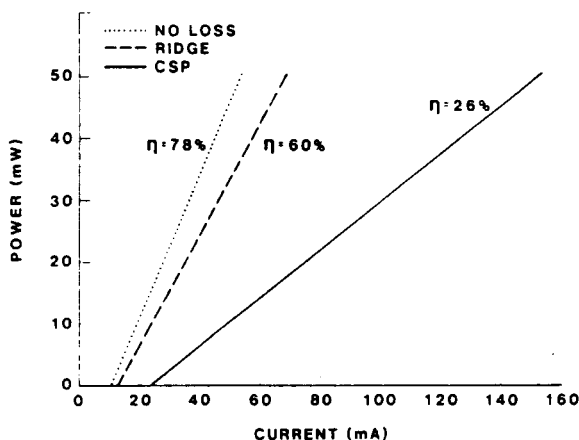

Figure 16. Calculated power versus current curves for a conventional CSP laser (——), a conventional ridge guide laser (----), and a lossless ridge guide laser (···).

3. GRATING SURFACE EMITTING LASERS

Grating Surface Emitting (GSE) lasers use a grating in first order to couple light out perpendicular to the plane of the wafer. The same grating is used in second order to provide feedback for laser oscillation. Use of a grating allows a large increase in the size of the output aperture, reducing the beam divergence by one or two orders of magnitude compared to edge-emitters. In addition, the grating provides dynamic wavelength stabilization of 30 to 40 dB.

Early GSE devices were gain guided and extremely inefficient when operated at either room temperature or liquid nitrogen temperatures.[39-43] An early index guided GSE laser was based on a CSP structure[24] and demonstrated a one-quarter degree beam divergence (equivalent to the diffraction limit) and 40 dB sidemode rejection, although the power and efficiency remained very low compared to conventional edge-emitters.

To improve efficiency, optical confinement was obtained by using a ridge guide, eliminating the characteristic substrate radiation of CSP structures.[21] Also to improve efficiency, a Graded Index Separate Confinement Heterostructure Single Quantum Well (GRINSCH-SQW) epilayer geometry (see Fig. 17) was used. The cladding layers are approximately 80% AlAs, graded to 40% AlAs over a distance of 0.2 μm, with a GaAs quantum well. A completely processed single element ridge-guided GSE is shown in Fig. 18. If the top of the waveguide in the grating region is 1000Å above the graded region while 600 Å of p-clad remains outside the ridge, an index step of about 8×10^{-3} and 4×10^{-3} is achieved for the active and passive sections, respectively. The top inset in Fig. 18 shows an SEM micrograph of the transition between the gain and grating region. The second inset is an SEM of the grating region. As shown in Fig. 19, single element GSE's are capable of more than 150 mW peak output power with a differential quantum efficiency of 30%. The emitting aperture, which consisted of a 200 μm long active region and two 250 μm long grating sections had a diffraction limit of 0.06°, which corresponded to the measured beam divergence (Fig. 20).
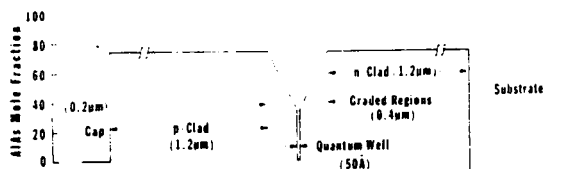

Figure 17. The composition and dimensions of the GRINSCH-SQW structure.

The characteristics of these single element, ridge-guided GSE devices were obtained by probe testing the lasers junction side up in wafer form with 50 ns current pulses, no dc bias, and a 2% duty cycle. Under these severe modulation conditions, the spectral output of the laser was single wavelength with 20 - 45 dB side mode rejection around the central peak at 8500 Å. The spectrum shown in Fig. 21 was taken at 70 mW.

The operation of coherent linear arrays of a GRINSCH-SQW GSE lasers has been reported.[22] A seven element array was gain-guided and produced more than 400 mW peak power with a differential quantum efficiency of 15% (Fig. 22). The spectrum of the seven element GSE at 250 mW is shown in Fig. 23 and is predominantly single-mode at 8577 Å, with a sidemode 17 dB down at 8578 Å. The measured beam divergence of the far-field from the seven element array, shown in Fig. 24, was 0.012°. The total extent of the array was about 4 mm. A uniformly illuminated 4 mm aperture would have a diffraction limited beam divergence of 0.011° -- which is within the experimental error of the measurement.

61
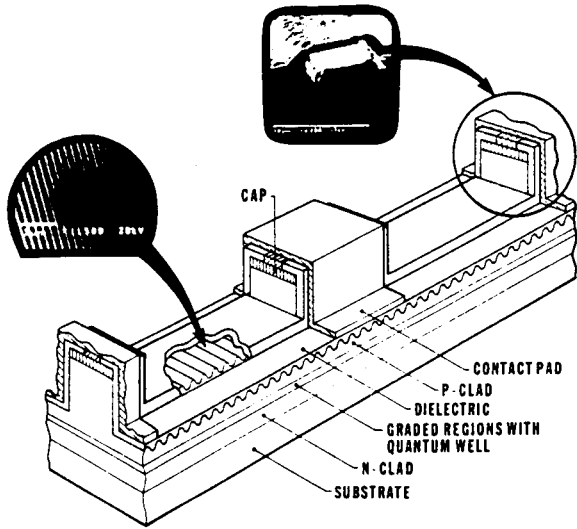
Figure 18. Schematic drawing of the GRINSCH-SQW surface emitting laser; insets show a scanning electron micrograph of 1) the transition between the gain and DBR sections and 2) the grating in the DBR section.
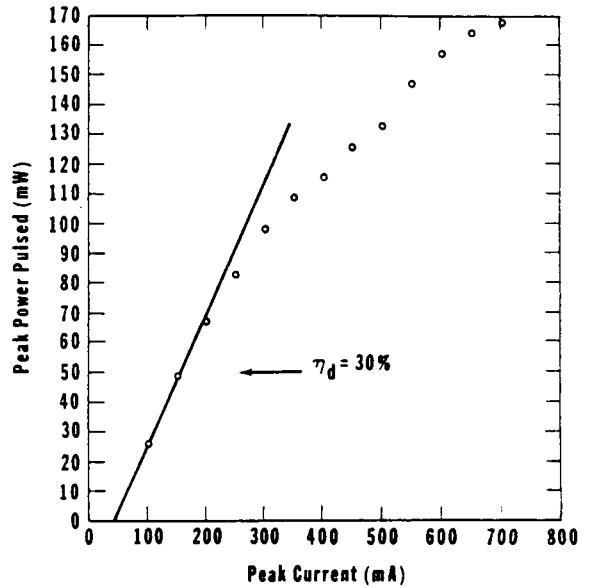
Figure 19. Power versus current curve for a ridge-guided GRINSCH-SQW surface emitting laser with a 200 μm long gain section between 500 μm long waveguide sections. The external differential quantum efficiency η_d is 30%.
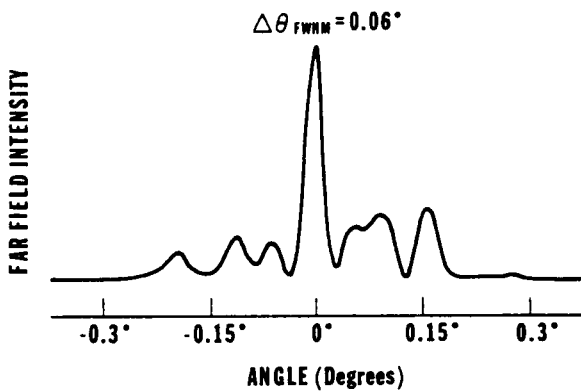
Figure 20. Far field pattern of a ridge-guided GRINSCH-SQW grating surface emitting laser in the direction normal to the grating lines.
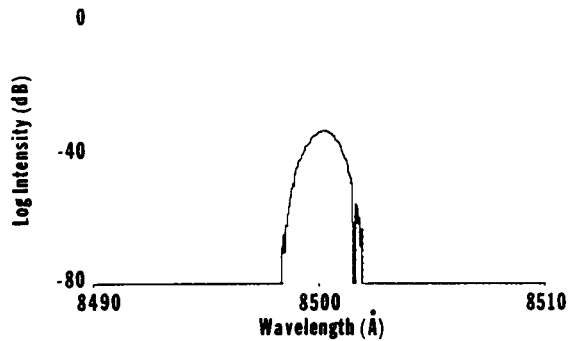
Figure 21. Semilog plot of the surface emitted mode spectrum at an output of 70 mW showing 20-40 dB dynamic wavelength sidemode rejection. Instrument resolution is 1 Å.

62
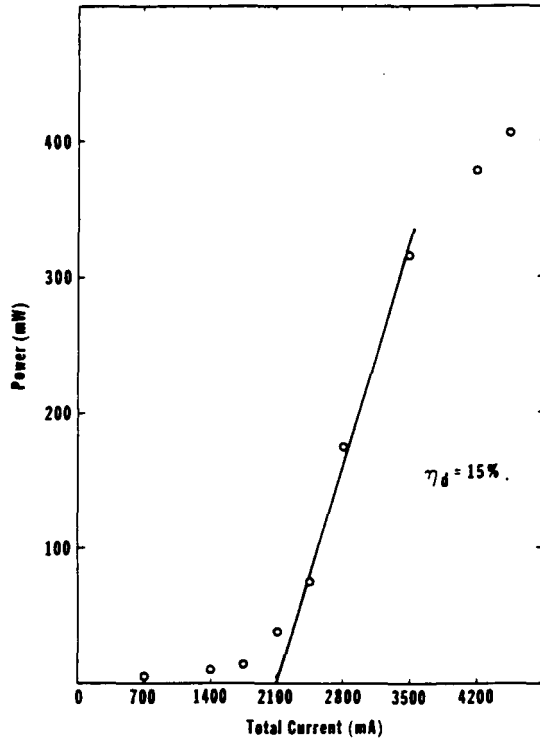
Figure 22. Power vs current curve for a seven element GSE laser array.

Figure 23. Spectral output of a seven element GSE laser array.

Figure 24. Far field intensity pattern (measured along the axis of the array) of a seven element GSE laser array.

4. CONCLUSIONS

To summarize, the advantages and disadvantages of the devices discussed in this paper are listed in Table 2. CSP lasers, because of their excellent mode discrimination, can have wide channels resulting in moderate peak power densities at the output facet. However, mode discrimination comes at the expense of increased threshold current and decreased efficiency. This mode discrimination of CSP lasers, caused by radiation into the substrate, has been used effectively to force an edge-emitting array to operate in a single array mode[44] with near diffraction limited characteristics.[45] Edge emitting ridge guides (and this would also apply to buried heterostructure lasers) can have very low threshold currents and high efficiencies -- but to eliminate higher order mode oscillation, must have small spot sizes resulting in high peak power densities at the output facet. Finally, Grating Surface Emitters--because they can have extremely large emitting apertures, will never be performance limited by catastrophic optical damage. With increasing development of Grating Surface Emitters, we expect that their threshold currents and efficiencies will equal that of the best edge emitters.

63

TABLE 2. DEVICE COMPARISON

DEVICE	PLUS	MINUS
CSP	EXCELLENT MODE DISCRIMINATION; MODERATE P_D	MODERATE η_{DQE} MODERATE I_{TH}
RIDGE (BURIED HET)	LOW I_{TH} HIGH η_{DQE}	HIGH P_D MODERATE MODE DISCRIMINATION
RIDGE GSE	VERY LOW P_D ⌐ LOW I_{TH} ⌐ HIGH η_{DQE} (FUTURE)	MODERATE MODE DISCRIMINATION; ⌐ MODERATE I_{TH} ⌐ MODERATE η_{DQE} (PRESENT)

5. REFERENCES

1. K. Aiki, M. Nakamura, T. Kuroda, J. Umeda, R. Ito, Naoki Chinone, and M. Maeda, "Transverse mode stabilized $Al_xGa_{1-x}As$ injection lasers with channeled-substrate-planar structure," IEEE Journal of Quantum Electronics QE-14(2), 89-94, (1978).

2. S. Yamamoto, H. Hayashi, S. Yano, T. Sakurai, and T. Hijikata, "Visible GaAlAs V-channeled substrate inner stripe laser with stabilized mode using p-GaAs substrate," Appl. Phys. Lett. 40(5), 372-374 (1982).

3. S. Yamamoto, N. Miyauchi, S. Maei, T. Morimoto, O. Yamamoto, S. Yano, and T. Hijikata, "High output power characteristics in broad-channeled substrate inner stripe lasers," Applied Physics Letters 46(4) 319-321 (1985).

4. K. Hamada, M. Wada, H. Shimizu, M. Kume, F. Susa, T. Shibutani, N. Yoshikawa, K. Itoh, G. Kano, and I. Teramoto, "A 0.2W cw laser with buried twin-ridge substrate structure," IEEE J. Quantum Electron. QE-21(6), 623-628 (1985).

5. B. Goldstein, M. Ettenberg, N. A. Dinkel, and J. K. Butler, "A high-power channeled-substrate-planar AlGaAs laser," Appl. Phys. Lett. 47, 655-657 (1985).

6. T. Shibutani, M. Kume, K. Hamada, H. Shimizu, K. Itoh, G. Kano, and I. Teramoto, "A novel high-power laser structure with current-blocked regions near cavity facets," IEEE J. Quan. Electron. QE-23(6), 760-764 (1987).

7. T. Kuroda, M. Nakamura, K. Aiki, and J. Umeda, "Channeled-substrate-planar structure $Al_xGa_{1-x}As$ lasers: an analytical waveguide study," Applied Optics, 17(20), 3264-3267 (1978).

8. K. A. Shore, "Above-threshold analysis of channelled-substrate-planar (CSP) laser," IEE Proc. Part I, 9-15 (1981).

9. S.Wang, C. Chen, A. S. Liao, and L. Figueroa, "Control of mode behavior in semiconductor lasers," IEEE Journal of Quantum Electron.QE-17(4), 453-468 (1981).

10. J. K. Butler, G. A. Evans, and B. Goldstein, "Analysis and performance of channeled-substrate-planar double-heterojunction lasers with geometrical asymmetries," IEEE J. Quan. Electron. QE-23(11) 1890-1899 (1987).

11. G. A. Evans, B. Goldstein, and J. K. Butler, "Observations and consequences of non-uniform aluminum concentrations in the channel regions of AlGaAs channeled-substrate-planar lasers," IEEE J. Quan. Electron. QE-23(11), 1900-1908 (1987).

12. T. Ohtoshi, K. Yamaguchi, C. Nagaoka, T. Uda, Y. Murayama, and N. Chinone, "A two dimensional device simulator of semiconductor lasers," Solid-State Electronics 30(6), 627-638 (1987).

13. T. Kadowaki, T. Aoyagi, S. Hinata, N. Kaneno, Y. Seiwa, K. Ikeda, and W. Susaki, "Long-lived phase-locked laser arrays mounted on a Si-submount with Au-Si solder with a junction-down configuration," IEEE International Semiconductor Laser Conference, Kanazawa, Japan, Conference Program and Abstract of Papers, 84-85 (1986).

14. B. Goldstein, N. Dinkel, N. W. Carlson, G. A. Evans, and V. J. Masin, "Performance of a channeled-substrate-planar high-power phase-locked array operating in the diffraction limit," Conference on Lasers and Electro-Optics, Baltimore, Technical Digest, 330-331 (1987).

15. M. Taneya, M. Matsumoto, S. Matsui, S. Yano, and T. Hijikata, "0º phase mode operation in phased-array laser diode with symmetrically branching waveguide," Appl. Phys. Lett. 47(4), 341-343 (1985).

16. D. F. Welch, P. Cross, D. Scifres, W. Streifer, and R. D. Burnham, "In-phase emission from index-guided laser array up to 400 mW," Electronics Letters 22(6), 293-294 (1986).

17. K. Uomi, S. Nakatsuka, T. Ohtoshi, Y. Ono, N. Chinone, and T. Kajimura, "High-power operation of index-guided visible GaAs/GaAlAs multiquantum well lasers," Appl. Phys. Lett. 45(8), 818-821(1984).

18. J. J. Yang, C.S. Hong, J. Niesen, and L. Figueroa, "High-power single longitudinal mode operation of inverted channel substrate planar lasers," J. Appl. Phys 58, 4480-4482 (1985).

19. H. Tanaka, M. Mushiage, Y. Ishida, "Single-longitudinal-mode selfaligned (AlGa)As double-heterostructure lasers fabricated by molecular beam epitaxy," Japanese Journal of Applied Physics 24(2), L89-L90 (1985).

20. K. Yagi, H. Yamauchi, and T. Niina, "High external differential quantum efficiency (80%) SCH lasers grown by MBE," IEEE International Semiconductor Laser Conference, Kanazawa, Japan, Conference Program and Abstract of Papers, 158-159 (1986).

21. G. A. Evans, N. W. Carlson, J. M. Hammer, M. Lurie, J. K. Butler, L. A. Carr, F. Z. Hawrylo, E. A. James, C. J. Kaiser, J. B. Kirk, W. F. Reichert, S. R. Chinn, J. R. Shealy, and P. S. Zory, "Efficient, high power (>150 mW) grating surface emitting lasers," Appl. Phys. Letters, March 28, 1988, accepted for publication.

22. N. W. Carlson, G. A. Evans, J. M. Hammer, M. Lurie, L. A. Carr, F. Z. Hawrylo, E. A. James, C. J. Kaiser, J. B. Kirk, W. F. Reichert, D. A. Truxal, J. R. Shealy, S. R. Chinn, and P. S. Zory, "A high power seven element grating surface emitting diode laser array with 0.012° far field angle," Appl. Phys. Letters, March 21,1988, accepted for publication; also N. W. Carlson, G. A.

Evans, J. M. Hammer, M. Lurie, J. K. Butler, S. L. Palfrey, M. Ettenberg, L. A. Carr, F. Z. Hawrylo, E. A. James, C. J. Kaiser, J. B. Kirk, W. F. Reichert, J. R. Shealy, J. W. Sprague, S. R. Chinn, and P. S. Zory, "Dynamically stable 0° phase mode operation of a grating surface emitting diode laser array," Optics Letters, April 1988; accepted for publication.

23. J. Hammer, "Monolithic two-dimensional surface-emitting diode laser arrays," Conference on Lasers and Electro-Optics, Baltimore, Technical Digest, 134 (1987).

24. G. A. Evans, J. M. Hammer, N. W. Carlson, F. R. Elia, E. A. James, and J. B. Kirk, "Surface-emitting second order distributed Bragg reflector laser with dynamic wavelength stabilization and far-field angle of 0.25°," Appl. Phys. Lett.49(6), 314-315 (1986).

25. J. K. Butler and D. Botez, "Mode characteristics of nonplanar double-heterojunction and large-optical-cavity laser structures," IEEE Journal of Quantum Electron QE-18(6), 952-961 (1982).

25. J. K. Butler and D. Botez, "Mode characteristics of nonplanar double-heterojunction and large-optical-cavity laser structures," IEEE Journal of Quantum Electron. QE-18(6), 952-961 (1982).

26. A. Sommerfeld, Partial Differential Equations in Physics, p. 195, Academic Press, New York (1949).

27. L. Lewin, "Obliquity-factor correction to solid-state radiation patterns," Journal of Applied Physics, 46(5) 2323-2324 (1975).

28. H. C. Casey, Jr., D. D. Sell, and K. W. Wecht, "Concentration dependence of the absorption coefficient for n- and p-type GaAs between 1.3 and 1.6 eV," J. Appl. Phys. 46(1), 250-257 (1975).

29. T. Tamir and F. Y. Kou, "Varieties of leaky waves and their excitation along multilayered structures," IEEE Journal of Quantum Electronics QE-22(4), 544-551(1986).

30. J. K. Butler, H. Kressel, and I. Ladany, "Internal optical losses in very thin CW heterojunction laser fiodes," IEEE Journal of Quantum Electronics QE-11(7), 402-408 (1975).

31. W. Streifer, Robert D. Burnham, and D. R. Scifres, "Substrate radiation losses in GaAs heterostructure lasers," IEEE Journal of Quantum Electronics QE-12(3), 177-182 (1976).

32. D. R. Scifres, W. Streifer, and R. D. Burnham, "Leaky wave room-temperature double heterostructure GaAs:GaAlAs diode laser," Appl. Phys. Lett. 29(1) 23-25 (1976).

33. J. Manning and R. Olshansky, "The carrier-induced index change in AlGaAs and 1.3 μm InGaAs diode lasers," IEEE J. Quan. Electron QE-19(10), 1525-1530 (1983).

34. V. Asder, J. Christiansen, and R. D. Russel, "COLSYS - a collocation code for boundary value problems," Codes for Boundary Value Problems, B. Childs et. al. Eds., Lecture Notes in Computer Science, 76, New York: Springer-Verlag (1979).

35. R. Papannareddy, W. E. Ferguson, Jr., and J. K. Butler, "Four models of lateral current spreading in double-heterostructure stripe-geometry lasers," IEEE J. Quan. Electron. QE-24(10), 60-65 (1988).

36. J. K. Butler and G. A. Evans, "Self-consistent analysis of gain saturation in channeled-substrate-planar double-heterojunction lasers," Appl. Phys. Lett. 51(22), 1792-1794 (1987).

37. F. Stern, "Calculated spectral dependence of gain in excited GaAs," J. Appl. Phys. 47, 5382-5386 (1976).

38. N. W. Carlson, V. J. Masin, G. A. Evans, B. Goldstein, and J. K. Butler, "Phase front measurements of high-power diode lasers," paper TuQ6, Digest of Technical Papers, Conference on Lasers and Electro-Optics, San Francisco, CA, (1986).

39. R. D. Burnham, D. R. Scifres, and W. Streifer, "Single heterostructure distributed feedback GaAs diode lasers," IEEE J. Quantum Electron. QE-11, 439 (1975).

40. Zh. I. Alferov, V. M. Andreyev, S. A. Gurevich, R. F. Kazarinov, V. R. Larionov, M. N. Mizerov, and E. L. Portnoy, "Semiconductor lasers with the light output through the diffraction grating on the surface of the waveguide layer," IEEE J. Quantum Electron. QE-11, 449 (1975).

41. P. Zory and L. D. Comerford, "Grating-coupled double-heterostructure AlGaAs diode lasers," IEEE J. Quantum Electron. QE-11, 451 (1975).

42. F. K. Reinhart, R. A. Logan, and C. V. Shank, "GaAs-Al$_{1-x}$Ga$_x$As injection lasers with distributed Bragg reflectors," Appl. Phys. Lett. 27, 45 (1975).

43. W. Ng and A. Yariv, "Highly collimated broadside emission from room temperature GaAs distributed Bragg reflector lasers," Appl. Phys. Lett. 31, 613 (1977).

44. B. Goldstein, N. W. Carlson, G. A. Evans, N. A. Dinkel, and V. J. Masin, "Performance of a channeled-substrate-planar high-power phase-locked array operating in the diffraction limit," Electronics Letters 23(21), 1136-1137 (1987).

45. N. W. Carlson, V. J. Masin, M. Lurie, B. Goldstein, and G. A. Evans, "Measurement of the coherence of a single-mode phase-locked diode laser array,", Appl. Phys. Lett. 51(9), 643-645 (1987).

65

Lateral Optical Confinement of Channeled-Substrate-Planar Lasers with GaAs/AlGaAs Substrates

Gary A. Evans

Jerome K. Butler

Valerie J. Masin

PRECEDING PAGE BLANK NOT FILMED

Lateral Optical Confinement of Channeled-Substrate-Planar Lasers with GaAs/AlGaAs Substrates

GARY A. EVANS, SENIOR MEMBER, IEEE, JEROME K. BUTLER, SENIOR MEMBER, IEEE, AND VALERIE J. MASIN

Abstract—A physical explanation is presented of the lateral guiding mechanism in channeled-substrate-planar (CSP) lasers based on the amount of wavefront tilt of the transverse field outside the channel region. Because of this inherent wavefront tilt, all CSP lasers will have a very slight asymmetry in their tranverse far-field pattern. The nature of the guiding mechanism does not require light absorption by the substrate. Design curves showing the complex lateral effective index step as a function of n-clad thickness with the active layer as a parameter are also presented. Depending on the specific layer compositions and thicknesses, the CSP guiding mechanism can provide a positive lateral index step for substrates with mole fractions of AlAs ranging from 0 to higher than 0.2.

I. INTRODUCTION

CHANNELED-substrate-planar (CSP) AlGaAs/GaAs semiconductor lasers are important commercial products and have been extensively studied both experimentally and theoretically [1]–[12]. CSP lasers have single spatial mode output powers as high as any single element semiconductor laser [4], [5] and have demonstrated long life at very high power [6]. They have been used as the elements in linear [13], [14] and Y-guide [15], [16] arrays. Originally grown by liquid phase epitaxy (LPE) on n-type [1] and later p-type [2] GaAs substrates, functionally equivalent structures are also grown by metalorganic chemical vapor deposition (MOCVD) [17], [18] and molecular beam epitaxy (MBE) [19], [20]. Although GaAs substrates with GaAs buffer layers have been predominantly used for CSP lasers, AlGaAs buffer layers have also been used [14], [21]. The purposes of this paper are to: 1) analyze the "cold cavity" modal characteristics of conventional CSP lasers which have GaAs and AlGaAs substrates, and 2) present a physical explanation of the CSP guiding mechanism. Current spreading and spatial hole burning in CSP lasers with GaAs substrates have been treated previously [10], [12] and those analyses are directly applicable to the structures discussed in this paper.

The waveguiding mechanisms of this extensively researched and highly developed laser structure [Fig. 1(a)]
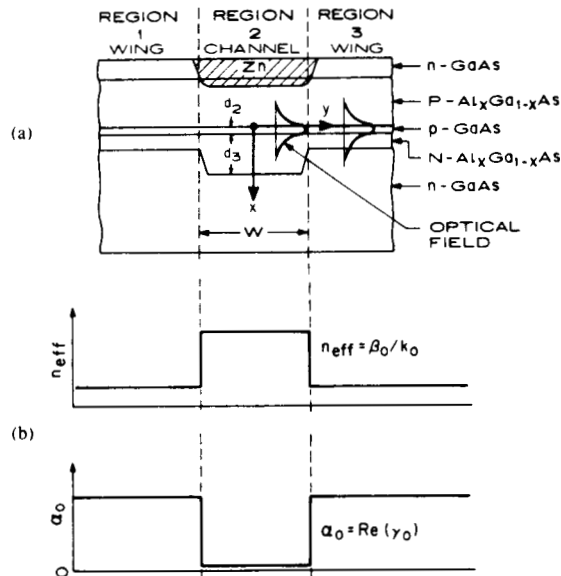
Fig. 1. (a) Geometry of a CSP laser, (b) real part of the lateral effective index profile, and (c) imaginary part of the lateral effective index profile.

have been qualitatively explained in physical terms [9], and theoretical analyses [7]–[12] agree that lateral mode confinement results from the combination of a positive real index guide [Fig. 1(b)] parallel to the junction, with high losses (related to a large imaginary component of the effective index) in the region outside the channel [Fig. 1(c)]. This resulting complex effective index provides mode confinement parallel to the junction.

Growth of CSP lasers on AlGaAs substrates or AlGaAs buffer layers is of interest to prevent meltback of the channel profile during the growth of both single devices and arrays [14], to prevent meltback of a grating incorporated in the structure that provides distributed feedback (DFB) [21], and to provide a transparent window for "junction-down" mounting of grating surface emitting lasers [22]. In addition, the AlGaAs buffer layer may be a more effective current blocking layer than a conventional GaAs blocking layer [2], [17] and AlGaAs substrates may reduce local heating. The modification of a CSP laser by inserting an AlGaAs layer between the cladding layer and the GaAs substrate of a CSP laser has been suggested as

PRECEDING PAGE BLANK NOT FILMED

a possible approach to reduce heating and to increase efficiency [23]. In this proposed structure, lateral radiation (because a negative index step lateral waveguide [24]–[27] is formed) would be substituted for the transverse substrate radiation of a CSP laser.

In this paper, we show that CSP lasers emitting at wavelengths in the vicinity of 0.7–0.9 μm have a real positive index step even if the substrate has a mole fraction of AlAs approaching 0.3. Previously, a high absorption loss in the substrate was considered necessary for lateral guiding in CSP structures [9]. A common belief has been that CSP lasers would not be index guided at long wavelengths (> ~8600 Å) because of the reduced absorption of the lasing light by the GaAs substrate. (Depending on the dopant concentration of the substrate, the substrate absorption is reduced from about 5000 cm^{-1} at 8300 Å to about 500 cm^{-1} or less at 8700 Å [28].) The explanation of the guiding mechanism presented in this paper is consistent with the experimental operation of index guided CSP lasers at 8700 Å [29].

II. The Effective Index Method

The analysis of the near- and far-fields of lasers can be accomplished using the effective index method as discussed extensively in the literature [27]. The analysis of the lateral modes (along the y direction) uses the effective index obtained from calculations of the transverse modal field. We assume the fields are written as

$$E_y = E_0 u(x, y) \, v(y) \exp(j\omega t - \gamma z) \quad (1)$$

where $\gamma = \alpha + j\beta$ is the complex modal propagation constant. The quantity $u(x, y)$ is the transverse field function and is a solution of the wave equation

$$\partial^2 u / \partial x^2 + [\gamma_0(y)^2 - k_0^2 \kappa(x, y)] u = 0 \quad (2)$$

where $\kappa(x, y)$ is the layer-dependent complex relative electric permittivity, $\gamma_0(y) = \alpha_0(y) + j\beta_0(y)$ is the transverse complex propagation constant, and k_0 is the free-space wavenumber. Assuming the top p-clad layer > 1.0 μm in thickness, the transverse modes can be determined from a solution of the four-layer waveguide shown in Fig. 2. The secular equation for the modes in the four-layer waveguide is

$$[(r^2 - q^2) \tan rd_2 - 2qr](p + q) \exp(qd_3)$$
$$+ [(r^2 + q^2) \tan rd_2](p - q) \exp(-qd_3) = 0$$
$$(3)$$

where

$$r^2 = [\gamma_0^2 + k_0^2 \kappa_2] \quad (4a)$$

$$q^2 = -[\gamma_0^2 + k_0^2 \kappa_i], \quad i = 1, 3 \quad (4b)$$

$$p^2 = -[\gamma_0^2 + k_0^2 \kappa_4]. \quad (4c)$$

We have assumed for proper modes, i.e., modes that decay exponentially as $|x| \to \infty$, that Re $\{p\}$ and Re $\{q\}$ > 0. Generally, the solutions are complex with complex
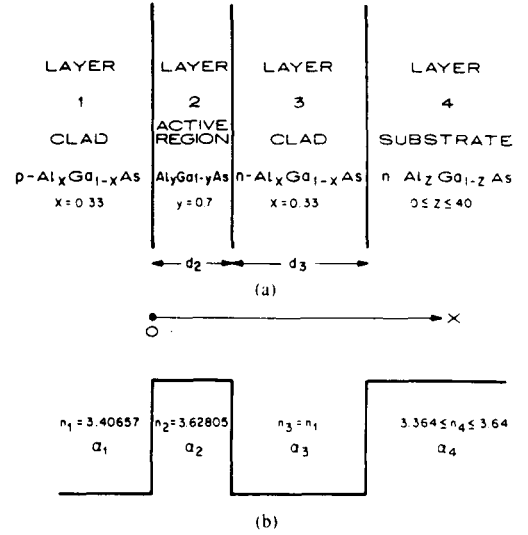

Fig. 2. The four-layer waveguide structure with (a) the layer geometry and (b) the refractive index profile.

eigenvalues [30] and the fields in the substrate are damped sinusoid functions as shown in Fig. 3. The solutions for the transverse field functions $u(x, y)$ are obtained in both the channel region ($|y| < W/2$) and the wing region ($|y| > W/2$) by matching the fields and their derivatives at the three interfaces located at $x = 0$, d_2, and d_3; W is the channel width. The lateral field functions $v(y)$ are computed after the complex effective index profile $n_{eff}(y)$ = $-j\gamma_0(y)/k_0$ is determined. In the analysis of the transverse mode functions, we assume the absorption losses in the p-cladding, active layer, and n-cladding layers have values $\alpha_1 = 10$ cm^{-1}, $\alpha_2 = 200$ cm^{-1}, and $\alpha_3 = 10$ cm^{-1}. (The actual value of loss (or gain) in the active layer has an insignificant effect on the value of the complex effective index. However, the lateral distribution of the gain in the active layer above threshold is very important in determining the optoelectronic characteristics of the device [10], [12].) The Al content of the active layer is ~7 percent in order to give a lasing wavelength $\lambda_0 = 0.83$ μm. The Al content of the cladding layers is 33 percent, while the Al content of the substrate (normally 0 percent for CSP lasers) is varied from 0 to 40 percent. This variation allows for a study of the coupling of light from the lasing region to the substrate. Because the mole fraction of AlAs in the substrate is variable, the value of the substrate absorption coefficient (at $\lambda = 0.83$ μm) ranges from about 10 000 cm^{-1} (p-type GaAs substrate) or 5000 cm^{-1} (n-type GaAs substrate) [28] down to 10 cm^{-1} as the mole fraction of AlAs in the substrate increases beyond 0.10. A material absorption value of 10 cm^{-1} is nominally assigned to the cladding layers and the AlAs containing substrates to account for free-carrier losses.

The far-field intensity pattern is found from the two-dimensional Fourier transform of the aperture field distribution and the obliquity factor $g(\theta)$ [31]. The two-di-
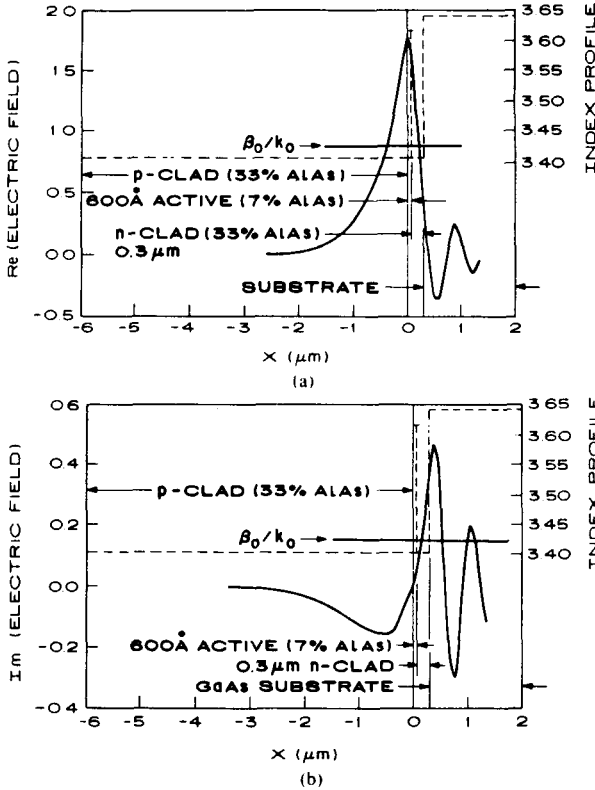
Fig. 3. The (a) real and (b) imaginary part of the electric field distribution for the transverse profile shown in Fig. 2 with $d_2 = 600$ Å, $d_1 = 0.3$ μm, and $\alpha_s = 5000$ cm^{-1}

mensional Fourier transform of the aperture field at the laser facet lying in the $z = 0$ plane is

$$F(k_x, k_y) = E_0 \int_{-\infty}^{\infty} \int_{-\infty}^{\infty} u(x, y) \, v(y)$$
$$\cdot \exp\left[jk_x x + k_y y \right] dx \, dy \qquad (5)$$

where $k_x = k_0 \cos \phi \sin \theta$ and $k_y = k_0 \sin \phi \sin \theta$ and r, θ, and ϕ are the observation point coordinates in the far field defined by $z = r \cos \theta$, $x = r \sin \theta \cos \phi$, and $y = r \sin \theta \sin \phi$. The transverse radiation pattern is obtained by placing $\phi = 0$ and varying θ. The lateral pattern is obtained by placing $\phi = \pi/2$ and varying θ.

Since we are focusing our attention on the transverse patterns, we place $\phi = 0$ so that

$$F(k_x, 0) = \int_{-\infty}^{\infty} \int_{-\infty}^{\infty} u(x, y) \, v(y)$$
$$\cdot \exp\left[jk_x x + k_y y \right] dx \, dy \qquad (6)$$

represents an "averaged transform" of the transverse field function $u(x, y)$ where $v(y)$ is the weighting term. In the special case of a square channel CSP, the function $u(x, y)$ can be written

$$u(x, y) = \begin{cases} u_{ch}(x), & |y| \leq W/2 \\ u_w(x), & |y| > W/2. \end{cases} \qquad (7)$$

For this case. (6) reduces to

$$F(k_x, 0) = F_{ch}(\theta) \, \zeta_{ch} + F_w(\theta) \, \zeta_w \qquad (8)$$

where

$$F_i(\theta) = \int_{-\infty}^{\infty} u_i(x) \exp\left[jk_x x \right] dx, \quad i = \text{channel, wing} \qquad (9)$$

and

$$\zeta_{ch} = \int_{-W/2}^{W/2} v(y) \, dy \Big/ \int_{-\infty}^{\infty} v(y) \, dy \qquad (10a)$$

$$\zeta_w = 2 \int_{W/2}^{\infty} v(y) \, dy \Big/ \int_{-\infty}^{\infty} v(y) \, dy. \qquad (10b)$$

Thus, the transverse far-field radiation pattern perpendicular to the junction $I_\perp(\theta) = |g(\theta)|^2 F(k_x, 0) F^*(k_x, 0)$ for the square channel CSP laser can be written as

$$I_\perp(\theta) = I_{ch}(\theta) \left| \zeta_{ch} \right|^2 + I_w(\theta) \left| \zeta_w \right|^2$$
$$+ 2 |g(\theta)|^2 \, Re\left[F_{ch}(\theta) \, F_w(\theta) \, \zeta_{ch} \zeta_w \right] \qquad (11)$$

where $I_{ch}(\theta) = |g(\theta)|^2 F_{ch}(\theta) \, F_{ch}^*(\theta)$ and $I_w(\theta) = |g(\theta)|^2 F_w(\theta) \, F_w^*(\theta)$. ζ_{ch}, the fraction of the lateral field confined to the channel, is generally large. For the conventional CSP laser described in Table I, $|\zeta_{ch}|^2$ ranges from 0.97 to 0.99 for channel widths of 4–6 μm. Therefore, the transverse far-field pattern of the laser will be almost totally shaped by the Fourier transform field in the channel region.

III. LATERAL OPTICAL CONFINEMENT

Waveguiding in CSP lasers appears paradoxical at first glance: Based on intuition for bound modes in dielectric waveguides, one expects that the CSP geometry has a larger effective index (real part) in the region outside the channel since a significant portion of the perpendicular field distribution there "averages in" the high index of the GaAs substrate. In addition, one expects that the large imaginary component of the effective index outside the channel region is due to high absorption (because $\alpha_4 = 5000 - 10\,000$ cm^{-1} at a lasing wavelength of 0.83 μm [28]) in the GaAs substrate. However, analysis of the CSP structure shows that: 1) the effective index (real part) is higher inside the channel than outside (producing a positive index step and corresponding bound lateral modes), and 2) the mode loss outside the channel region *increases* as the substrate absorption is *decreased*.

The reason for these apparent contradictions is that the transverse field in the regions outside the channel is not a conventional bound mode, but a complex field which radiates some power into the substrate. The conventional bound mode of a passive dielectric waveguide has decaying exponential field solutions in the first and last (the semi-infinite) layers. A leaky mode [32] has sinusoidal solutions with exponential growth in one or both of the outermost layers. When the outermost layers of an otherwise leaky waveguide have sufficient loss, the field so-

	CSP	CSPNL	CSPNIC
d_2	600 Å	600 Å	600 Å
α_4	10 000 cm⁻¹(5000 cm⁻¹)	0 cm⁻¹	10 000 cm⁻¹(5000 cm⁻¹)
Δn	6.59 × 10⁻³(6.82 × 10⁻³)	7.14 × 10⁻³	2.55 × 10⁻³(1.25 × 10⁻³)
$\Delta\alpha/k_0$	4.75 × 10⁻³(5.07 × 10⁻³)	5.37 × 10⁻³	2.57 × 10⁻³(2.08 × 10⁻³)
$(\beta/k_0)_{ch}$	3.42315 (3.42315)	3.42315	3.42315 (3.42315)
$(\beta/k_0)_w$	3.41656 (3.41633)	3.41601	3.42061 (3.42190)
FWHP of $I_{ch}(\theta)$	25.18° (25.17°)	25.21°	24.88° (24.73°)
FWHP of $I_w(\theta)$	32.12° (32.21°)	32.40°	30.14° (28.17°)

lution is proper (referred to here as a "bound leaky mode") because the fields exponentially decay, albeit the decay is due to the absorption. Conventional bound modes have normalized transverse propagation constants β_0/k_0 that are greater than the refractive indexes of the outermost layers. The complex transverse fields ("bound leaky modes") outside the channel have normalized propagation constants less than the refractive index of one (or both) outermost layers.

In Fig. 3, the index of refraction profile of the layers outside the channel region is shown superimposed on a plot of the real (a) and imaginary (b) parts of the electric field for the fundamental mode. The magnitude (3.4163) of the normalized longitudinal propagation constant β_0/k_0 (at $y > W/2$) for the fundamental mode, also shown in Fig. 3, corresponds to sinusoidal solutions in both the active layer and the substrate. The oscillatory behavior of the fields for $x > 0.36$ is characteristic of a complex field which radiates some power into the substrate. Even in the channel region, the mode perpendicular to the junction is also, strictly speaking, a complex field, but the electric field is so isolated from the substrate by the thick n-clad region that the amplitude of the field oscillations in the substrate are negligible (see [11, Fig. 3]).

Fig. 4 shows the near-field intensities (a) and near-field phases (b) for the fields perpendicular to the junction in both the regions inside and outside the channel for a CSP structure with $d_2 = 600$ Å and $\alpha_4 = 10\,000$ cm⁻¹. Note that the wavefront is tilted at 1.0° for $-1.5 < x < 0.0$ μm and is tilted at about 20.2° for $x > 0.3$ μm for the mode in the regions outside the channel. Since the direction of wave propagation is perpendicular to the wavefront, the wave outside the channel is therefore tilted away from the z axis of the waveguide and is radiating some energy into the substrate. As the wavefront tilt increases, the guide wavelength λ_z increases (see Fig. 5). Correspondingly, the propagation constant ($\beta = 2\pi/\lambda_z$) and the effective index ($n_{eff} = \beta/k_0$) decrease.

If we assume that the wavelength in the direction of propagation (λp) does not change for the fundamental field distribution perpendicular to the junction whether it is inside or outside the channel, we can calculate the average tilt angle of the field distribution from (see Fig. 5)

$$\theta = \cos^{-1}[\lambda_p/\lambda_z]$$

$$= \cos^{-1}[\beta_0(y > W)/2/\beta_0(y = 0). \quad (12)$$
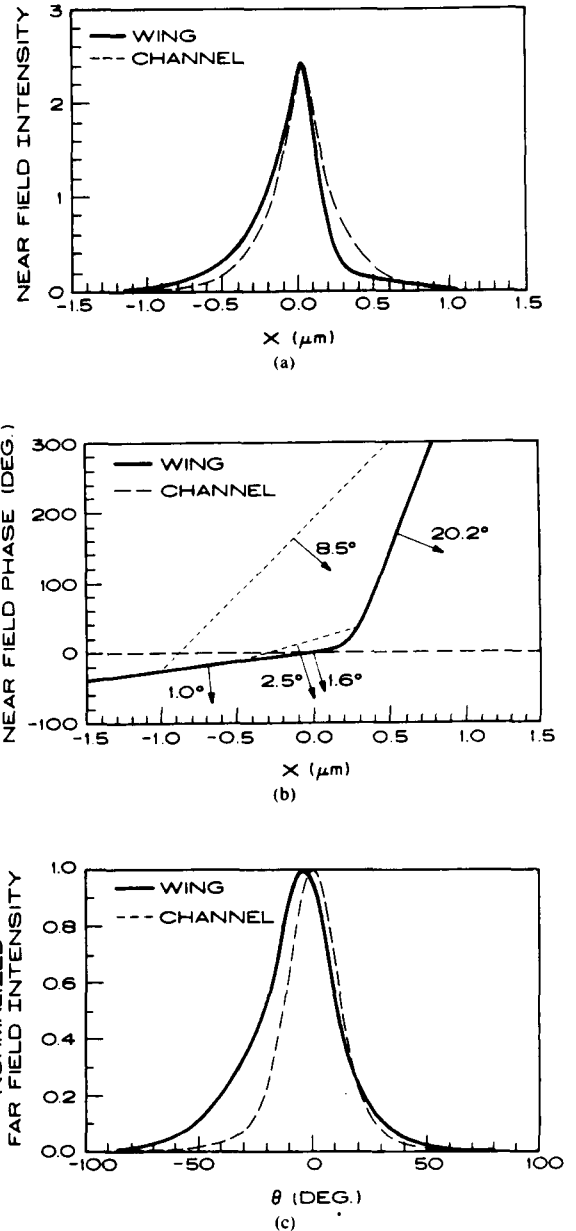

(a)

(b)

(c)

Fig. 4. The transverse (a) near-field intensity, (b) near-field phase, and (c) far-field intensity $I_{ch}(\theta)$ and $I_w(\theta)$ for a conventional CSP laser with an active layer thickness of 600 Å in the region inside (————) and outside (- - - -) the channel.
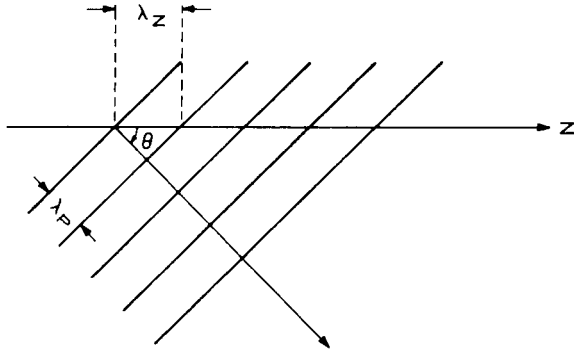
Fig. 5. Relationship of the guide wavelength λ to the waveguide in the direction of propagation λ_p for a wave propagating at an angle θ with respect to the guide axis.

For a structure with $d_2 = 600$ Å and $\alpha_4 = 10\,000\ cm^{-1}$, β_0/k_0 (at $y = 0$) $= 3.42315$ and β_0/k_0 (at $y > W/2$) $= 3.41656$ which results in a tilt angle of $3.6°$ using (12).

From curves such as Fig. 4(b), a plane wave equivalent tilt Θ can be calculated between any two points x_1 and x_2 with corresponding phases (in degrees) $\Phi(x_1)$ and $\Phi(x_2)$ from

$$\Theta = \tan^{-1} \frac{[\Phi(x_1) - \Phi(x_2)]\lambda_0}{360\, n_{eff}[x_1 - x_2]}. \qquad (13)$$

Indicated in Fig. 4(b) are plane wave equivalent tilts between the region of nonzero intensity ($-1.0 < x < 1.0$) of $8.5°$, between the $1/e^2$ points in intensity of $2.5°$, and between the half power points of $1.6°$. Another indication of average tilt of the wavefront can be obtained from the calculated shift of the peak of the far-field intensity pattern (corresponding to the "wing" region, $|y| > W/2$) which is offset from $0°$ because of radiation into the substrate [11], [33]-[35]. For the mode perpendicular to the junction outside the channel region, the calculated shift in the far-field peak is $4.0°$ in air [Fig. 4(c)], and therefore about $1.2°$ in the structure.

As a further illustration of the guiding mechanism, three structures are considered in Table I. All three models have the same dimensions: a 600 Å active layer, 1.5 μm channel depth, and a 0.3 μm thick n-clad in the "wing" regions ($|y| > W/2$). The first model (CSP) is that of a real CSP with losses of $10\,000\ cm^{-1}$ ($5000\ cm^{-1}$) in the GaAs substrate. The second model (CSPNL) is the same as the first model, except that there are no losses in the GaAs substrate. The third model (CSPNIC) is the same as the first model except that the "substrate" has the same AlAs composition as the n-clad layer (no index change between the n-clad and the substrate). The last two models are not physical, but are pedagogically chosen to show the various effects of complex field distributions and substrate absorption on the complex effective index that provides lateral confinement in a CSP laser. The parameters listed in Table I are the real and imaginary parts of the lateral complex effective index step, and for both inside and outside the channel, the normalized longitudinal

propagation constant and full width half power (FWHP) of the transverse beam divergence. The lateral optical confinement is due to the difference Δn and $\Delta\alpha$ in the real and imaginary parts of the complex effective index (γ_0/k_0) between the channel and wing region.

The near-field intensities, phases, and far-field intensities in the channel region are nearly identical for all three cases. However, the near-field intensities in the wing region, plotted in Fig. 6(a) differ, primarily for $x > 0.36$ where the bound mode (CSPNIC) is the strongest damped, the CSP leaky mode is moderately damped, and the CSPNL leaky mode is undamped. The near-field phases in the wing region are plotted in Fig. 6(b). They are similar for the CSP and CSPNL cases, with the CSPNL case having slightly more tilt for $x > 0.36$. The near-field phase of the CSPNIC has considerably less tilt than the other cases. The far-field intensities corresponding to the near-field in the wing region are shown in Fig. 6(c). The far-field peaks are all shifted from $0°$ to about $4°$. Because the far-field pattern in the transverse direction obtained from either (6) or (11) is due to the field in the channel and wing regions, the asymmetries in the far fields produced by the wing regions will always add a slight asymmetry to the far field produced by CSP lasers. Other causes of asymmetries in semiconductor far fields are thin cladding layers [33]-[35], material composition variations [11], and asymmetries in the device geometry [10], [12]. Although these far-field equations also hold for other laser geometries such as the ridge guide, the transverse fields inside and outside an ideal ridge structure both have symmetric transforms, and therefore ideal ridge (and most other) laser structures should have symmetric transverse far-field patterns.

Of the three models, the first two (CSP and CSPNL) give almost identical results, with the "no loss" model having a slightly larger complex effective index step. The third model does show that only high losses outside the channel region are sufficient to provide a lateral positive index step, in agreement with an earlier qualitative calculation [9]. The index step of the third model is less than half the complex effective index step of the other two models for a substrate loss of $10\,000\ cm^{-1}$. If the substrate absorption is $5000\ cm^{-1}$, the result is a positive index step of only 1.25×10^{-3} for the CSPNIC model, which is comparable to the amount of gain-induced index depression [36] expected at threshold.

These results are reasonable since from Fig. 6(a) the CSPNL structure has a larger fraction of the mode intensity in the substrate, has slightly more tilt in the near-field phase, and has slightly more off-axis tilt in the far-field than the CSP case. As the substrate absorption is decreased, more energy is radiated into the substrate, resulting in an increased average wavefront tilt, and therefore both the positive index step and the mode absorption (imaginary part of the effective index) in the region outside the channel increases. Another way to view the increasing mode loss with decreasing substrate absorption is that the "skin depth" of the "bound leaky mode" in-
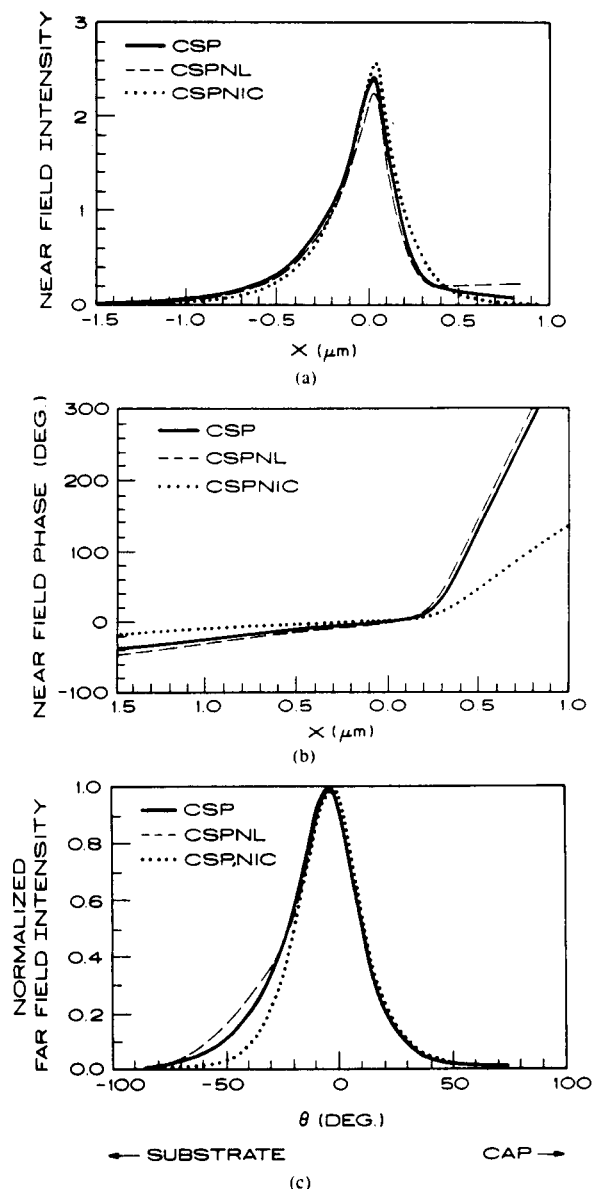
← SUBSTRATE   CAP →

(c)

Fig. 6. The transverse (a) near-field intensity, (b) near-field phase, and (c) far-field intensity in the region outside the channel region for a conventional CSP laser (———), a CSP laser with no absorption in the GaAs substrate (– – –), and a structure with the same index in the substrate as the channel region, but with high losses (10 000 c.n^{-1}) in the substrate (.....). All structures have an active layer thickness of 600 Å and d_3 = 0.3 μm.

creases as the substrate becomes less like a perfect conductor. Table I shows that the mode loss and lateral index step only increase by about 13 and 8 percent as the substrate absorption decreases from 10 000 cm^{-1} to 0. This increase, although slight, is unexpected from an earlier explanation [9] of CSP waveguiding which predicts that the magnitude of the complex lateral effective index step approaches zero as the substrate absorption decreases towards zero.

CSP Design Curves

Fig. 7(a) is a plot of the real part of the effective index for the mode perpendicular to the junction as a function of the n-clad thickness (d_3 in Fig. 2) for active layer thicknesses of 300, 400, 600, 800, and 1000 Å. For a CSP laser to have stable near- and far-field patterns with increasing drive current, the lateral index step should be large compared to index variations due to gain. The gain-induced index depression will typically reduce the index of refraction of the active layer by 10^{-2}, which in turn reduces the "cold cavity" effective index by about 10^{-3}. For this reason, a "cold cavity" lateral index step greater than 3 × 10^{-3} is desired to provide lateral mode stability. From Fig. 7, this is obtained for n-clad thicknesses (outside of the channel) of 0.3 μm or less for channel depths greater than 1.0 μm.

Fig. 7(b) is a plot of the imaginary part of the effective index, which increases with decreasing cladding thickness. The resulting magnitudes of the real and imaginary parts of the lateral effective index step for a CSP are always the same order of magnitude. Although a large imaginary component of the effective index is beneficial for stability of single laser diodes, it is detrimental to the operation of coherent CSP arrays in the fundamental array mode [37], [38].

Fig. 8 is a plot of the active layer confinement factor [11] as a function of the n-clad thickness ($d3$) for active layer thicknesses ($d2$) of 300, 400, 600, 800, and 1000 Å.

AlGaAs Substrates for CSP Lasers

The use of an AlGaAs substrate or a very thick AlGaAs buffer layer is often desirable: since AlGaAs has less meltback during LPE growth than GaAs, an AlGaAs layer may be preferred for fabricating gratings for distributed feedback CSP lasers [21]. The reduced meltback can also aid in maintaining the dimensions of the channel and the n-clad thickness. Due to a shorter diffusion length of minority carriers [39], [40], an AlGaAs buffer layer can be a more effective current blocking layer than the conventional GaAs blocking layer [2]. Some surface emission devices such as the CSP-LOC-DBR [22] can be made more efficient if the lasing light were extracted through a transparent substrate.

Plots of the real and imaginary parts of the effective index for a CSP laser with a 600 Å active layer and for substrate compositions of 0, 10, 20, 30, and 40 percent AlAs are shown in Fig. 9. The behavior of the curves for 10 and 20 percent AlAs have the same explanation as the effective index curves for CSP lasers on GaAs substrates: the real part of the lateral effective index is smaller outside the channel region than inside because of the wavefront tilt. Although this tilt is the dominant mechanism responsible for the smaller index outside the channel, there is less of an index step as the Al increases from 0 to 20 percent in the substrate. The reason for this is that the substrate confinement factor Γ_4 (a weighting factor in cal-
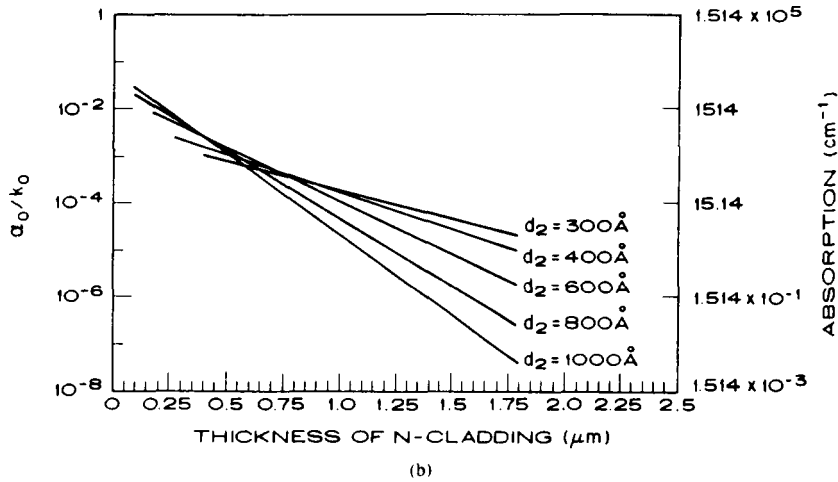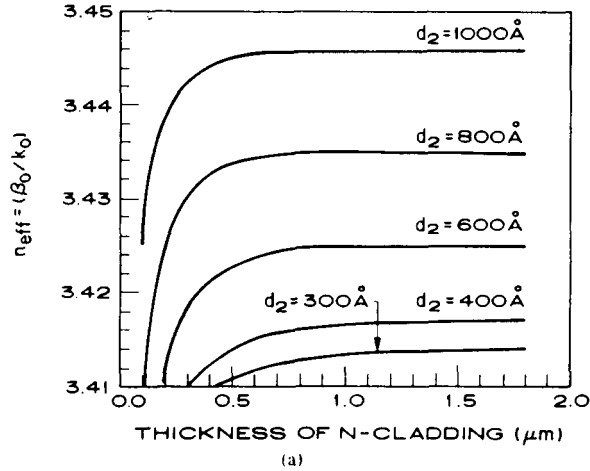
Fig. 7. The (a) real part of the effective index and (b) imaginary part of the effective index as a function of the n-clad thickness for active layer thicknesses of 300, 400, 600, 800, and 1000 Å for a conventional CSP laser.
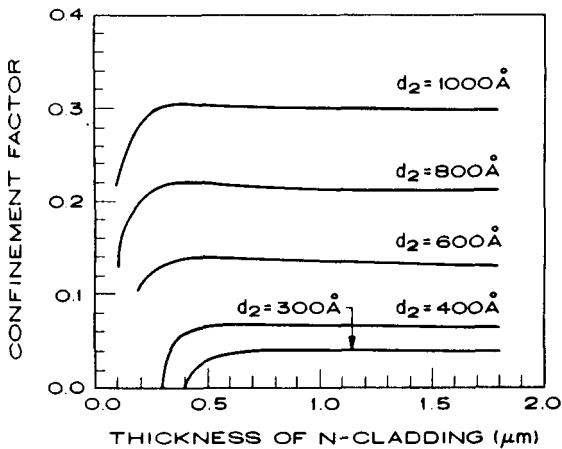

Fig. 8. The active layer confinement factor as a function of the n-clad thickness for active layer thicknesses of 300, 400, 600, 800, and 1000 Å for a conventional CSP laser.

culating the effective index) increases substantially which increases the effective index towards n_4. (The same behavior one expects for a conventional bound mode.)

For a fixed n-clad thickness, for example 0.3 μm, and for mole fractions of AlAs below about 30 percent, the mode losses increase with the mole fraction of AlAs in the substrate. This can be explained by increased coupling of the mode energy to the substrate (see Γ_4, the substrate confinement factor [11] in Table II) as the index of the substrate approaches the value of the normalized transverse mode propagation constant β_0/k_0. This increased coupling of energy to the substrate is also apparent in Fig. 10(a) which shows a reduced peak mode intensity with increased mode intensity in the substrate, in Fig. 10(b) which shows the near-field phase, and in Fig. 10(c) which shows an increasing tilt of the far-field patterns as the mole fraction of AlAs increases. Because of the increased field penetration (increased "skin depth") into the substrate
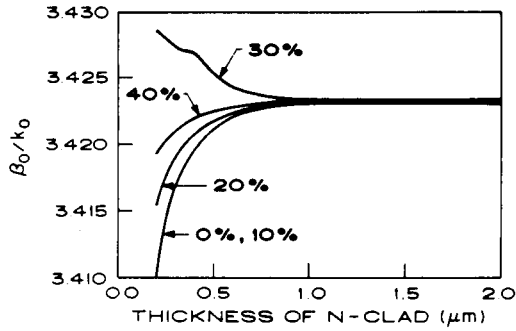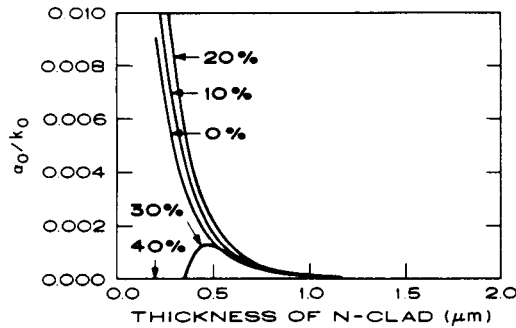
Fig. 9. The (a) real part of the effective index and (b) imaginary part of the effective index as a function of the n-clad thickness for an active layer thickness of 600 Å for CSP lasers with mole fractions of AlAs of 0, 10, 20, 30, and 40 percent.

TABLE II
CONFINEMENT FACTORS FOR CSP LASERS WITH 0, 10, AND 20 PERCENT AlAs SUBSTRATES (d_2 = 600 Å)

Γ_{layer}	0.0 AlAs (n_4 = 3.64)		0.1 AlAs (n_4 = 3.591)		0.2 AlAs (n_4 = 3.498)	
	Channel	Wing	Channel	Wing	Channel	Wing
Γ_1	0.431	0.558	0.431	0.476	0.431	0.290
Γ_2	0.139	0.138	0.139	0.120	0.139	0.083
Γ_3	0.431	0.248	0.430	0.223	0.430	0.184
Γ_4	1.6×10^{-5}	0.055	5.8×10^{-5}	0.182	1.8×10^{-4}	0.443

with increasing mole fraction of AlAs, the peak temperature due to local heating at the channel shoulders [41], [42] may be reduced by spreading the absorption of the optical field further into the substrate.
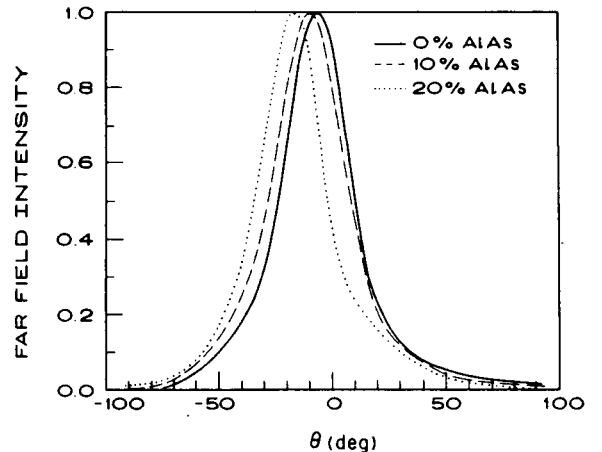
As the mole fraction of AlAs in the substrate approaches 30 percent, the index in the substrate becomes close to the value of the normalized transverse mode propagation constant β_0/k_0 in both regions. Table III lists the applicable parameters for a CSP laser with an AlAs mole fraction of 0.30 in the substrate. For this case, the effective index for the region outside the channel is greater than the index of the substrate, corresponding to a conventional bound field distribution. Inside the channel, the effective index is less than the index of the substrate, resulting in a complex transverse field distribution ("bound leaky mode") in the channel region, exactly opposite to
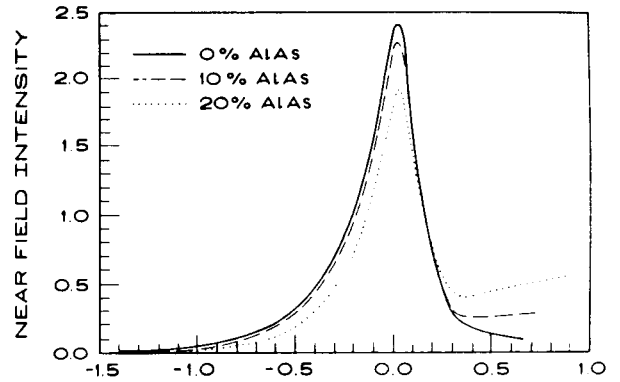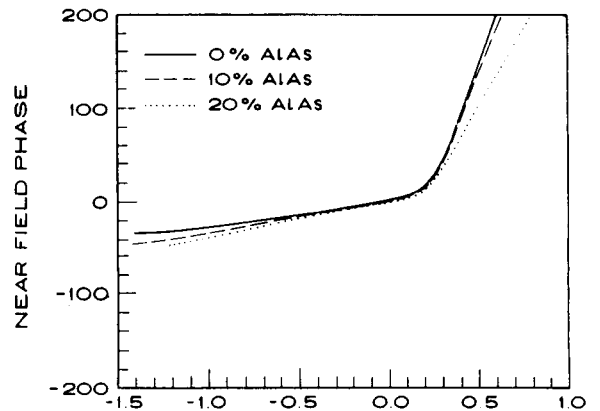
Fig. 10. The transverse (a) near-field intensity, (b) near-field phase, and (c) far-field intensity pattern $I_{\shortparallel}(\theta)$ in the region outside the channel region for CSP lasers with mole fractions of AlAs in the substrate of 0 (———), 10 (- - -), and 20 percent ($\cdots$). For all cases, d_1 = 0.3 μm.

a conventional CSP laser. Because the effective index of the (complex) transverse field distribution in the channel region is very close to the value of the index of the substrate, the mode energy couples strongly to the substrate.

TABLE III
CSP Laser with 30 Percent AlAs Substrate

Structure	Wing Parameters (Bound Mode)	Channel Parameters (Leaky Mode)
$d_2 = 600$ Å	$\beta/k_0 = 3.4273$	$\beta/k_0 = 3.4232$
$n_4 = 3.4270$	$\Gamma_1 = 0.16$	$\Gamma_1 = 0.43$
$\alpha_4 = 10$ cm^{-1}	$\Gamma_2 = 0.06$	$\Gamma_2 = 0.14$
$\Delta n = -4.17 \times 10^{-3}$	$\Gamma_3 = 0.18$	$\Gamma_3 = 0.43$
$\Delta\alpha/k_0 = 2.32 \times 10^{-6}$	$\Gamma_4 = 0.60$	$\Gamma_4 = 0.0036$

This strong coupling is analogous to impedance matching in a transmission line, and is similar to the effect of enhanced coupling of mode energy to the substrate by nonuniformities in the Al composition in the channel region of a CSP laser [11]. Although this strong coupling is not apparent in the near-field intensity [Fig. 11(a)], the near-field phase [Fig. 11(b)] shows a wavefront tilt of 2.8° for $x > 1.5$ μm. The substrate confinement factor in the channel region (Table III) for this case is one or two orders of magnitude larger than Γ_4 for the channel regions of any of the other cases considered (Tables II-IV). In addition, the far-field pattern [Fig. 11(c)] corresponding to the channel region is characteristic of strong coupling of mode energy to the substrate—the pattern is asymmetric and tilted 2.5° towards the substrate [11]. For the 30 percent case, Fig. 9(b) is an example of a resonant region (for n-clad thicknesses $0.4 < d_3 < 1.0$) in which the "average wavefront tilt" argument no longer properly predicts the index step. Again, the assumption that λ_p (Fig. 5) remains unchanged by the tilt is no longer the case. In fact, in this case, the change in λ_p more than offsets the slight wavefront tilt. λ_p decreases (the effective index increases) because n_4 is greater than n_3 and the substrate confinement factor is very large (increasing from 0.19 to 0.95 as d_3 decreases from 1.0 to 0.4). Fig. 12, which plots the active layer confinement factor for the cases shown in Fig. 9, shows a large decrease in the active layer confinement factor over the same range in d_3.

As the n-clad thickness decreases even further (below about 0.35 μm), the mode becomes a conventional bound mode and the effective index of the mode continues to increase because an increasing fraction of the mode energy is in the (slightly) higher index substrate. In Fig. 9(b), the losses for the 30 percent case increase as the n-clad thickness decreases, until the mode changes from a complex mode into a conventional bound mode and the losses approach zero (background).

Table IV lists the applicable parameters for a CSP laser which has 0.40 mole fraction of AlAs in the substrate. In this case, neither the transverse field inside the channel nor outside the channel are "bound leaky modes." The effective index curve decreases with decreasing n-clad thickness because the mode energy outside the channel is "averaging in" the lower clad index—just as in any ridge guide structure. The near- and far-fields for this case are shown in Fig. 13(a) and (b). Both inside and outside the
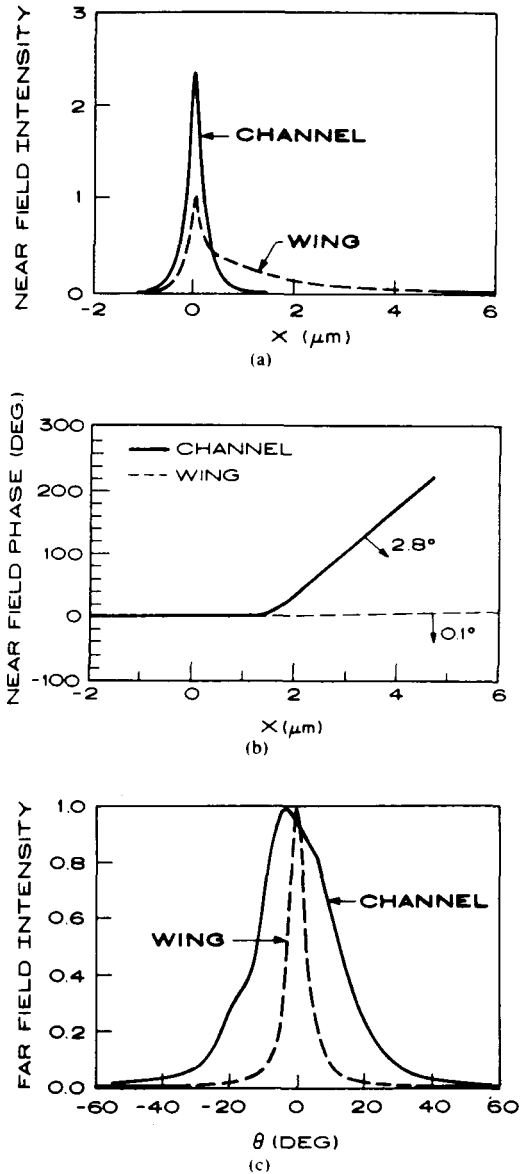
Fig. 11. The transverse (a) near-field intensity, (b) near-field phase, and (c) far-field intensity pattern for a CSP laser with a mole fraction of AlAs in the substrate of 30 percent. $d_3 = 0.3$ μm in the wing region.

channel, the modes are bound modes with flat phase fronts.

Performance Considerations

Although the large imaginary part of the effective index outside the channel region of a CSP laser helps stabilize the mode, it also increases the threshold current and decreases the differential quantum efficiency. Using the computational procedure described in [10], the power versus current curves for a CSP type laser, a ridge guide laser with cladding layer losses of 10 cm^{-1}, and a lossless ridge guide laser (all with active layer thicknesses of 600 Å) are calculated in Fig. 14. All three structures have the

Fig. 12. The active layer confinement factor as a function of the n-clad thickness for an active layer thickness of 600 Å for CSP lasers with mole fractions of AlAs of 0, 10, 20, 30, and 40 percent.

TABLE IV
CSP LASER WITH 40 PERCENT AlAs SUBSTRATE

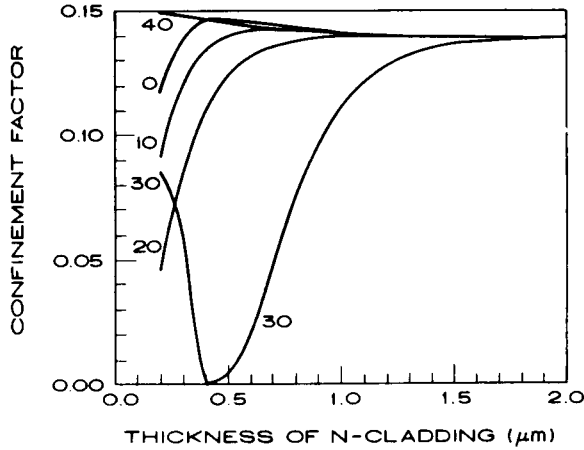| Structure	Wing Parameters (Bound Mode)	Channel Parameters (Bound Mode)
$d_2 = 600$ Å	$\beta/k_0 = 3.4209$	$\beta/k_0 = 3.4231$
$n_4 = 3.364$	$\Gamma_1 = 0.51$	$\Gamma_1 = 0.43$
$\alpha_4 = 10$ cm^{-1}	$\Gamma_2 = 0.15$	$\Gamma_2 = 0.14$
$\Delta n = 2.21 \times 10^{3}$	$\Gamma_3 = 0.32$	$\Gamma_3 = 0.43$
$\Delta\alpha/k_0 = 0.0$	$\Gamma_4 = 0.032$	$\Gamma_4 = 1.15 \times 10^{-5}$

Fig. 13. The transverse (a) near-field intensity and (b) far-field intensity pattern $I_h(\theta)$ and $I_w(\theta)$ for a CSP laser with a mole fraction of AlAs in the substrate of 40 percent in the region inside (———) and outside (– – –) the channel. $d_1 = 0.3$ μm in the wing region.

same lateral index step (6.822×10^{-3}) and profile (see inset of Fig. 14) with a channel or ridge width of 4 μm. The large differences in threshold current and differential quantum efficiency are due to the reduced losses outside the ridge of the two ridge structures compared to the high losses outside the channel of the CSP device.

The value of the injected current at which the first order lateral mode reaches threshold was also calculated for the three structures in Fig. 14. While the first-order mode of the ridge structures reached threshold at power levels in the 10–20 mW range, the first-order mode of the CSP structure was only approaching transparency at 200 mW. Since the channel and ridge widths are equal in these calculations, we must note that 4 μm is a relatively narrow channel for a CSP laser, while 4 μm is relatively wide for a ridge guide. As the CSP channel is widened from 8 to 12 μm, the power level at which the first higher order lateral mode reaches threshold is reduced from about 100 to 30 mW. As the width of the ridge is reduced to 2 μm, the first higher order lateral mode is calculated to reach threshold at about 50 mW. Such calculations indicate that the onset of higher order modes is not a significant effect in CSP lasers of common channel widths (less than 8 μm). Rather, variations and irregularities in the output characteristics of CSP lasers are more likely due to compositional variations [11] and geometrical asymmetries [10], [12].
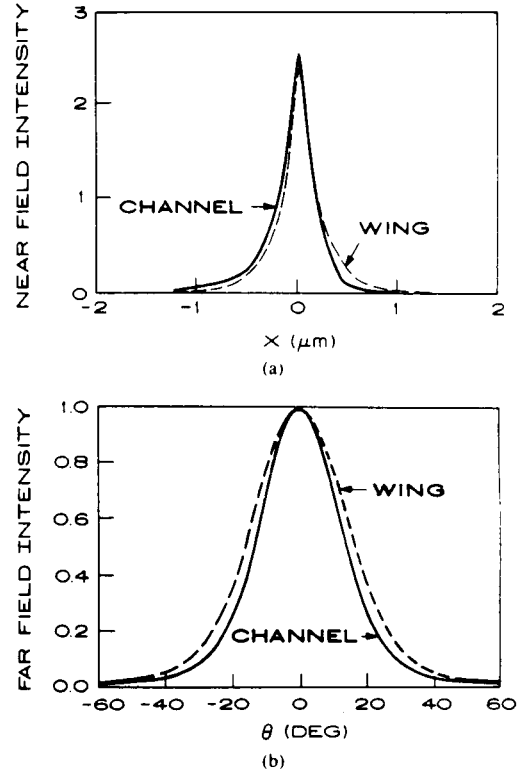
For the devices in Fig. 14, $\Delta\alpha_0/k_0 = 0$ for the ridge guide structures and 5.074×10^{-3} for the GaAs substrate CSP laser.

Analysis of Related Structures

In the Introduction, we mention two primary variations of the CSP structure. One contains an AlGaAs layer between the substrate and n-clad region which can serve to provide current blocking and/or prevent meltback during LPE growth over the channel. The other is grown by either MOCVD or MBE and is known by several names including self-aligned stripe (SAS) [17], [19], [20]. The conventional SAS structure contains a GaAs current blocking layer (with the same dopant polarity as the substrate) about 0.2–0.4 μm above the active layer. A segment of the blocking layer is removed and a second growth of material with the same composition as the cladding layer buries the GaAs blocking layers. The resulting structure is comparable to a CSP laser in that the opening in the blocking layer is equivalent to the channel width and the GaAs blocking layer is equivalent to the substrate. One feature of the SAS structure is that since the blocking layer is a finite thickness (typically 1 μm) compared to the infinitely thick (>50 μm) substrate, the calculated differential quantum efficiency is somewhat larger than for a conventional CSP. For 4 μm wide openings in the block-
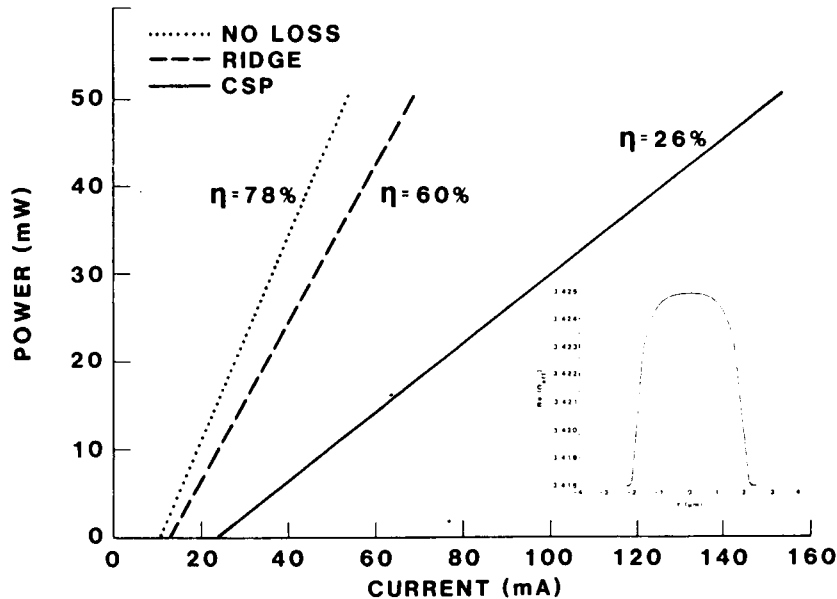
Fig. 14. Calculated power versus current curves for a conventional CSP laser (——), a conventional ridge guide laser (– – –), and a lossless ridge guide laser (· · ·). The inset shows the lateral effective index profile for all three structures.

ing layer or channel, the increase in differential quantum efficiency can be as much as 65 percent.

The calculations shown in this paper for CSP lasers suggest that AlGaAs layers can be used for anti-meltback and for current blocking in related structures such as the SAS or VSIS [2] device. However, for both of these related structures, the value of the effective index outside the channel region is very sensitive to laser wavelength, layer composition, and layer thickness. For some parameter values, the effective index can even oscillate [43] about the effective index of the channel region for small changes in a specific parameter (e.g., 1000–2000 Å in layer thickness). The sensitivity of the effective index for these structures is due to the various layers behaving as a dielectric stack which changes from high reflectivity to low reflectivity as the index or layer thickness is changed. A similar phenomenon has been observed in conventional CSP lasers which have a nonuniform AlAs composition in the channel regions [11]. Therefore, the use of AlGaAs layers to provide current blocking or to reduce meltback requires careful design and precise growth for these related structures.

CONCLUSIONS

We have presented a physical explanation of the guiding mechanism in CSP lasers: the lateral index step is determined by: 1) the amount of wavefront tilt, and 2) the magnitude of the wavelength in the direction of propagation λ_p. In most cases, the wavefront tilt is the dominate mechanism affecting the lateral index step and slight changes in the magnitude of λ_p explain minor changes in the real part of the lateral index step with changes in the AlAs composition ($0 < x < 0.3$) of the substrate. How-

ever, when the normalized transverse propagation constant is very close to the refractive index of the substrate (as in the example of a substrate with an AlAs composition equal to 0.3), a resonant condition occurs and the dominant mechanism governing the value of the effective index is the magnitude of λ_p. Therefore, CSP lasers are generally index guided even when there is no substrate absorption.

Because of the contribution of the tilted wavefront in the calculation of the far-field radiation pattern, all CSP lasers will have a slight asymmetry in their transverse far-field pattern.

Design curves which provide the complex lateral effective index step as a function of n-clad thickness with the active layer thickness as a parameter are presented. We also show that the CSP guiding mechanism provides a positive lateral real index step for substrates with mole fractions of AlAs ranging from 0 to values approaching 0.30.

REFERENCES

[1] K. Aiki, M. Nakamura, T. Kuroda, J. Umeda, R. Ito, N. Chinone, and M. Maeda, "Transverse mode stabilized $Al_xGa_{1-x}As$ injection lasers with channeled-substrate-planar structure," *IEEE J. Quantum Electron.*, vol. QE-14, pp. 89–94, Feb. 1978.
[2] S. Yamamoto, H. Hayashi, S. Yano, T. Sakurai, and T. Hijikata, "Visible GaAlAs V-channeled substrate inner stripe laser with sta-

bilized mode using p-GaAs substrate," *Appl. Phys. Lett.*, vol. 40, pp. 372–374, 1 Mar. 1982.

[3] S. Yamamoto, N. Miyauchi, S. Maei, T. Morimoto, O. Yamamoto, S. Yano, and T. Hijikata, "High output power characteristics in broad-channeled substrate inner stripe lasers," *Appl. Phys. Lett.*, vol. 46, pp. 319–321, Feb. 15, 1985.

[4] K. Hamada, M. Wada, H. Shimizu, M. Kume, F. Susa, T. Shibutani, N. Yoshikawa, K. Itoh, G. Kano, and I. Teramoto, "A 0.2W CW laser with buried twin-ridge substrate structure," *IEEE J. Quantum Electron.*, vol. QE-21, pp. 623–628, June 1985.

[5] B. Goldstein, M. Ettenberg, N. A. Dinkel, and J. K. Butler, "A high-power channeled-substrate-planar AlGaAs laser," *Appl. Phys. Lett.*, vol. 47, pp. 655–657, Oct. 1, 1985.

[6] T. Shibutani, M. Kume, K. Hamada, H. Shimizu, K. Itoh, G. Kano, and I. Teramoto, "A novel high-power laser structure with current-blocked regions near cavity facets," *IEEE J. Quantum Electron.*, vol. QE-23, pp. 760–764, June 1987.

[7] T. Kuroda, M. Nakamura, K. Aiki, and J. Umeda, "Channeled-substrate-planar structure $Al_xGa_{1-x}As$ lasers: An analytical waveguide study," *Appl. Opt.*, vol. 17, pp. 3264–3267, Oct. 15, 1978.

[8] K. A. Shore, "Above-threshold analysis of channelled-substrate-planar (CSP) laser," *Proc. IEE*, part I, pp. 9–15, Feb. 1981.

[9] S. Wang, C. Chen, A. S. Liao, and L. Figueroa, "Control of mode behavior in semiconductor lasers," *IEEE J. Quantum Electron.*, vol. QE-17, pp. 453–468, Apr. 1981.

[10] J. K. Butler, G. A. Evans, and B. Goldstein, "Analysis and performance of channeled-substrate-planar double-heterojunction lasers with geometrical asymmetries," *IEEE J. Quantum Electron.*, vol. QE-23, pp. 1890–1899, Nov. 1987.

[11] G. A. Evans, B. Goldstein, and J. K. Butler, "Observations and consequences of nonuniform aluminum concentrations in the channel regions of AlGaAs channeled-substrate-planar lasers," *IEEE J. Quantum Electron.*, vol. QE-23, pp. 1900–1908, Nov. 1987.

[12] T. Ohtoshi, K. Yamaguchi, C. Nagaoka, T. Uda, Y. Murayama, and N. Chinone, "A two dimensional device simulator of semiconductor lasers," *Solid-State Electron.*, vol. 30, no. 6, pp. 627–638, 1987.

[13] T. Kadowaki, T. Aoyagi, S. Hinata, K. Kaneno, Y. Seiwa, K. Ikeda, and W. Susaki, "Long-lived phase-locked laser arrays mounted on a Si-submount with Au-Si solder with a junction-down configuration," in *IEEE Int. Semiconductor Laser Conf., Conf. Program and Abstr. of Papers*, Kanazawa, Japan, Oct. 1986, pp. 84–85.

[14] B. Goldstein, N. W. Carlson, G. A. Evans, N. Dinkel, and V. J. Masin, "Performance of a channeled-substrate-planar high-power phase-locked array operating in the diffraction limit," *Electron. Lett.*, vol. 23, pp. 1136–1137, Oct. 8, 1987.

[15] M. Taneya, M. Matsumoto, S. Matsui, S. Yano, and T. Hijikata, "0° phase mode operation in phased-array laser diode with symmetrically branching waveguide," *Appl. Phys. Lett.*, vol. 47, pp. 341–343, Aug. 15, 1985.

[16] D. F. Welch, P. Cross, D. Scifres, W. Streifer, and R. D. Burnham, "In-phase emission from index-guided laser array up to 400 mW," *Electron. Lett.*, vol. 22, pp. 293–294, Mar. 13, 1986.

[17] K. Uomi, S. Nakatsuka, T. Ohtoshi, Y. Ono, N. Chinone, and T. Kajimura, "High-power operation of index-guided visible GaAs/GaAlAs multiquantum well lasers," *Appl. Phys. Lett.*, vol. 45, pp. 818–821, Oct. 15, 1984.

[18] J. J. Yang, C. S. Hong, J. Niesen, and L. Figueroa, "High-power single longitudinal mode operation of inverted channel substrate planar lasers," *J. Appl. Phys.*, vol. 58, pp. 4480–4482, Dec. 1985.

[19] H. Tanaka, M. Mushiage, and Y. Ishida, "Single-longitudinal-mode selfaligned (AlGa)As double-heterostructure lasers fabricated by molecular beam epitaxy," *Japan. J. Appl. Phys.*, vol. 24, pp. L89–L90, Feb. 1985.

[20] K. Yagi, H. Yamauchi, and T. Niina, "High external differential quantum efficiency (80%) SCH lasers grown by MBE," in *IEEE Int. Semiconductor Laser Conf., Conf. Program and Abstr. of Papers*, Kanazawa, Japan, Oct. 1986, pp. 158–159.

[21] B. Goldstein, G. Evans, J. Connolly, N. Dinkel, and J. Kirk, "An efficient AlGaAs distributed feedback channeled-substrate-planar laser," *Appl. Phys. Lett.*, to be published.

[22] G. A. Evans, J. M. Hammer, N. W. Carlson, F. R. Elia, E. A. James, and J. B. Kirk, "Surface-emitting second order distributed Bragg reflector laser with dynamic wavelength stabilization and far-field angle of 0.25°," *Appl. Phys. Lett.*, vol. 49, pp. 314–315, Aug. 11, 1986.

[23] S. Lee and L. Figueroa, "Modified channeled substrate planar (CSP) lasers with lateral leaky mode behavior," in *Proc. Topical Meet. Semiconductor Lasers*, Albuquerque, NM, Feb. 1987, pp. 128–131.

[24] T. Kajimura, K. Saito, N. Shige, and R. Ito, "Leaky-mode buried-heterostructure AlGaAs injection lasers," *Appl. Phys. Lett.*, vol. 30, pp. 590–591, June 1, 1977.

[25] R. W. H. Englemann, D. Kerps, and F. D. Nunes, "Lateral wave-guiding in stripe-geometry double-heterostructure lasers below the lasing threshold," *IEEE J. Quantum Electron.*, vol. QE-15, pp. 740–743, Aug. 1979.

[26] R. W. H. Englemann and D. Kerps, "Leaky modes in active three-layer slab waveguides," *Proc. IEE*, vol. 127, part I, pp. 330–336, Dec. 1980.

[27] J. K. Butler and D. Botez, "Mode characteristics of nonplanar double-heterojunction and large-optical-cavity laser structures," *IEEE J. Quantum Electron.*, vol. QE-18, pp. 952–961, June 1982.

[28] H. C. Casey, Jr., D. D. Sell, and K. W. Wecht, "Concentration dependence of the absorption coefficient for n- and p-type GaAs between 1.3 and 1.6 eV," *J. Appl. Phys.*, vol. 46, pp. 250–257, Jan. 1975.

[29] J. Connolly, T. R. Stewart, D. B. Gilbert, S. E. Slavin, D. B. Carlin, and M. Ettenberg, "High-power 0.87 μm channeled substrate planar lasers for spaceborn communications," in *SPIE Proc.*, vol. 885, Los Angeles, CA, Jan. 1988.

[30] A. Sommerfeld, *Partial Differential Equations in Physics.* New York: Academic, 1949, p. 195.

[31] L. Lewin, "Obliquity-factor correction to solid-state radiation patterns," *J. Appl. Phys.*, vol. 46, pp. 2323–2324, May 1975.

[32] T. Tamir and F. Y. Kou, "Varieties of leaky waves and their excitation along multilayered structures," *IEEE J. Quantum Electron.*, vol. QE-22, pp. 544–551, Apr. 1986.

[33] J. K. Butler, H. Kressel, and I. Ladany, "Internal optical losses in very thin CW heterojunction laser diodes," *IEEE J. Quantum Electron.*, vol. QE-11, pp. 402–408, July 1975.

[34] W. Streifer, R. D. Burnham, and D. R. Scifres, "Substrate radiation losses in GaAs heterostructure lasers," *IEEE J. Quantum Electron.*, vol. QE-12, pp. 177–182, Mar. 1976.

[35] D. R. Scifres, W. Streifer, and R. D. Burnham, "Leaky wave room-temperature double heterostructure GaAs:GaAlAs diode laser," *Appl. Phys. Lett.*, vol. 29, pp. 23–25, July 1976.

[36] J. Manning and R. Olshansky, "The carrier-induced index change in AlGaAs and 1.3 μm InGaAs diode lasers," *IEEE J. Quantum Electron.*, vol. QE-19, pp. 1525–1530, Oct. 1983.

[37] L. Figueroa, T. L. Holcomb, K. Burghard, D. Bullock, C. B. Morrison, L. M. Zinkiewicz, and G. A. Evans, "Modeling of the optical characteristics for twin-channel laser (TCL) structures," *IEEE J. Quantum Electron.*, vol. QE-22, pp. 2141–2149, Nov. 1986.

[38] N. W. Carlson, V. J. Masin, M. Lurie, B. Goldstein, and G. A. Evans, "Measurement of the coherence of a single-mode phase-locked diode laser array," *Appl. Phys. Lett.*, vol. 51, pp. 643–645, Aug. 31, 1987.

[39] H. Neumann and U. Flohrer, "Electron mobility in $Al_xGa_{1-x}As$," *Phys. Status Solidi (a)*, vol. 25, pp. K145–K147, Oct. 16, 1974.

[40] S. Adachi, "GaAs, AlAs, and $Al_xGa_{1-x}As$: Material parameters for use in research and device parameters," *J. Appl. Phys.*, vol. 58, pp. R1–R29, Aug. 1, 1985.

[41] S. Todoroki, M. Sawai, and K. Aiki, "Temperature distribution along the striped active region in high power GaAlAs visible lasers," *J. Appl. Phys.*, vol. 58, pp. 1124–1128, Aug. 1985.

[42] S. Todoroki, "Influence of local heating on current-optical output power characteristics in $Ga_{1-x}Al_xAs$ lasers," *J. Appl. Phys.*, vol. 60, pp. 61–65, July 1986.

[43] N. Carlson, private communication.

Gary A. Evans (S'69-M'75-SM'82) was born in Omak, WA, in 1948. He received the B.S.E.E. degree from the University of Washington, Seattle, in 1970, and the M.S.E.E. and Ph.D. degrees in electrical engineering and physics from the California Institute of Technology, Pasadena, in 1971 and 1975, respectively.

After post-doctoral work at Caltech, he worked for R&D Associates, Marina Del Rey, CA, on radar systems, CCD's, and integrated optics. While on leave of absence from RDA, he was a Visiting Professor at the University of Washington, teaching and doing research in solid-state physics and integrated optics for two academic years (1977–

1979). In 1979 he joined Aerospace Corporation's Electronic Research Laboratory, El Segundo, CA, and then TRW, Redondo Beach, CA, in 1981. In 1984 he joined the David Sarnoff Research Center (formerly RCA Laboratories, now a subsidiary of SRI International), Princeton, NJ. Since 1979 he has worked on the design, growth, and fabrication of conventional cleaved facet lasers, DBR lasers, and grating surface emitting lasers using both LPE and MOCVD technologies. He and his co-workers developed the first integrated two-cavity semiconductor laser, the first etched-mirror unstable resonator semiconductor laser, and the first coherent array of surface emitting lasers. He also has worked on reliability, power, and stability issues of semiconductor lasers for laser satellite communication systems. He has authored or coauthored more than 50 papers and a book chapter. His current research interests are the development of semiconductor lasers and laser arrays.

Dr. Evans is a past member of the IEEE National Task Force for Career Maintenance and Development and was Chairman of the Santa Monica Bay Section of the IEEE. He is a member of the American Physical Society, the Optical Society of America, Tau Beta Pi, and is a Registered Professional Engineer.

Valerie J. Masin was born in Glen Cove, NY, on November 24, 1956. She received the B.S. degree in electrical engineering from the University of Pennsylvania, Philadelphia, in 1983.

She joined RCA Laboratories' Optoelectronic Systems Research Group in 1983 studying the structures of high power AlGaAs lasers. In March 1987 she joined TASC (The Analytic Sciences Corporation), Reading, MA, as a member of the Technical Staff in the Surveillance and Space Technology Department. She is currently working on scene generation and sensor modeling.

High-Power 0.87μm Channel Substrate Planar Lasers for Spaceborne Communications

J.C. Connolly, T.R. Stewart, D.B. Gilbert,
S.E. Slavin, D.B. Carlin, and M. Ettenberg

David Sarnoff Research Center
CN-5300 Princeton, New Jersey 08543-5300

ABSTRACT

High-power single mode channeled-substrate-planar AlGaAs diode lasers are being developed for reliable, high-power operation for use as sources in spaceborne optical communications systems. Most work on AlGaAs semiconductor lasers has been focused on devices with an emission wavelengths less than 8400Å where both high power and reliable operation have been previously demonstrated. In spaceborne communication systems, the output wavelength is optimized at 8700Å to avoid absorption of the emitted light by the atmosphere when communicating with ground-based terminals. The CSP laser structure has been optimized for operation at an emission wavelength of 8700Å. Such devices have exhibited output powers in excess of 80 mW cw at an operating temperature of 80°C. Single spatial mode and substantially single longitudinal mode operation has been obtained at output powers greater than 50 mW cw and 100 mW (50% duty-cycle). The phase-front of the high-power devices has been examined and has shown rms aberrations to be $\cong \lambda/50$. Lifetesting of these devices at 50mW (50% duty-cycle) has shown reliable operation in excess of 5,000 hrs.
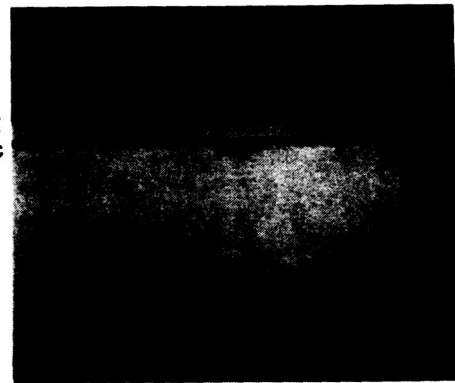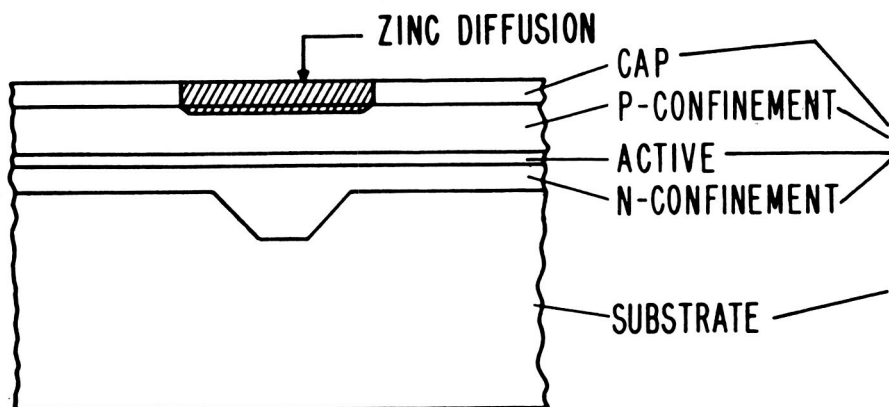
1. INTRODUCTION

The rapid development of high-power single mode AlGaAs lasers was initially sparked by their potential use in optical recording and printing systems[1,2,3]. Recently, their potential as light sources for free space communications applications has been recognized. Some of the benefits gained by the use of diode lasers include their compact size, high power conversion efficiency, and reliability. In addition, the mass of the spaceborne optical communication system is greatly reduced compared to conventional communication equipment due to the short emmission wavelength of the diode laser. Here, we report the continued development on channeled-substrate-planar (CSP) diode laser optimized for emission wavelengths between 8600Å and 8800Å to minimize the absorption of the light by water vapor in the atmosphere[4]. These optimized CSP lasers have provided up to 205 mW of cw output power with an overall power conversion efficiency from one facet of >35%.

2. CSP LASER STRUCTURE

A schematic diagram and cross-sectional micrograph of a CSP structure optimized for an emission wavelength of 8700Å are shown in Figure 1. The structure is fabricated in a single growth step using liquid phase epitaxy (LPE). V-shaped channels are chemically etched in the (100) oriented GaAs substrate along the [0$\bar{1}$1] direction using an oxide-defined contact mask before LPE growth. Prior to placement of the substrate in the horizontal sliding graphite growth boat, the entire surface of the wafer is subject to a light chemical etch. This procedure ensures that both the surfaces in the channel region and on the substrate are chemically prepared in the same manner for LPE growth.

LPE growth is performed over the V-channeled substrate and four layers are grown: 1) $Al_xGa_{1-x}As$ cladding layer (x=0.27, 0.3μm, $N_d=1\times10^{18}cm^{-3}$); 2) GaAs active layer (0.07μm, $N_d=1\times10^{17}cm^{-3}$); 3) $Al_xGa_{1-x}As$ cladding layer (x=0.27, 1.5μm, $N_a=5\times10^{17}cm^{-3}$); 4) GaAs capping layer (0.7 μm, $N_d=5\times10^{17}cm^{-3}$). The growth is performed at 800°C using a cooling rate of 1°C/min. The fabrication of high power CSP lasers having the proper lateral index profile for fundamental mode operation requires the active layer to be planar over the V-channel while the thickness of the n-cladding layer outside the channel region is maintained between 0.2 and 0.5 μm. A non-planar active layer alters the lateral index profile of the CSP structure, which degrades the superior performance characteristics of the laser. To ensure planar active layer growth over the channel region, it is necessary to maximize the total amount of supercooling associated with the gallium melt used for the growth of the n-cladding layer. This is accomplished in our automated growth system by using the single-phase growth method[5] for the n-cladding layer and the two-phase method[6] for the growth of the other layers in the CSP structure. The single-phase growth method permits us to

Figure 1   Schematic diagram and cross-sectional micrograph of CSP diode laser designed for emission at 8700Å.

accurately control the degree of supercooling present in the gallium melt prior to the introduction of the growth wafer.   In addition to the quick filling of the V-channel to planarize the layer, careful control of the amount of supercooling also permits a high degree of control on layer thickness not only across the wafer but from one LPE growth run to another.   The single-phase growth technique may also be used for the growth of the other layers in the structure, but is not necessary since the n-cladding layer grown directly on the non-planar substrate planarizes the surface for the subsequent layers.   The use of the single-phase growth technique for all the layers in the structure would unnecessarily complicate the growth process.

Another factor affecting the planarity of the active layer in the CSP structure is the crystal orientation of growth substrate.   The effects of surface morphology due to large amounts (>0.5°) of substrate misorientation with respect to the (100) surface has been previously noted in the literature[7,8,9].   We have found that substrate misorientations as small as 0.1° may result in terracing of the n-cladding and active layers in the CSP structure during the LPE growth process.   Thus, the shape or planarity of the epitaxial layers are extremely sensitive to such factors as the non-planar growth surface, substrate orientation, and growth conditions.   Local arsenic concentration gradients in and around the channels influence the lateral and vertical growth rates which lead to terracing of the epitaxial layers as the channels are filled[10].   Although this effect is not desired in the CSP laser, other high-power lasers, such as the terraced-heterostructure large optical cavity (TH-LOC) laser, have been fabricated exploiting this anomaly[11].   Independent of the growth conditions and/or the geometric channel shape, the terrace or perturbation in the layer would eventually be eliminated as the (100) surface, which possesses the lowest interfacial energy density, is reconstructed.   However, in the CSP structure the terrace must be eliminated before the growth of the active layer otherwise the change in the active layer thickness due to the terrace alters the lateral index profile of CSP structure.   By optimizing the LPE growth conditions and minimizing the misorientation of the growth substrate with respect to the (100) plane, planar active layer growth can be obtained on a routine basis.

A terrace formed in the active layer of the CSP structure cannot be observed in standard high magnification cross-sectional micrographs.   A more effective examination technique is angle lapping of the growth surface.   A 1° angle lap polished perpendicular to the active layer can reveal terracing as small as 100Å.   Figure 2(a) and 2(b) are 1° angle lap micrographs of two CSP growth runs displaying a terraced and a non-terraced active

layer, respectively. The height of the terrace or step in figure 2(a) is approximately 600Å which yields a 20% change in the active layer thickness. Thus, this terrace represents a significant change in the properties of the CSP structure. A CSP laser with a planar active layer is depicted in Figure 2(b). Laser devices fabricated from this wafer displayed low threshold operation, kink-free P-I curves to high output powers, fundamental mode operation, and stable far-field radiation patterns while devices fabricated with the terraced active layers displayed kinks in the P-I curve and far-field radiation patterns that move with changing drive current. Thus, careful control of the V-channel etching, substrate orientation, and LPE growth can lead to the fabrication of CSP lasers having desirable performance properties. The flow of current in the CSP structure is confined to the channel region via a deep zinc diffusion. Zinc is diffused through the n-type cap layer into the p-type cladding layer using an oxide-defined contact mask thereby forming a reverse bias p-n junction to confine the current flow. The leading edge of the zinc front is positioned approximately 0.5 μm above the active layer.

Terraced   **Planar**

Cap
p-Cladding
Active
n-Cladding
Substrate

|—| $\mathbf{I}$ 0.5μm |—| $\mathbf{I}$ 0.5μm
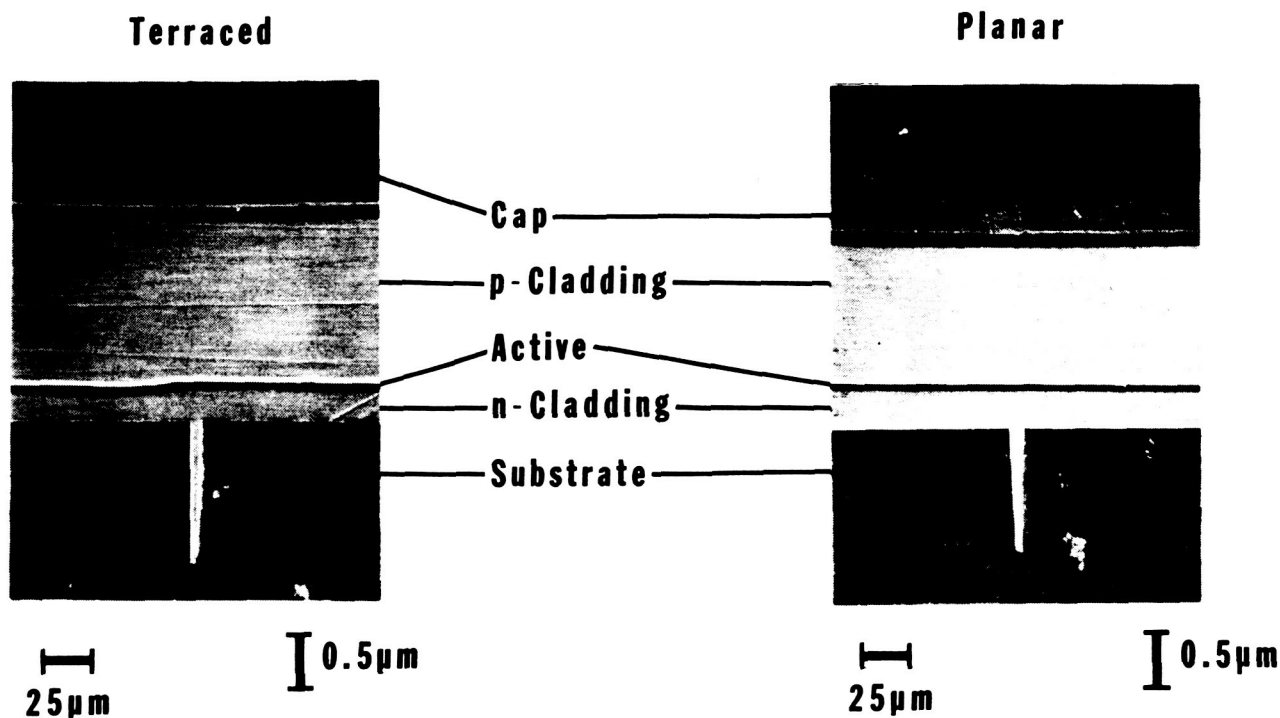**25μm**   **25μm**

Figure 2 (a) Polished 1° angle lap of a CSP diode laser having a terraced active layer. (b) Polished 1° angle lap of a CSP diode laser optimized for high power operation at an emission wavelength of 8700Å.

3. CSP LASER PERFORMANCE

In Figure 3, the power output versus drive current (P-I) curves for two devices are displayed. The devices are 200 μm long, with a (1/4) Al_2O_3 passivation coating on the (front) emitting facet and a six layer dielectric-stack reflector on the rear facet[12]. In Figure 3(a) we show the performance of the CSP laser as the heat sink temperature is varied from 0 to 80°C. Note that 80 mW cw output power was obtained at a heat sink temperature of 80°C. The device operated in a stable single spatial mode over the entire temperature range. The differential quantum efficiency of the device decreased from 62% to 45% as the heat sink temperature was raised from 0 to 80°C. The T_o value for this device in cw operation over this temperature range is appoximately 100°K. At 62% differential quantum efficiency, the slope efficiency of the device is 0.89 mW/mA.

Figure 3(b) shows the results of operating a device to its catastrophic optical damage (COD) level. Damage occured at 205 mW cw at a drive current of 335 mA. The applied voltage at 205 mW is 1.76V. The emitting facet of the device displayed melting of the crystalline material, normally associated with facet damage. This exceptionally high COD level was

85

level is reached. While the heatsink temperature was varied, we monitored the far-field pattern of several optimized CSP devices. At powers below 100mW, the lateral far-field pattern remains unchanged in both the cw and pulsed conditions. This is expected since the lateral mode confinement is provided by a real index dielectric waveguide. This also confirms that the superior device performance is not related to changes in the lateral mode guiding. Typical beam dimensions at FWHP levels in the planes parallel and perpendicular to the junction for the optimized CSP structure are $8-12^\circ$ and $22-26^\circ$, respectively. The exceptional single mode performance of this device at high output powers is related to the very high power conversion efficiency it displays. This high efficiency significantly reduces thermal effects at high output powers which can modify the index profile. Small changes in the complex lateral index profile due to joule heating can dramatically degrade the single-mode properties of the device. Minimizing the joule heating in this structure by reducing optical absorption losses has permitted operation in a single spatial mode at output powers previously unattainable before in conventional CSP structures.

In free-space communications, large signal losses may occur due to aberrations in the collimated output beam of the diode laser. The source of these aberrations maybe associated with the diode laser, the optical system forming the beam, or variations in the atmosphere if the system is use for communication between space and ground terminals. In conventional oxide-defined or gain-guided lasers, sizable aberrations are present in the output beam. In particular, they exhibit large amounts of astigmatism, which change as power is varied and during modulation. By using index-guided laser sources, such as CSP type device, to achieve diffraction limited performance aberrations are minimized. The phase fronts of collimated 8700Å CSP diode lasers have been experimentally measured using a LADITE computer controlled Mach-Zehnder interferometer. The total rms phase aberrations measured $\cong \lambda/50$ under all operating conditions up to 100mW of cw output power, well below the level at which aberrations significantly decrease beam quality.

Preliminary lifetest studies have been conducted both in the cw and 50% duty cycle (10MHz) modes of operation at 30 and 50 mW, respectively. Lifetesting has been performed both at room and elevated temperatures to accelerate the degradation rate associated with the CSP lasers. The elevated temperatures used in our lifetests are 50 and 70°C. The devices were tested using a constant power technique where the drive current used to power the device is continually adjusted to maintain rated output power. This technique subjects the devices to a greater operational stress than the constant current technique where the laser device is placed on lifetest at rated power and the change in output power is monitored. The devices used in the lifetests were mounted p-side down to a copper heatsink using a hard solder and the n-side contact was made using a gold wirebonded lead. To date, devices placed on room temperature (25°C) lifetest at 50mW (50% duty-cycle) have operated over 5000 hours with little or no change in drive current. Lifetesting of devices at elevated temperatures has also produced similiar results. The best devices at 50°C have operated over 4,000 hours with little or no change in drive current. This indicates room temperate lifetimes in excess of 30,000 hours (assuming an activation energy=0.7eV). These lifetests are continuing.

4. CONCLUSION

In conclusion, we present a high-power CSP laser diode which has been optimized for operation in the 8600Å to 8800Å wavelength range. Exceptionally high cw output powers and overall power conversion efficiencies have been achieved. In addition, both single-spatial and single-longitudinal mode operation at very high output powers have been attained due to improved device efficiency. These increases in performance criteria should permit more reliable operation at high-output power levels.

5. ACKNOWLEDGMENTS

a mode hop. When a mode hop or shift occurs, the power in the longitudinal mode is shared between modes. We have found that the mode hop normally occurs over a 2-3°C temperature range and that the longitudinal mode is stable both above and below this transition region. These shifts are normally seen appoximately every 6-7°C over the temperatures we investigated. One of the best CSP devices exhibited stable longitudinal mode operation over a 15°C temperature range at a cw output power of 41mW[14]. The wavelength shifted from 8688Å to 8700Å as the temperature was varied from 19 to 34°C. This corresponds to a wavelength dependence of 0.8Å/°C over this temperature range. Over a much larger temperature range (~50°C) this device displayed the characteristic 3Å/°C wavelength dependence normally associated with CSP-type lasers.

The lateral far-field patterns of an optimized CSP laser from 25-190mW of cw output power are shown in Figure 4(b). Below 100 mW the beam full width at half-power (FWHP) of the lateral far-field patterns remained unchanged with drive current. At output powers of 100 mW and above the beam FWHP broadens from 11 to 15° with increasing drive current due to heating and gain saturation in the CSP structure. The perpendicular far-field pattern did not change with increasing drive current, the beam FWHP remaining unchanged at 25°. At output powers exceeding 190mW, higher order mode operation begins to dominant until the COD
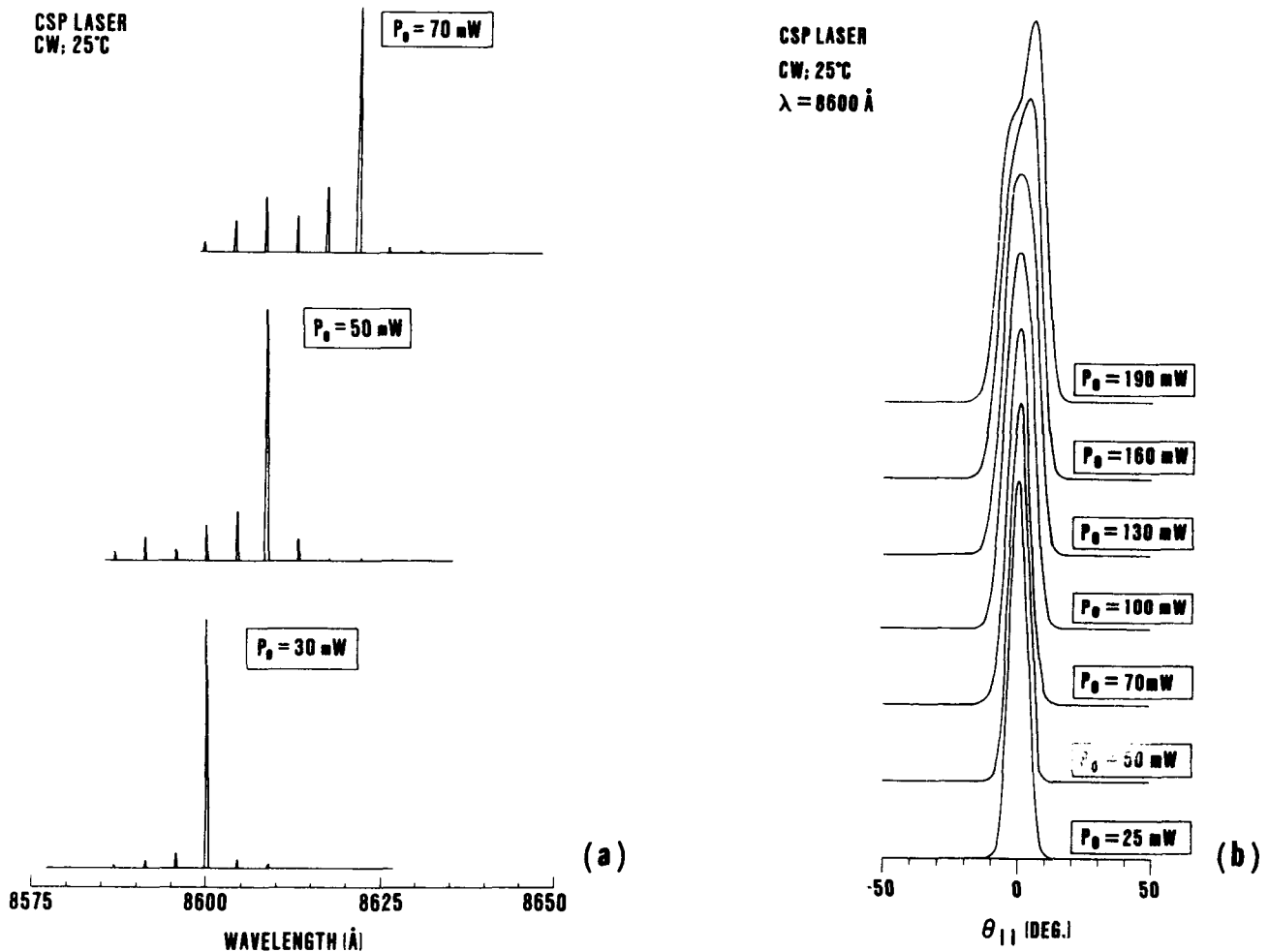

(a)

(b)

Figure 4   (a) Spectra of the CSP diode laser operating in the cw mode at elevated power levels. Spectrometer resolution is 0.15Å.   (b) Far-field radiation patterns in the plane parallel to the junction of a CSP diode laser operating in the cw mode at elevated power levels. The perpendicular far-field beam FWHP was unchanged at 25°.

87

level is reached. While the heatsink temperature was varied, we monitored the far-field pattern of several optimized CSP devices. At powers below 100mW, the lateral far-field pattern remains unchanged in both the cw and pulsed conditions. This is expected since the lateral mode confinement is provided by a real index dielectric waveguide. This also confirms that the superior device performance is not related to changes in the lateral mode guiding. Typical beam dimensions at FWHP levels in the planes parallel and perpendicular to the junction for the optimized CSP structure are 8-12° and 22-26°, respectively. The exceptional single mode performance of this device at high output powers is related to the very high power conversion efficiency it displays. This high efficiency significantly reduces thermal effects at high output powers which can modify the index profile. Small changes in the complex lateral index profile due to joule heating can dramatically degrade the single-mode properties of the device. Minimizing the joule heating in this structure by reducing optical absorption losses has permitted operation in a single spatial mode at output powers previously unattainable before in conventional CSP structures.

In free-space communications, large signal losses may occur due to aberrations in the collimated output beam of the diode laser. The source of these aberrations maybe associated with the diode laser, the optical system forming the beam, or variations in the atmosphere if the system is use for communication between space and ground terminals. In conventional oxide-defined or gain-guided lasers, sizable aberrations are present in the output beam. In particular, they exhibit large amounts of astigmatism, which change as power is varied and during modulation. By using index-guided laser sources, such as CSP type device, to achieve diffraction limited performance aberrations are minimized. The phase fronts of collimated 8700Å CSP diode lasers have been experimentally measured using a LADITE computer controlled Mach-Zehnder interferometer. The total rms phase aberrations measured $\cong \lambda/50$ under all operating conditions up to 100mW of cw output power, well below the level at which aberrations significantly decrease beam quality.

Preliminary lifetest studies have been conducted both in the cw and 50% duty cycle (10MHz) modes of operation at 30 and 50 mW, respectively. Lifetesting has been performed both at room and elevated temperatures to accelerate the degradation rate associated with the CSP lasers. The elevated temperatures used in our lifetests are 50 and 70°C. The devices were tested using a constant power technique where the drive current used to power the device is continually adjusted to maintain rated output power. This technique subjects the devices to a greater operational stress than the constant current technique where the laser device is placed on lifetest at rated power and the change in output power is monitored. The devices used in the lifetests were mounted p-side down to a copper heatsink using a hard solder and the n-side contact was made using a gold wirebonded lead. To date, devices placed on room temperature (25°C) lifetest at 50mW (50% duty-cycle) have operated over 5000 hours with little or no change in drive current. Lifetesting of devices at elevated temperatures has also produced similiar results. The best devices at 50°C have operated over 4,000 hours with little or no change in drive current. This indicates room temperate lifetimes in excess of 30,000 hours (assuming an activation energy=0.7eV). These lifetests are continuing.

4. CONCLUSION

In conclusion, we present a high-power CSP laser diode which has been optimized for operation in the 8600Å to 8800Å wavelength range. Exceptionally high cw output powers and overall power conversion efficiencies have been achieved. In addition, both single-spatial and single-longitudinal mode operation at very high output powers have been attained due to improved device efficiency. These increases in performance criteria should permit more reliable operation at high-output power levels.

5. ACKNOWLEDGMENTS

6. REFERENCES

1. B. Goldstein, M. Ettenberg, N.A. Dinkel, and J.K. Butler, " A high-power channeled-substrate-planar AlGaAs diode laser," Appl. Phys. Lett. 47 (1985) 655.

2. M. Sakamoto, K. Aiki, and H. Ouchi, "High-power laser diodes," Hitachi Review 31 (1982) 227.

3. T. Shibutani, M. Kume, K. Hamada, H. Shimizu, K. Itoh, G. Kano, and I. Teramoto, "A novel high-power laser structure with current-blocked regions near cavity facets," IEEE J. Quantum Electron., QE- 23 (1987) 760.

4. D.B. Carlin, G.N. Pultz, and B.Goldstein, "0.87 μm CSP diode lasers for spaceborne communications," SPIE Vol. 756 Optical Technologies for Space Communicatios Systems (1987).

5. J.J. Hsieh, "Thickness and surface morphology of GaAs LPE layers grown by supercooling, step-cooling, equilibrium-cooling, and two-phase solution techniques," J. Crystal Growth 27 (1974) 49.

6. *Ibid*

7. T. Nishinaga, K. Pak, and S. Uchiyama, "Studies of LPE ripple on morphological stability theory," J. Crystal Growth 43 (1978) 85.

8. B.L. Mattes and R.K. Route, "LPE growth of GaAs: formation of nuclei and surface terraces," J. Crystal Growth 27 (1974) 133.

9. D. L. Rode, "Crystal growth terraces and surface reconstruction," J. Crystal Growth 27 (1974) 313.

10. D. Botez, W. Tsang, and S. Wang, "Growth characteristics of GaAs-Ga$_{1-x}$Al$_x$As structures fabricated by liquid-phase epitaxy over preferentially etched channels," Appl. Phys. Letters 28 (1976) 234.

11. D. Botez and J.C. Connolly, "Terraced-heterostructure large optical cavity AlGaAs diode laser: A new type of high-power cw single-mode device," Appl. Phys. Letters 41 (1982) 310.

12. M. Ettenberg, "A new dielectric facet reflector for semiconductor lasers," Appl. Phys. Lett. 32 (1978) 724.

13. T. Murakami, K. Ohtaki, H. Matsubara, T. Yamawaki, H. Saito, K. Isshiki, Y. Kokubo, A. Shima, H. Kumabe, and W. Susaki, "A very narrow-beam AlGaAs laser with a thin tapered-thickness active layer (T^3 laser)," IEEE J. Quantum Electron., QE-23 (1987) 712.

14. H. Hendricks and T. Mack, *private communication*.

Self-consistent analysis of gain saturation in channeled-substrate-planar double-heterojunction lasers

Jerome K. Butler[a] and Gary A. Evans

David Sarnoff Research Center, CN 5300, Princeton, New Jersey 08543-5300

A self-consistent model for semiconductor lasers [using the channeled-substrate-planar (CSP) double-heterojunction (DH) laser as an example] which does not assume constant optical power along the laser axis is developed. This approach allows for the analysis of high-power lasers with low facet reflectivities which produce nonuniform photon densities along the propagation direction. Analytical equations for the modal gain coefficient, the threshold current density, and the radiated power for a specific CSP laser structure are obtained.

Semiconductor lasers with high reflectivity facets (>0.3) have an almost uniform density of photons along their longitudinal axis, allowing the assumption of uniform gain in their analysis. However, the highest power from a semiconductor laser is achieved using a high reflectivity end facet and a low reflectivity (0.05–0.1) output facet resulting in large variations of the photon density along the cavity axis.[1-4] In this letter we extend a recent uniform (longitudinal) gain analysis[5] based on the "self-consistent model." This extension, which allows for photon density variations along the longitudinal axis, results in relatively simple phenomenological equations for the modal gain coefficient, the threshold current density, and (in the limit of high facet reflectivities) the radiated power.

In self-consistent models the carrier density in the active layer is derived from a solution of the diffusion equation having both source and sink terms. The source for the injected carriers is the drive current, whereas the sink is the stimulated recombination. The current flow into the active layer varies laterally and lateral carrier diffusion within the active region affects the optical gain profile modifying the shape of the optical field distribution in the laser diode.[6-14] The spatial dependence of the recombination term is computed from the product of the lateral gain profile and the photon density in the active layer as a function of position along the longitudinal axis.

For wave propagation of the form $\exp(j\omega t - \gamma z)$, the transverse electric field polarized along y can be solved using the effective index method; it is written as

$$E_y = E_0 u(x,y) v(y) \exp(-\gamma z), \qquad (1)$$

where the complex function $u(x,y)$ determines the transverse field shape along x, but it is slowly varying (along y) compared to $v(y)$ which defines the lateral field profile. The nonlinear differential equation for the lateral field $v(y)$ satisfies

$$\frac{d^2 v}{dy^2} + [\gamma^2 - \gamma_0^2 + k_0^2 \Gamma_c(y) \kappa_a(y,P_a)] v = 0, \qquad (2)$$

where $\Gamma_c(y)$ is the complex confinement factor and k_0 is the free-space wave number. The complex effective index of refraction is $n_{\text{eff}} = -j\gamma_0(y)/k_0$ and $\gamma_0(y)$ is found from the

solution of the transverse problem. The value $\kappa_a(y,P_a)$ is the carrier-dependent part of the dielectric constant in the active layer and P_a is the optical power in the active layer. In terms of the active layer gain $g(y,P_a)$, the dielectric perturbation can be expressed as

$$\kappa_a(y,P_a) = n_a g(y,P_a)(2R + j)/k_0, \qquad (3)$$

where n_a is the passive index of the active layer and R is the gain-induced index suppression coefficient.

The carrier distribution in the active layer must be found from solutions of the inhomogeneous diffusion equation having both "source" and "sink" terms. The source term is $R_{\text{pump}} = J_x(y)/q d_a$, where $J_x(y)$ is the current density, q is the electronic charge, and d_a is the active layer thickness. For typical stripe geometry laser structures with Zn diffusion fingers, the lateral variation of the current density can be fit to the simple analytic formula[15]

$$J_x(y) = \begin{cases} J_0 & |y| < S/2 \\ \dfrac{J_0}{[1 + (|y| - S/2)/y_0]^2} & |y| > S/2 \end{cases}, \qquad (4)$$

where J_0 is the current density under the stripe, S is the stripe width; y_0 is primarily a function of the Zn diffusion depth, the stripe contact width, and the resistivities of the various epitaxially grown layers. The injected current density is assumed to be invariant with z since the current density flowing into the active layer is controlled predominately by the series resistance R_s due to the various grown layers.[16] Further, it has been shown that above threshold, the differential resistance of the junction is small compared to R_s.[15] The sink term is $R_{\text{st}} = P\Gamma(y)|v|^2 g(y, P_a)$, where P is the intracavity power, $\Gamma(y)$ is the intensity confinement factor of the active layer, and $|v|^2$ is normalized to unity over $(-\infty, \infty)$.

The diffusion equation governing the pair density $N(y)$ is

$$D_e \frac{d^2 N}{dy^2} - \frac{N}{\tau_s} - BN^2 = -R_{\text{pump}} + R_{\text{st}}, \qquad (5)$$

where D_e is the effective diffusion coefficient, τ_s is the carrier lifetime, and B is the bimolecular recombination coefficient. The gain coefficient is $g(y,P_a) = aN(y) - b$, where $a = 2.5 \times 10^{-16}$ cm^2 and $b = 190$ cm^{-1}. In general, the stimulated recombintion term R_{st} will be functionally depen-
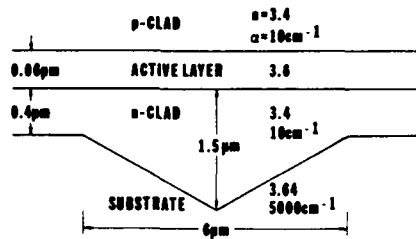
FIG. 1. CSP DH geometry used for the laser device.

dent on z. However, we have neglected carrier diffusion along the longitudinal direction since $|\partial N/\partial z| \ll N/L_D$, where L_D is the carrier diffusion length.

At a given point z, the intracavity power $P(z) = P^+(z) + P^-(z)$ is the sum of the forward and backward waves. The power in the active layer P_a is computed from a fraction of the intracavity power P. In lasers with high facet reflectivities, the intracavity power is almost constant along the z direction; however, when reflectivities are small, $P(z)$ has relativity large changes along the axis. The modal power gain coefficient $G = -2Re(\gamma)$ is computed from the self-consistent solutions of the carrier diffusion and Maxwell's equations.

Solutions of the optical fields of the channeled-substrate-planar (CSP) double-heterojunction (DH) structure with the material parameters shown in Fig. 1 are obtained with an index suppression coefficient $R = -2$. The parameters used in the diffusion equation are $L_D = \sqrt{D_e \tau_s} = 3$ μm, $\tau_s = 3$ ns, $B = 10^{-10}$ cm^3/s, the stripe width $S = 6\mu m$, and $y_0 = 0.5 \mu m$. The points in Fig. 2 show numerically computed values of the modal gain coefficient as a function of the intracavity power for different values of drive current which has been normalized for a laser length $L = 100 \mu m$.

Although the numerical data can be used to calculate the longitudinal variation of the gain in a laser with known facet reflectivities, it is useful to fit the numerically calculat-

ed modal gain coefficient points to an analytical expression (motivated by the form of the equation for gain saturation in homogeneously and inhomogeneously broadened systems)[17] written as

$$G(P) = \left(\frac{I}{I_0}\right)^c \frac{G_0}{(1 + P/P_s)^d} - \alpha_1, \tag{6}$$

where c, d, G_0, P_s, and α_1 are unknown constants. An optimization procedure for a least-squares fit of (6) to the computed values of the self-consistent model gives $c = 0.708$, $d = 0.687$, $G_0 = 51.4$/cm, $P_s = 41.2$ mW, and $\alpha_1 = 49.6$/cm. (The value of I_0 is arbitrary but we used $I_0 = 10$ mA for the computed G_0 above. Note that G_0 and I_0 can be combined to form a single constant.) The resulting gain curves for these parameters are also illustrated in Fig. 2. It is interesting to note that the value of c is not unity due to the fact that bimolecular recombination is significant. The value of d is unity for a classical two-level system which is broadened homogeneously, whereas it is $1/2$ for an inhomogeneously broadened laser. P_s is the saturation power and α_1 is the modal loss coefficient in the absence of gain. At threshold, the intracavity power $P = 0$ and the threshold current is

$$I_{th} = I_0[(G_{th} + \alpha_1)/G_0]^{1/c}, \tag{7}$$

where $G_{th} = (1/2L)\ln(1/R_1 R_2)$, and R_1 and R_2 are the facet reflectivities. In the event the reflectivities are high, the intracavity power is almost constant along z and the gain $G \approx G_{th}$. The emission power from the R_1 facet is obtained from (6)

$$P_{rad} = P_s \left(\frac{1 - R_1}{1 + R_1}\right)\left[\left(\frac{I}{I_{th}}\right)^{c/d} - 1\right]. \tag{8}$$

This is just the expression for the emission power versus drive current one would obtain for uniform photon densities. When one or both of the facet reflectivities is small, the intracavity power varies considerably along the laser axis and must be computed from the integral equation

$$P(z) = P_0\left[\exp\left(\int_0^z G(P)dz'\right)\right.$$
$$\left. + \frac{1}{R_2}\exp\left(-\int_0^z G(P)dz'\right)\right], \tag{9}$$
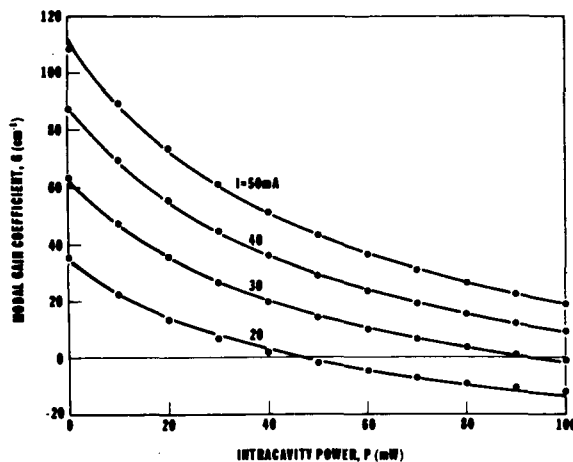

FIG. 2. Optical gain characteristics of the fundamental mode as a function of the intracavity power. The drive current is for a device of length $L = 100$ μm. The dots are computed from a self-consistent model[5] and the solid curves are obtained from Eq. (6).

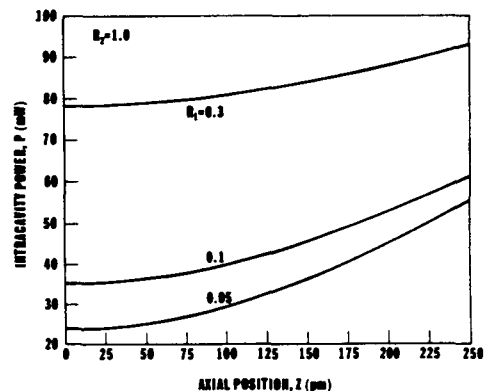
FIG. 3. Intracavity power computed from Eq. (9) for a laser of length $L = 250 \mu m$. The back facet has $R_2 = 1$ while the front facet reflectivity is treated as a parameter. The total emission power from the front facet is 50 mW.
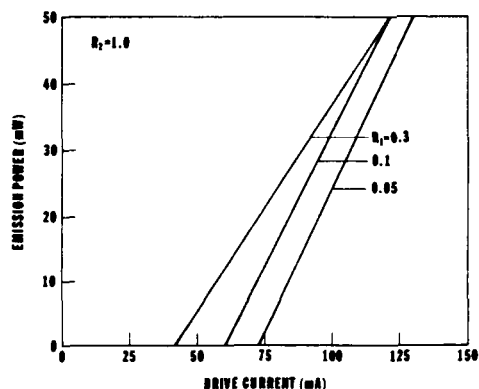
FIG. 4. Emission power from the front facet vs drive current. These data were obtained from repeated solutions of Eq. (9).

where P_0 is an eigenvalue, facet 2 lies at $z = 0$ and facet 1 lies at $z = L$. The boundary condition on $G(P)$ requires its integral over the length of the cavity $= 1/2 \ln(1/R_1 R_2)$.

Figure 3 shows the results for a laser with $L = 250 \mu m$ and an emission power $P_{rad} = 50$ mW. The back facet has a reflectivity $R_2 = 1$, and the output facet reflectivity R_1 is treated as a parameter. [The threshold current can be computed using Eq. (7).] When the output facet reflectivity is 0.3, P is almost constant along the laser axis; however, for $R_1 = 0.05$, the intracavity power varies from about 24 mW at $z = 0$ to about 55 mW at $z = L$. Figure 4 shows the power versus current for the different reflectivities.

In conclusion, we have developed a self-consistent model for semiconductor lasers (using the CSP DH laser structure as an example) without assuming constant optical power along the laser axis. The advantage of the present approach allows for the analysis of lasers (typically high-power) with small facet reflectivities which produce nonuniform photon densities along the propagation direction. Generally, the hole burning effects will be larger at the output facet because the optical density is highest there. Further, hole burning is nonuniform in the direction of propagation. However, in lasers with $L > 200 \mu m$ and moderate facet reflectivities, the longitudinal nonuniformities are slowly varying compared to the carrier diffusion length. We also have developed analytical equations for the modal gain coefficient, the threshold current density, and (in the limit of high facet reflectivities) the radiated power for a specific CSP laser structure.

[1]G. P. Agrawal, W. B. Joyce, R. W. Dixon, and M. Lax, Appl. Phys. Lett. 43, 11 (1983).
[2]R. Baets and P. E. Lagasse, Electron. Lett. 20, 41 (1984).
[3]P. Meissner, E. Patzak, and D. Yevick, IEEE J. Quantum Electron. QE-20, 899 (1984).
[4]R. Baets, J. P. van de Capelle, and P. E. Lagasse, IEEE J. Quantum Electron. QE-21, 693 (1985).
[5]J. K. Butler, G. A. Evans, and B. Goldstein, IEEE J. Quantum Electron. QE-23, 1890 (1987).
[6]J. Buus, IEEE J. Quantum Electron. QE-15, 734 (1979).
[7]W. Streifer, D. R. Scifres, and R. D. Burnham, Appl. Phys. Lett. 37, 877 (1980).
[8]W. Streifer, D. R. Scifres, and R. D. Burnham, IEEE J. Quantum Electron. QE-17, 1521 (1981).
[9]W. Streifer, D. R. Scifres, and R. D. Burnham, IEEE J. Quantum Electron. QE-17, 736 (1981).
[10]M. Ueno, R. Lang, S. Matsumoto, H. Kawano, T. Furuse, and I. Sakuma, IEEE Proc. 129, Part I, 218 (1982).
[11]S. Wang, C. Y. Chen, A. S. Liao, and L. Figueroa, IEEE J. Quantum Electron. QE-17, 453 (1981).
[12]K. A. Shore, Opt. Quantum Electron. 15, 371 (1983).
[13]G. P. Agrawal, IEEE J. Lightwave Technol. LT-2, 537 (1984).
[14]J. Buus, IEEE Proc. 132, 42 (1985).
[15]R. Papannareddy, W. E. Ferguson, and J. K. Butler, IEEE J. Quantum Electron. QE-24, Jan. (1988).
[16]G. Lengyel, P. Meissner, E. Patzak, and K. H. Zschauer, IEEE J. Quantum Electron. QE-18, 618 (1982).
[17]A. Yariv, in Quantum Electronics, 2nd ed. (Wiley, New York, 1975).

NASA

National Aeronautics and
Space Administration

Report Documentation Page

1. Report No.	2. Government Accession No.	3. Recipient's Catalog No.
NASA CR-4238		

4. Title and Subtitle	5. Report Date
High-Power Single Spatial Mode AlGaAs Channeled-Substrate-Planar Semiconductor Diode Lasers for Spaceborne Communications	June 1989
	6. Performing Organization Code

7. Author(s)	8. Performing Organization Report No.
J. C. Connolly, D. B. Carlin, and M. Ettenberg	
	10. Work Unit No.
	506-44-21-01

9. Performing Organization Name and Address	11. Contract or Grant No.
David Sarnoff Research Center Princeton, NJ 08540-5300	NAS1-17441
	13. Type of Report and Period Covered

12. Sponsoring Agency Name and Address	Contractor Report 7/16/87 - 10/15/88
National Aeronautics & Space Administration Langley Research Center Hampton, VA 23665-5225	14. Sponsoring Agency Code

15. Supplementary Notes

Langley Technical Monitor: Herbert D. Hendricks

Final Report

16. Abstract

A high-power single-spatial-mode channeled substrate planar AlGaAs Semiconductor Diode Laser has been developed. The emission wavelength has been optimized at 860-880 nm. The operating characteristics (power-current, single spatial mode behavior, far-field radiation patterns, and spectral behavior) and results of computer modeling studies on the performance of the laser will be discussed. Reliability Assessment at high output levels is also included. Performance Results on a new type of Channeled Substrate Planar Diode Laser incorporating current blocking layers, grown by Metalorganic Chemical Vapor Deposition, to more effectively focus the operational current to the lasing region has been demonstrated. The optoelectronic behavior and fabrication procedures for this new diode laser are discussed. The highlights of this study include single spatial mode devices with up to 160-mW output at 8600 Å, and quantum efficiencies of 70% (1 W/amp) with demonstrated operating lifetimes of 10,000 h at 50 mW.

17. Key Words (Suggested by Author(s))	18. Distribution Statement
Semiconductor Laser High Power AlGaAs (Aluminum Gallium Arsenide) Index Guided	Unclassified - Unlimited Subject Category 36

19. Security Classif. (of this report)	20. Security Classif. (of this page)	21. No. of pages	22. Price
Unclassified	Unclassified	104	A06

NASA FORM 1626 OCT 86

NASA-Langley, 1989

END DATE AUG. 18, 1989